



## City Research Online

### City, University of London Institutional Repository

---

**Citation:** Kabir, I. R. (2019). Modelling of Laser Surface Glazing for Metallic Materials by Finite Element Method. (Unpublished Doctoral thesis, City, University of London)

This is the accepted version of the paper.

This version of the publication may differ from the final published version.

---

**Permanent repository link:** <https://openaccess.city.ac.uk/id/eprint/22299/>

**Link to published version:**

**Copyright:** City Research Online aims to make research outputs of City, University of London available to a wider audience. Copyright and Moral Rights remain with the author(s) and/or copyright holders. URLs from City Research Online may be freely distributed and linked to.

**Reuse:** Copies of full items can be used for personal research or study, educational, or not-for-profit purposes without prior permission or charge. Provided that the authors, title and full bibliographic details are credited, a hyperlink and/or URL is given for the original metadata page and the content is not changed in any way.

# **Modelling of Laser Surface Glazing for Metallic Materials by Finite Element Method**

by

**Israt Rumana Kabir**

Supervisor

**Dr Sumsun Naher**

A thesis submitted in fulfilment of the requirements for the degree of

**Doctor of Philosophy**

in

Mechanical Engineering

Department of Mechanical Engineering & Aeronautics  
School of Mathematics, Computer Science & Engineering



July 2018

# List of contents

List of contents	II
List of figures	VII
List of tables	X
List of symbols and abbreviations	XI
Acknowledgement	XIV
Declaration	XV
Preface	XVI
Abstract	XVII
Chapter 1 <b>Introduction</b>	1
1.1 Thesis structure	6
Chapter 2 <b>Literature review</b>	8
2.1 Thermal modelling of Laser Surface Glazing and similar processes	8
2.1.1 Laser Surface Glazing	9
2.1.2 Laser Welding	11
2.1.3 Laser Cladding	13
2.1.4 Selective Laser Melting	15
2.2 Residual stress of laser melting processes	17
2.2.1 Thermomechanical modelling of laser melting processes	18
2.3 Miscellaneous coupled model of laser melting processes	25
2.4 Controlling factors in modelling of laser melting processes	26
2.4.1 Material properties	27

2.4.2 Heat source model	28
2.4.3 Laser coupling efficiency or absorptivity	31
2.4.4 Plasticity models	33
2.5 Summary	34
<b>Chapter 3 Thermal modelling of LSG</b>	<b>35</b>
3.1 Introduction	35
3.2 Methodology	35
3.2.1 Materials	37
3.2.2 Model geometry	38
3.2.3 Laser parameters	39
3.2.4 Thermal modelling principle	40
3.3 FEM model set-up	45
3.3.1 FEM solver, ANSYS	45
3.3.2 2D and 3D models	45
3.4 Temperature distribution calculation using an explicit solution	49
3.5 Results and discussion	50
3.5.1 2D and 3D FEM models	50
3.5.2 Comparing results from FEM models and explicit solution	60
3.6 Summary	61
<b>Chapter 4 Thermomechanical modelling of LSG</b>	<b>63</b>
4.1 Introduction	63

4.1.1 Residual stress in LSG	63
4.2 Methodology	65
4.2.1 2D FEM thermomechanical model set-up	67
4.3 Results and discussion	69
4.3.1 Temperature change rate, $dT/dt$	69
4.3.2 Stress and strain	71
4.3.3 Prediction of crack formation	84
4.4 Summary	85
<b>Chapter 5 Parametric study of the LSG model</b>	<b>87</b>
5.1 Introduction	87
5.1.1 Laser surface glazing of Ti6Al4V alloy	87
5.2 3D thermal model of LSG for different laser power	88
5.2.1 Results and discussion	90
5.3 3D thermal model for different heat source	92
5.3.1 Surface heat source	93
5.3.2 Volumetric heat source	93
5.3.3 Results and discussion	94
5.4 Summary	94
<b>Chapter 6 Application of LSG thermal model in quenching and tempering</b>	<b>96</b>
6.1 Introduction	96
6.1.1 Quenching and Tempering in TMT	96

6.1.2 Structure of TMT steel	97
6.1.3 Previous relevant modelling works	98
6.2 Methodology	100
6.2.1 Materials selection	100
6.2.2 Principle of quenching and tempering model	100
6.2.3 FEM model set-up	101
6.3 Results and discussion	102
6.3.1 Temperature distribution and cooling rate	102
6.3.2 Case and core depth	107
6.4 Summary	107
<b>Chapter 7 Conclusions and future recommendation</b>	<b>109</b>
7.1 Thermal modelling of LSG	109
7.2 Parametric study of 3D LSG thermal model	110
7.3 Thermomechanical modelling of LSG	110
7.4 Application of LSG thermal model in quenching and tempering	111
7.5 Future recommendations	112
References	114
Appendices	123
A1. Theory and background	123
A1.1 Principle of heat conduction in solid	123
A1.2 Thermal residual stress	123

A1.3 Finite element method	124
A1.4 Thermomechanical coupling method	125
A2. Mesh convergence	126
A2.1 Mesh convergence study of LSG model	126
A2.2 Mesh convergence study of quenching and tempering model	127
A3. APDL code of LSG modelling	129
A3.1 Geometry and mesh of half-cylindrical workpiece	129
A3.2 Thermal model with surface and volumetric heat source	131
A3.3 2D thermomechanical model for Ti6Al4V alloy	133

# List of figures

Figure 1. 1 (a) Experimental arrangement of LSG, (b) laser modified surface [3]	2
Figure 1. 2 Application of LSG process	3
Figure 1. 3 Necessity for optimisation of laser parameters through modelling	5
Figure 2. 1 (a) Temperature distribution along X, Y and Z axis on the surface (b) Thermal cycles at different depths from surface [28]	10
Figure 2. 2 Variation in residual stresses with laser energy density, when surface experience melting the compressive residual stress transform to tensile [48]	18
Figure 2. 3 Thermomechanical coupling used in laser melting processes	22
Figure 2. 4 A typical discretization technique of the T-T-T diagram for phase transformation modelling [21]	25
Figure 2. 5 The Transverse Electrical Mode (TEM) profile of intensity distribution of laser beam [27]	28
Figure 2. 6 Absorptivity of some metals at different wavelength [71]	31
Figure 3. 1 Methodology of developing thermal model of LSG using FEM	37
Figure 3. 2 Schematic illustration of cylindrical geometry used in modelling of laser surface glazing with laser beam fixed at one point over the surface	38
Figure 3. 3 Schematic representation of energy flow during LSG process and the conduction heat flow along x and y directions of a control element taken from the surface exposed to laser heat source	41
Figure 3. 4 Schematic representation of boundary conditions are applied in LSG process	43
Figure 3. 5 The meshed geometries of (a) 2D circular and (b) 3D half-cylinder geometries with stationary laser beam on top of the surface; point O is the middle of the melt pool is created due to laser irradiation	48
Figure 3. 6 Temperature distributions on X-Y plane through the depth from (a) 2D and (b) 3D thermal models of H13 tool steel at 200 W laser power at 0.15 ms time	51

Figure 3. 7 Time-temperature plot from 2D and 3D FEM LSG models of H13 tool steel for 200 W laser power, 0.2 mm beam width and 0.15 ms residence time	53
Figure 3. 8 (a) Cooling rates vs time for different depth from surface to centre upto 60 $\mu\text{m}$ and (b) Cooling rates vs. distance from surface to centre for 0.15 ms and 0.151 ms time	55
Figure 3. 9 TTT diagram of H13 tool steel [41]	57
Figure 3. 10 Temperature isotherm for two laser power (a) 200 W and (b) 300 W, showing melt depth (MD) and heat-affected zone (HAZ). The schematic diagram of the cross-section of half cylinder is pointing out the location of the isotherm	59
Figure 3. 11 Analytical and numerical temperature distributions along the distance from the surface towards the centre in the cooling phase	61
Figure 4. 1 Schematic demonstration of thermal stress development due to thermal strain in temperature gradient mechanism (a) during heating and (b) during cooling [51]	64
Figure 4. 2 Stress strain relationship in bilinear elastic-plastic material	65
Figure 4. 3 Schematic representation of the evolution of yield surface in the principle stresses space during (a) isotropic and (b) kinematic plasticity rule	66
Figure 4. 4 Temperature dependent Young's modulus, Poisson's ratio, yield strength and tangent modulus of H13 tool steels input in the model [89]	69
Figure 4. 5 Temperature change rate ( $dT/dt$ ) vs. time plot for 200 W and 300 W laser power	70
Figure 4. 6 X and Y directional normal stress distribution with time at 200 W laser power from (a) isotropic and (b) kinematic plasticity models	72
Figure 4. 7 X and Y directional normal stress distribution with time at 300 W laser power from (a) isotropic and (b) kinematic plasticity models	74
Figure 4. 8 Mechanism of stress generation on the surface in (a) X and (b) Y direction based on thermal expansion coefficient and temperature gradient principle	75
Figure 4. 9 X and Y directional normal strain vs. time at 200 W laser power from (a) isotropic and (b) kinematic plasticity models	78

Figure 4. 10 X and Y directional normal strain vs. time at 300 W laser power from (a) isotropic and (b) kinematic plasticity models	79
Figure 4. 11 Stresses in X direction ( $\sigma_X^{total}$ ) vs. distance from surface to centre during from the (a) isotropic and (b) kinematic models at 200 W laser power after both heating (0.15 ms) and cooling (0.55 ms)	82
Figure 4. 12 Stresses in X direction ( $\sigma_X^{total}$ ) vs. distance from surface to centre during from the (a) isotropic and (b) kinematic models at 200 W laser power after both heating (0.15 ms) and cooling (0.55 ms)	83
Figure 4. 13 Variation in the equivalent von Misses stress ( $\sigma_e$ ) over time for the (a) isotropic and (b) kinematic plasticity models for different laser powers	85
Figure 5. 1 Variation of peak temperature at different laser powers form the 3D FEM thermal model of Ti6Al4V alloy and H13 tool steel using surface heat flux	91
Figure 5. 2 Variation in temperature distribution for surface heat source and volumetric heat source at 200 W laser power for Ti6Al4V alloy	94
Figure 6. 1 Schematic diagram of quenching and tempering in TMT process after last rolling pass	97
Figure 6. 2 (a) The cylindrical geometry of TMT steel bar and (b) the meshed model	101
Figure 6. 3 Temperature dependant physical properties of structural steel [122–124]	102
Figure 6. 4 Temperature distribution (a) just before the rolled bar subjected to quenching at 0.1 sec, (b) just after quenching starts at 0.3 sec, (c) at the middle of the quenching stage at 1.1 sec, and (d) just after the quenching finish at 2.1 sec	103
Figure 6. 5 Temperature variation along (a) radial and (b) axial distance of the bar	104
Figure 6. 6 (a) Time-temperature plot at different depth and (b) mean cooling rate variation from surface to centre	106
Figure 6. 7 (a) schematic of the composite structure predicted from simulation and (b) literature revealed three different zones 1. Case, 2. Core, and 3. Transition	107

# List of tables

Table 2. 1 Thermal models of LW process for various materials and laser parameters including key findings	12
Table 2. 2 Thermal models of LC process with different materials and process parameters including key findings	14
Table 2. 3 Thermal models of SLM or LSM for various materials and process parameters including key findings	16
Table 2. 4 Materials, software and parameters used in FEM thermomechanical models of some laser melting processes	21
Table 2. 5 The plasticity models and coupling techniques used in the thermomechanical model of laser melting processes	24
Table 2. 6 Various heat source models applied in modelling of different laser melting processes	30
Table 2. 7 Variation of absorptivity depending on laser and material types in different laser surface modification processes	32
Table 3. 1 Chemical composition of H13 tool steel in %weight [4]	38
Table 3. 2 Laser parameters used in the model	39
Table 3. 3 Governing equations, initial and boundary conditions of thermal 2D and 3D LSG modelling	44
Table 3. 4 Thermo-physical properties of H13 tool steel as a function of temperature [41,85]	49
Table 3. 5 The rates of heating and cooling of H13 tool steel at 200 W laser power	53
Table 4. 1 Temperature dependent thermal expansion coefficient of H13 tool steel [87]	68
Table 4. 2 The equivalent Mises stress for different power levels and plasticity models	84
Table 5. 1 Chemical composition of Ti6Al4V alloy in %weight [44]	88
Table 5. 2 Laser parameters used for Ti6Al4V and H13 tool steel alloy	89
Table 5. 3 Thermo-physical properties of Ti6Al4V alloy as a function of temperature [41,72]	90

# List of symbols and abbreviations

<b>Symbols</b>	<b>Specification</b>	<b>Unit</b>
$P$	Laser power	$W$
$C_P$	Specific heat	$Jkg^{-1}K^{-1}$
$k$	Thermal conductivity	$Wm^{-1}K^{-1}$
$T$	Temperature	$K$ or $^{\circ}C$
$T_0$	Initial temperature	$K$ or $^{\circ}C$
$Q$	Internal heat generation	$Wm^{-3}$
$Q_{laser}$	Laser heat intensity	$Wm^{-2}$
$h$	Convection film coefficient	$Wm^{-2}K^{-1}$
$A$	Absorptivity	-
$r_b$	Laser beam radius	$m$
$t_R$	Residence time	$s$
$f()$	Function	-
$dT/dt$	Temperature change rate	$Ks^{-1}$ or $^{\circ}Cs^{-1}$
$t_c$	Time of cooling	$s$
$\rho$	Density	$kgm^{-3}$
$\varepsilon$	Emissivity	-
$\sigma$	Boltzmann's constant, $5.67 \times 10^{-8}$	$Wm^{-2}K^{-4}$
$\pi$	Pi constant, $3.1416$	-
$\varepsilon^{total}$	Total strain	-
$\varepsilon^{el}$	Elastic strain	-
$\varepsilon^{pl}$	Plastic strain	-
$\varepsilon^{th}$	Thermal strain	-
$\sigma_{ij}$	Stress tensor	$Pa$
$\varepsilon_{ij}^p$	Plastic strain increment tensor	-

$\alpha_{ij}$	Back stress tensor	$Pa$
$\sigma_s$	Initial yield stress	$Pa$
$\sigma_f$	Final yield stress	$Pa$
$\sigma_e$	von Mises equivalent stress	$Pa$
$\Delta$	Difference	-
$\nabla$	Gradient operator	-
$q_x$	Heat flux rate along X axis	$Wm^{-2}$
$r_{beam}$	Radius of laser beam	$m$
$\alpha$	Coefficient of thermal expansion	$K^{-1}$
$[D]$	Material stiffness matrix	$Pa$
$V_{y,i}$	Volume fraction of y-phase at i-th step	%
$V_{aus}$	Volume fraction of austenite	%
$V_{marten}$	Volume fraction of martensite	%
$M_s$	Martensite-start transformation temperature	$K$

### Abbreviations

LSG	Laser surface glazing
LW	Laser welding
GTAW	Gas Tungsten arc welding
LC	Laser cladding
SLM	Selective laser melting
LSM	Laser surface melting
FEM	Finite element method
FDM	Finite difference method
FVM	Finite volume method
TMM	Transitional mapped meshing
APDL	ANSYS parametric design language
TMT	Thermomechanical treatment

HAZ	Heat-affected zone
CW	Continuous wave
T-T-T	Time temperature transformation
FEA	Finite element analysis
TEM	Transverse electromagnetic
SF	Surface force
BF	Body force
HPDDL	High power direct diode laser
Nd:YAG	Neodymium-doped Yttrium Aluminum Garnet

# Acknowledgement

Firstly I would like to acknowledge the grace of Almighty to provide me the opportunity to enrol in this PhD program at City, University of London, United Kingdom.

Secondly, I would like to acknowledge the relentless supports and ever-lasting trust rendered by my beloved parents which helped withhold my aim regardless any situations.

After that, most importantly, I would like to show paramount gratitude to my primary supervisor of the PhD, Dr Sumsun Naher. I acknowledge with gratification Dr Naher's all efforts and hard work for not only facilitating the project but also in developing my associative skills in research and personal development. I would like to mention her wide smile and positive energy helped me driving through the bumpy road throughout the years. I would like to acknowledge paramount reverence to Professor Ranjan Banerjee. I felt that throughout my PhD journey he stood beside me like the shade from a banyan tree. Along with his technical guidance in developing confidence for my modelling works, I would like to specially mention, how he used to storm my critical mind through quick chats. As a Guru, he also has taught me the importance of spiritual knowledge and discipline to channel the way of scientific knowledge for the wellbeing of the world.

I am grateful to Dr Danqing Yin, a postdoctoral research fellow of the materials research group at City, for his kind support in educating me modelling with commercial software and also for subsequent guidance in my PhD.

My special thanks go to Professor B M A Rahman and Erasmus Mundus INTACT project for the financial support of this work. I would like to remember all my colleagues in my research group and of the school who used to be source of joy, inspirations and support during PhD. I would like to convey my special thanks to Nusrat Tamanna, Xiang Liu, Hassan Kassem, Mrs. Bhagya Dasari, Abdullah Qaban, Rahul Kumar, Qian Li, Alberto Bonifacio, Naumana Ayub imparting knowledge through peer learning process which was really helpful.

# Declaration

I hereby certify that this material, which I now submit for assessment on the programme of study leading to the award of Ph.D. is entirely my own work, that I have exercised reasonable care to ensure that the work is original, and does not to the best of my knowledge breach any law of copyright, and has not been taken from the work of others save and to the extent that such work has been cited and acknowledged within the text of my work.

Name: Israt Rumana Kabir

Sign: \_\_\_\_\_

Date: \_\_\_\_\_

# Preface

This thesis presents original work on modelling of laser surface glazing (LSG) for metallic materials by finite element method. The research work has been conducted in the School of Mathematics, Computer Science and Engineering of City, University of London for the period of July 2014 until July 2018. This work has been disseminated through the following publications and conferences

## Journal

- I.R. Kabir, D. Yin, N. Tamanna and S. Naher. Thermomechanical modelling of laser surface glazing for H13 tool steel. *Applied Physics A-Materials Science & Processing*, 2018, **124**, 3, doi:10.1007/s00339-018-1671-9.
- I. R. Kabir, D. Yin and S. Naher 3D Thermal Model of Laser Surface Glazing for Ti6Al4V, submitted, Manuscript ID is applsci-219141, *Applied Sciences: Laser Processing for Bioengineering Applications*, IF-1.73.
- N. Tamanna, R. Crouch, I.R. Kabir, and S. Naher, An analytical model to predict and minimize the residual stress of laser cladding process. *Applied Physics A-Materials Science & Processing*, 2018, **124**, 2, doi:10.1007/s00339-018-1585-6.

## Conferences

- I.R. Kabir, D. Yin and S. Naher, Thermo-structural coupled model for laser glazing, Accepted and presented, *International Conference on Laser ablation (COLA)* 3-8th September, Marcelle, France, 2017.
- I.R. Kabir, , D. Yin and S. Naher, 3D Thermal Model of Laser Surface Glazing for H13 Tool Steel, *20<sup>th</sup> International ESAFORM Conference on Material Forming, ESAFORM 2017*, 24-27th April, Dublin City University , Dublin, Ireland, 2017.
- I.R. Kabir, D. Yin and S. Naher, Two dimensional finite element thermal model of laser surface glazing for H13 tool steel, *19<sup>th</sup> International ESAFORM Conference on Material Forming, ESAFORM 2016*; Nantes; France; 27 April 2016 through 29 April 2016, Code 124421, AIP Conference Proceedings, Volume **1769**, Article number 11000319, October 2016.

# Abstract

Laser surface glazing (LSG) is widely used to improve surface hardness and wear resistance in casting tool, railroad, automotive and bioimplant industries. This PhD project focused on developing a simple and reliable model of LSG for metallic materials by FEM. Both 2D and 3D transient thermal model of LSG with cylindrical geometry were successfully developed in ANSYS mechanical APDL software. Temperature distributions, heating, cooling rates and depth of modified zone of LSG treated parts were predicted from the thermal model. The temperature distribution resulting from thermal model were used to develop a 2D coupled thermomechanical model to predict residual stress for H13 tool steel using two plasticity theories, isotropic and kinematic. The thermal model was conducted for H13 tool steel and Ti6Al4V alloy. The laser power range 200-300 W and 100-200 W were used respectively with constant 0.2 mm beam width and 0.15 ms residence time. Results showed that surface peak temperature increased proportionally with laser power. Heating and cooling rates were extremely high in the range of  $10^6$ - $10^7$   $Ks^{-1}$  for both alloys and increased with laser power. The depth of modified zone was in micron range and increased with laser power. The parametric study of thermal model determined threshold power level 210 W and 130 W to initiate melting of H13 tool steel and Ti6Al4V alloy respectively. Thermomechanical model showed that tensile residual stress induced in the modified surface of H13 tool steel. Isotropic plasticity model developed higher von Mises residual stress than the kinematic model. Furthermore, the developed thermal model of LSG was applied to simulate quenching and tempering heat treatment of structural steel. The temperature distribution, cooling rates and outer case depth caused by quenching were predicted from the model. The calculated case depth from the model showed good agreement with the measured case depth found in the experimental work.

Dedicated to

My parents

Mrs Shahana Begum and Mr Anwarul Kabir

My teacher

Ms Farida Yasmin

# Chapter 1

## Introduction

The need for variational properties with homogeneous microstructure in metals and alloys used for tooling, automotive, biomedical industries is a formidable challenge currently faced by the materials science researchers [1,2]. For example, metal casting mould needs to have high wear resistance along with high toughness and strength, to sustain against severe abrasion during casting [3]. Enhanced strength and wear resistance with better lubricity are necessary and demanding properties in rail road track [4]. Of bioimplant materials, high surface hardness is essential along with better corrosion resistance and biocompatibility [5]. Bringing several properties in a bulk material can be impractical or complex to process. It is well known that in general, if hardness increases then the ductility decreases. In this respect, laser surface treatments such as laser surface glazing (LSG), selective laser melting (SLM) and laser cladding (LC) by altering different surface properties than the bulk materials. Thus, these advanced laser technologies have eliminated the concern of populating several properties in a single part. This project has focused on the LSG process in surface hardening of metallic materials. LSG is a promising surface modification technique, which was first developed by two researchers Edward M. Breinan and Bernard H. Kear from the United technologies corporation in USA [6]. The glazing name appears to have come from the glassy phase which can be produced from the process, was reported in the New Scientist [7]. In LSG, high power density of the order of  $10^8$ - $10^{11}$   $\text{Wm}^{-2}$  [1] and faster interaction time within the range of  $10^{-4}$ - $10^{-6}$  s, [8] produce ultra-fast cooling rates, depending on thermal gradient and material properties ( $10^5$ - $10^8$   $\text{Ks}^{-1}$ ) [2,8], after melting the surface of materials. This results into very hard, thin and smooth modified surface with amorphous or semi-

crystalline microstructures [3]. Figure 1.1a is showing an experimental arrangement of LSG process with a cylindrical sample. When laser scans over the surface of the sample it modifies the surface microstructure as well as properties. The micrograph of the LSG treated sample has been presented in Figure 1.1b.

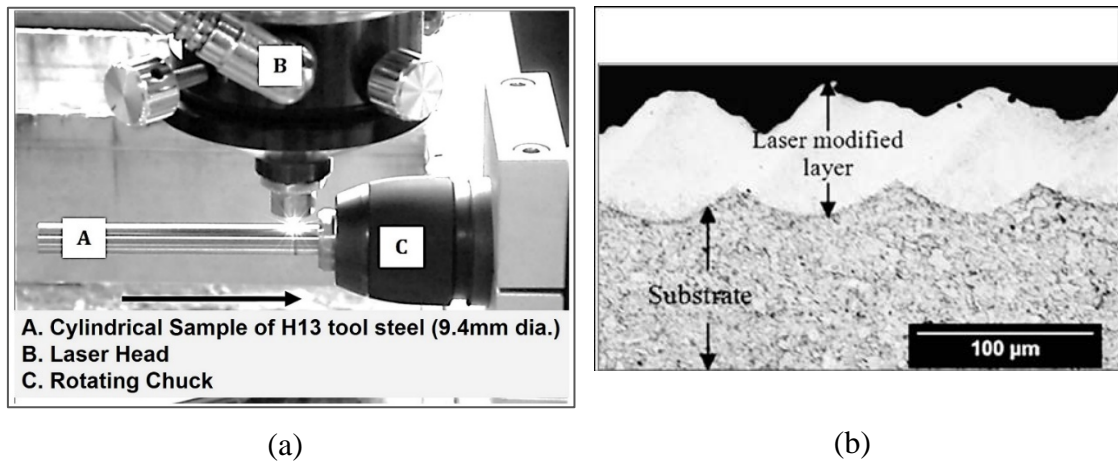


Figure 1. 1 (a) Experimental arrangement of LSG, (b) laser modified surface [3]

The major advantages and disadvantages have been listed as follows.

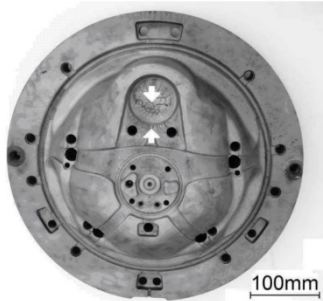
### Advantages

- Enhanced properties such as hardness, wear resistance, fatigue resistance, corrosion resistance
- No additional material is needed to modify the surface
- High heating and cooling rates ( $10^4$ - $10^8$  Ks<sup>-1</sup>) are achieved through LSG
- It is a fast and efficient process
- LSG has localization capability
- No distortion of the parts occurs

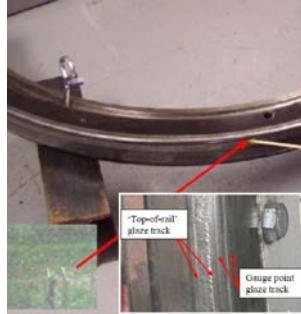
### Disadvantages

- Surface properties achieved are sensitive to process parameters
- Post stress-relieving is required after LSG

There are several applications of LSG are illustrated in Figure 1.2. The major applications of LSG are in casting tool, rail-road and bioimplant industries including automotive and aerospace applications.



(a) Hot work tool steel pressure die casting tool [9–11]



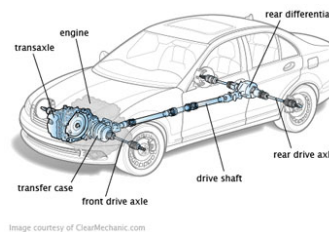
(b) 1080 steel glazed railroad track [4]



(c) Ti-6Al-4V in bio Implants [5]



(d) 7000 aluminium alloy in aerospace components - wing and fuselage shell [12]



(e) Axle, cam, brakes [13,14]

Figure 1. 2 Application of LSG process

LSG is relatively an inexpensive process with greater reproducibility and controllability in rapid solidification [1]. Kear et al. reported that high melting efficiency can be attained in LSG, which means most of the thermal energy is absorbed by the surface causing melting, very little thermal energy left in heating up the bulk solid part. This is the reason behind the extremely fast solidification [8] clearly from the localised heating with a defocused laser beam (0.09-0.4 mm) [3,15]. LSG can handle various materials including metals, alloys and ceramics. It can produce variety of novel and extremely homogeneous microstructures such as amorphous, supersaturated solid solution phases, metastable phases, ultrafine eutectics and refined dendritic structures [1,8]. These tailor-made

structures of the surface are responsible to improve hardness and wear resistance. Such surface also increases fatigue strength of the metal. One of the major advantages of LSG is that it creates a thin surface layer of several micrometres retaining the bulk material unaltered and relatively soft which gives a combination of properties to the metallic parts. However, application with the amorphous structure of LSG treated part is limited to the lower temperature just below the instantaneous glass transition temperature of the material. Other ultra-microcrystalline and controlled phase decompositions structures can be used in elevated temperature [1]. The critical point with LSG is to control the thickness of the glazed layer which is directly related to the melt zone produced by LSG. The melt depth depends on the power density and interaction time. With increasing melt depth, cooling rate decreases and to obtain the chilling effect, the cooling rates need to be above  $10^4 \text{ Ks}^{-1}$ , generally for metals [2,8]. Achieving the required cooling with thickness of the glazed layer is one of the biggest challenges in LSG, which need to be investigated by parametric optimisation of the process. Additionally, due to the rapid solidification, the development of residual stress is generally common in LSG, although, it is reported that no crack formation tendency was revealed by the LSG treated parts [8]. Nevertheless, the correct distribution and nature of residual stress induced in LSG is essential to know to predict its effect in service and to seek necessary measures in minimising it. Experimental studies of process optimisation take a lot of time and incur cost. Modelling and simulation offer an alternative way of making substantial trials to parameter optimisation and deeper understanding in details of multiphysics underpinned in LSG. Figure 1.3 has well-explained the need for modelling of LSG process because of large number of process parameters involved in the process.

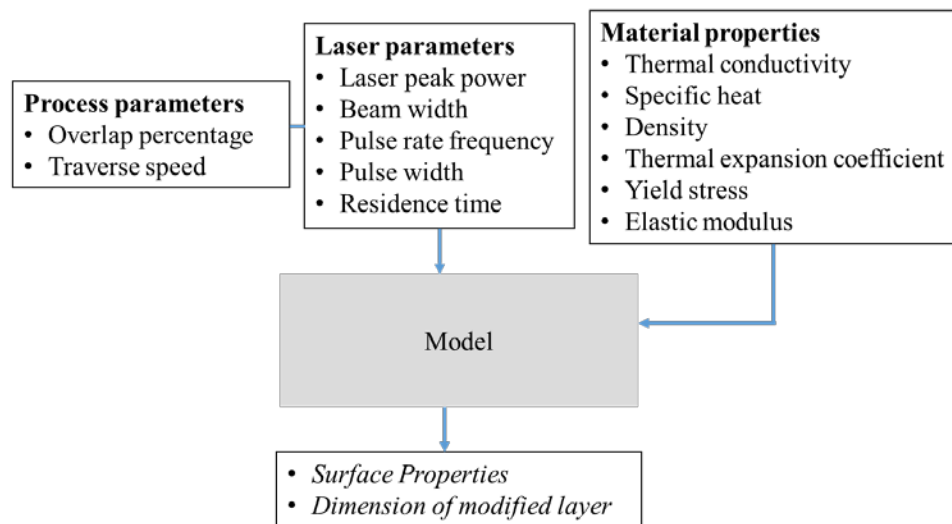


Figure 1. 3 Necessity for optimisation of laser parameters through modelling

Over the last three decades, there are numerous modelling works conducted for various laser materials processing including laser welding [16–18], laser cladding [19,20] and transformation hardening [21,22]. However, a few modelling works of LSG have been reported. A detail literature survey on the modelling works in LSG will be presented in chapter two in this thesis. In modelling, finite element method (FEM) is now widely used for various engineering problems using practical geometry of any shape and sizes. The thermal effects and interdisciplinary features of LSG process can be coupled well with FEM and investigated in detail to optimise process parameters and to predict its subsequent effects on the properties of the modified surface of metals and alloys.

The aforementioned account portrays that LSG is a very powerful and potential process for the surface treatments of various metals and alloys. However, the extremely fast nature of the process needs control and further detailed study for scaling-up the process and commercialisation. The modelling can play significant role towards this aim. Therefore, the project aim is to develop a reliable model of LSG using FEM which can predict the laser modified surface properties including hardness and be a useful tool for parameter optimisation for treated metals prior to the implement. The model will be helpful to understand the physical phenomena and their coupling effect involved in the LSG

process. As LSG is a surface heat treatment process, so the initiative will be taken to develop an accurate thermal model of heat transfer with laser energy coupling on materials surface which can predict the temperature distribution and the subsequent thermal effects on surface and subsurface regime. Therefore, the objectives of this PhD project have been set out as follows in line with the allocated time frame.

1. To develop 2D and 3D FEM thermal model for LSG to predict temperature distribution, depth of modified zone, heating and cooling rates.
  - To carry out parametric studies of the developed 3D thermal model for different materials and process conditions.
2. To develop a 2D FEM thermomechanical model for LSG coupling with the thermal model to predict the residual stress.
3. To verify the LSG thermal model, the methodology has been used to simulate similar heat treatment process, quenching and tempering of thermomechanically treated (TMT) steel bar to predict hardened outer case depth and compare it with the experimental results.

It should be noted that the first objective, developing a FEM thermal model of LSG to predict temperature distribution and heating cooling rates, is prerequisite to fulfil the subsequent steps. Because of LSG is a heat treatment process and temperature distribution plays vital role to alter microstructure and in deciding the surface properties of the heat-treated surface. That is why, a reasonable and reliable thermal model is important to the development of LSG.

## **1.1 Thesis structure**

The thesis consists of seven chapters. Chapter one presents the background of the problem and proposed aims and objectives with a brief outline of the whole thesis. Then, Chapter two deals with the literature survey on existing thermal, thermomechanical and other

models of LSG and similar laser melting processes. The important aspects in developing LSG modelling from the literature review have also been described relating to the objectives of the thesis. The third chapter and subsequent chapters will present the author's own works and contributions. In Chapter three, development of thermal modelling for LSG will be presented with the methodology, results and discussion progressively. Next, Chapter four will describe the establishment of thermomechanical coupled model using FEM. The residual stress distribution in surface or subsurface area treated with LSG process will be predicted in this chapter. In Chapter five, a parametric study of thermal FEM model of LSG will be presented. The parametric study is conducted based on ranges of laser power, types of material and heat source model applied in LSG modelling. Following this, the algorithm developed in LSG thermal model will be utilised in a different heat treatment process called quenching and tempering of TMT in Chapter six. The purpose of this chapter is to verify the present developed FEM methodology of LSG thermal model. This chapter will introduce the reader with the TMT process and its use and how the present FEM thermal model can be used to predict depth of hardened area of TMT treated bar after quenching and tempering. Finally, in Chapter seven, the principal findings of the research will be highlighted and concluded. Some specific and important future recommendations to broaden the horizon of the study will also be presented in this chapter.

-----X-----

# Chapter 2

## Literature review

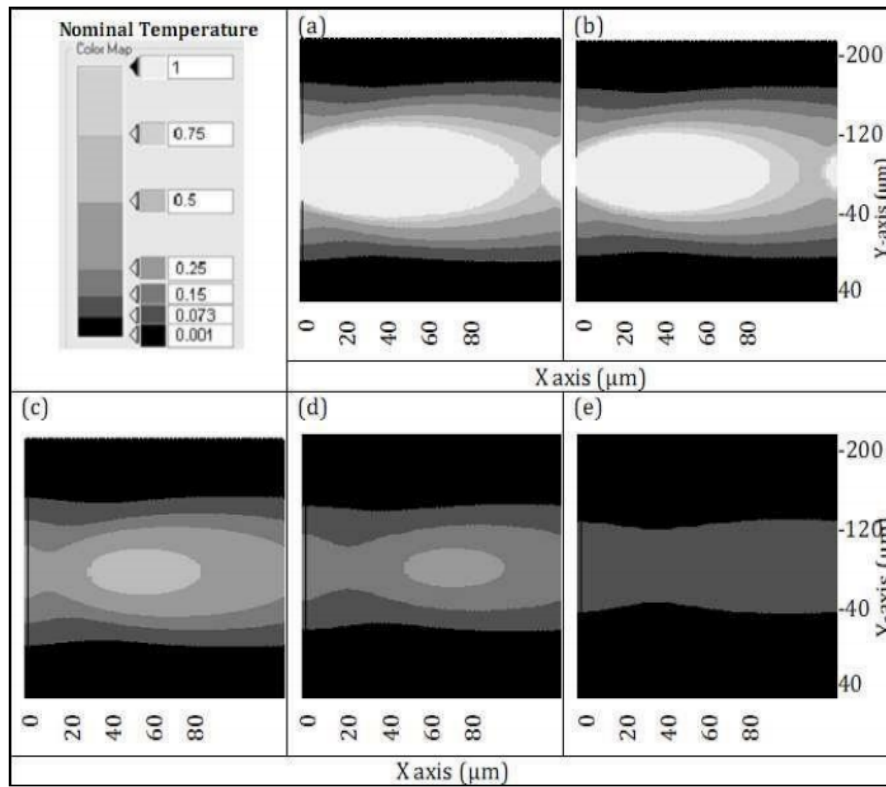
The literature review chapter has been discussed the progress in numerical thermal, thermomechanical modelling of laser melting processes including laser surface glazing (LSG), laser welding (LW), laser cladding (LC) and selective laser melting (SLM). Hardness modelling of laser modification techniques has briefly been discussed. After that, the salient controlling factors in the development of numerical models for the laser melting processes have also been outlined from the literature survey.

### 2.1 Thermal modelling of Laser Surface Glazing and similar processes

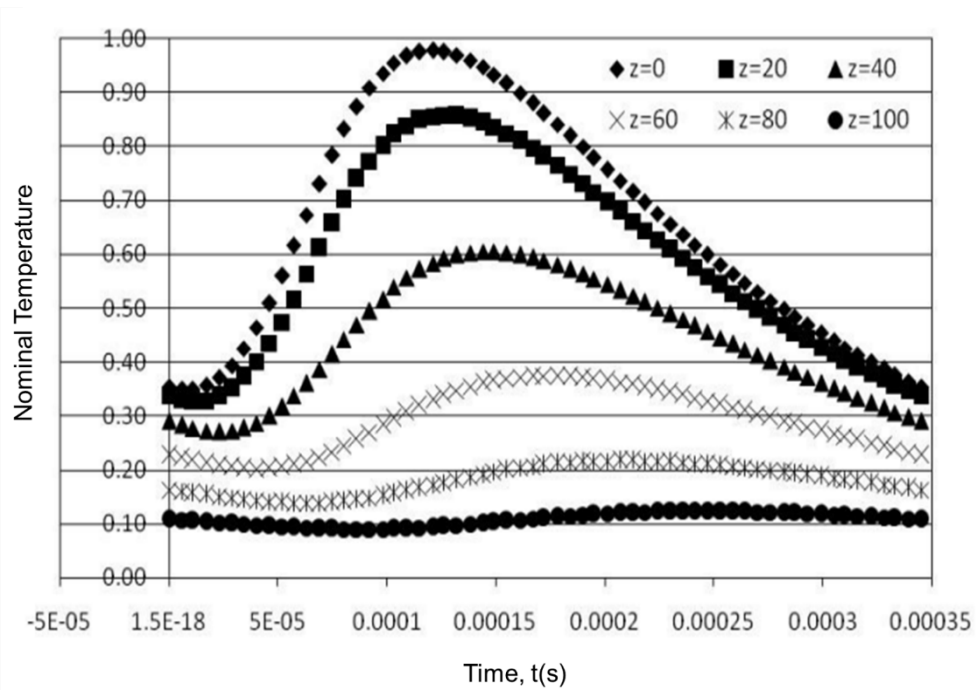
Over the last decade, there are numerous thermal modelling works of laser surface modification processes being carried out. The major purpose of the thermal modelling is to study the underpinned physical phenomena, predict temperature distribution [23], thermal effects [24,25] on surface of the treated part and subsequently to optimise the processes [26]. Through thermal modelling extensive numbers of trials can be performed in reduced cost and time unlike the experimental procedures. The physics of laser surface modification techniques, for their very fast nature deviates from the equilibria. Therefore, the heat transfer phenomena of such processes are complex to describe with the simple analytical modelling. Furthermore, along with a wide range of process parameters, laser absorption and material properties, all play key role in regulating heat transfer phenomena in the laser surface modification techniques. In this respect, the numerical thermal modelling technique has overcome the problem for the research and development of laser surface modification processes. This section of the thesis will review some recent numerical thermal modelling works of LSG, LW, LC and SLM to explore the parameters, materials and method used for those models and the outcome of those modelling works.

### 2.1.1 Laser Surface Glazing

Since LSG is introduced, very few modelling-works of LSG for metallic materials were carried out. Single numerical model of LSG for metallic and ceramic thermal barrier coating was developed by Mahank in 2004 [27]. The 2D thermal model of LSG was carried out using FDM method and predicted temperature distribution and dimension of laser glazed tracks. Temperature-dependant materials properties and variable absorptivity of metallic and ceramic materials were employed in this model. Later in 2011 [3], a thermal model of LSG of H13 tool steel to predict temperature distribution and dimension of melt pool was proposed using an explicit solution. The model used constant properties of steel and predicted nominal temperature distribution of the treated surface [28]. Figure 2.1a shows the isothermal temperature profiles on XY plane at five different thickness along Z direction from this model. The nominal temperature distribution was used in plotting the heating and cooling cycle at different depths from the surface, shown in Figure 2.1b. Besides there are few analytical models considering the modes of heat transfers conducted to predict melt pool geometry in laser glazing of ceramic materials [29–31]. All these models have a single primary goal which is predicting the temperature distribution; because, the temperature is the decisive factor to the outcome of all laser melting processes. The temperature profile and temperature history obtained from the simulation are utilised to further investigate the dimension of laser modified zone, possible phase transformation, hardness properties, thermal stress, distortion, cracks and so on. Therefore, it is very important to develop a reliable model that can predict temperature distribution and other outcomes.



(a)



(b)

Figure 2. 1 (a) Temperature distribution along X, Y and Z axis on the surface (b)

Thermal cycles at different depths from surface [28]

### 2.1.2 Laser Welding

Laser welding is a non-contact welding process to join metal pieces by scanning high power laser beam over the weld zone. The substantial number of modelling works in laser welding [32–34] manifests intense research and development program in this field. Temperature history, dimension of fusion zone, heat-affected zone (HAZ) [23,35,36], weld shape geometry [26,37], optimisation of laser welding process [34] have been predicted through FEM thermal modelling. Different software such as ABAQUS [34], SYSWELD [33] and ANSYS [17] have been utilized for developing the model and calculating output parameters. In LW process, high range of laser power 2.5 to 8 kW has been observed to process steels, whereas the non-ferrous alloy, for example, Ti6Al4V, Zircaloy 4 (Zr-1.4Sn-0.1Cr-0.2Fe), were operated with lower laser power. An exception in non-ferrous alloy is aluminium alloy, which was welded at 3 kW laser power. Laser scanning speed also observed to vary from 4 to 40  $\text{mms}^{-1}$  and laser spot size ranges from 0.2 to 1 mm depending on materials and processes. Different laser types were used for high power requirement of LW processes, among them CO<sub>2</sub> laser, Yb-YAG (ytterbium-yttrium aluminium garnet), fiber, and Nd-YAG lasers exert high power in descending manner. Moreover, some hybrid LW combining with arc current [38], MIG [35] or GTAW [17] processes were also modelled for various metals and geometries. The comparison between pure LW and hybrid welding was carried out through modelling [32]. Table 2.1 shows the laser parameters used in laser welding processes for different metals and alloys. From the thermal modelling of LW the temperature distribution, depth of weld pool and HAZ, cooling rates have been investigated. The effect of laser power, scanning speed on temperature distribution, size of fusion zone and cooling rates also have been analysed.

Table 2. 1 Thermal models of LW process for various materials and laser parameters including key findings

Materials/ Laser type	Laser parameters			Method/Software	Findings	Year	Ref.
	Power, kW	Beam width, mm	Scanning speed/RT <sup>1</sup> , mms <sup>-1</sup> , s				
6065 Al alloy, Nd:YAG, CW	3	0.45	10 <sup>-3</sup>	FEM, ABAQUS	Fluctuations of the absorbed laser beam power generate cooling speed deviations leading to the distortion	2013	[34]
Zircaloy 4, Nd:YAG, Pulse	0.3-0.9	1	4	FEM, SYSWELD	With increasing power, the size of the weld pool increases, 9% accuracy is reported of the numerical model	2012	[33]
Ti6Al4V	0.5-1.5	-	5.2	FEM, ANSYS 14.5	The peak temperature increases with laser power nonlinearly, bead geometry also changes with laser beam power	2014	[36]
Ti6Al4V, CO <sub>2</sub> , CW	1.7	-	13.34,40	FEM, SYSWELD	With increasing laser speed, the size of weld bead decreases	2015	[26]
Ti6Al4V, Nd:YAG, Pulse	0.24	0.7	3-9	FVM, SIMPLE algorithm	With decreasing laser welding speed, the peak temperature increases and the penetration depth increases. The numerical error was found maximum 17%	2014	[23]
Alloy steel, CO <sub>2</sub> , CW	8	0.5	25	FEM, SYSWELD	At 8 kW and 25 mms-1, fusion zone and HAZ cools down at 100 Ks-1 average cooling rate	2014	[39]

1. RT=Residence time 2. CW=Continuous Wave

### 2.1.3 Laser Cladding

Laser cladding is a surface modification technique where external material in powder or wire form is deposited on a substrate utilising scanning laser beam, the additional material is called clad [19]. The mixture of clad and substrate at the interface is called dilution zone. Temperature distribution in clad and substrate, dimension of clad, cooling rates were predicted from different FEM thermal model of LC [24,25,40,41]. The depth of dilution can also be predicted and controlled by optimising parameters through modelling [20]. In thermal modelling of LC, the range of processing power was observed to vary from 0.6 to 4 kW depending upon materials and geometries. Unlike LW, beam width or spot size differs from 1 mm [24] up to 12 mm of both spherical [20] and rectangular shape [25, 40] of laser beam. Table 2.2 summarizes technical information and the key findings from recent thermal modelling works of LC. The materials used for clad and substrate, laser type, laser parameters, numerical methods and software used have been enlisted. The effects of laser power, scanning speed in peak temperature in the clad, cooling rates, width of melt pool were analysed in those models. Relationship between melt pool width and dilution zone was also analysed through modelling. Comparing Table 2.1 and Table 2.2 it is understood higher level of laser power and faster scanning speed were applied in LW than LC. However, these values of parameters mainly depend on type of material been treated. Both spherical and rectangular laser beam were used in LC processes. Larger beam diameter was used in LC whereas comparatively small diameter was applied in LW process. The size of beam diameter determines the total heat flux applied and scanning speed is adjusted accordingly.

Table 2. 2 Thermal models of LC process with different materials and process parameters including key findings

Clad/Substrate	Laser type	Laser parameters			Method, Software	Findings	Year	Ref.
		Power, kW	Beam width, mm	Scanning Speed, mms <sup>-1</sup>				
H13 TS/mild steel	HPDDL (975 nm)	3.8	12×3	3-7	FEM, ANSYS	Peak temperature reaches 1850 °C at 5 mms <sup>-1</sup> speed, 370 °C higher than the melting point of H13. With increasing scanning speed, the cooling rate increases, and size of melt pool decreases	2014	[25]
Stellite (Co-Cr alloy)/mild steel	Nd:YAG, CW	0.6-4	3-4.5	5-20	FEM, COMSOL	Melt pool width is smaller than the critical value which is about 90% of the laser beam width, the dilution level is small	2011	[20]
Ti6Al4V/Ti6Al4V	Nd:YAG	0.4-0.6	0.8-1.8	8.33-11.66	FEM, ANSYS	With increasing laser power, the depth of melt pool increases, error in predicted results is claimed maximum 3.16% than the experimental	2013	[19]
H13 TS/AISI 4140 steel	HPDDL (808 nm)	1.4-1.8	12×1	6-9	FEM, ANSYS 11	The average peak temperature and cooling rate are predicted 1729 °C and 1300 °Cs <sup>-1</sup> respectively in clad of H13, for power 1.6 kW and 7 mms <sup>-1</sup> speed	2011	[40]

#### 2.1.4 Selective Laser Melting

Selective laser melting is a process of rapid prototyping which creates mechanical parts layer-by-layer scanning laser beam over the powder beds of materials [42]. A significant number of numerical thermal modelling of SLM are also published in this field. Table 2.3 has presented the information summary of some numerical thermal models of SLM processes. The table has included types of materials and laser, process parameters, and key findings from those models. SLM processes use distinctly smaller beam width ranging from 0.01 to 0.3 mm. Comparing with other laser melting processes, lower laser power from 110 W to 320 W and higher scanning speed varying 200 to 1939  $\text{mms}^{-1}$  were reported to operate SLM for Ti6Al4V, aluminium (Al) and copper-ceramic composite [43–45]. Thermal modelling of SLM can predict the temperature distribution, dimension of melt pool and optimise process parameters [43]. The relative density and pore size can also be calculated through thermal modelling of SLM which need coupling fluid flow dynamics with heat transfer mechanism [46].

From reviewing those modelling works of laser melting processes the possible outcome and state-of-the-art of numerical laser modelling have been realised. The effects of some parameters including types of material and laser heat source to develop a successful numerical thermal models of laser melting processes have also been understood which will be described in subsequent sections. As it is obvious that very high peak power and cooling rates are achieved in those processes which eventually lead to induce thermal residual stress in the treated parts. The temperature distribution data from the thermal model can be further used to predict the residual stress through thermomechanical models of laser melting processes.

Table 2. 3 Thermal models of SLM or LSM for various materials and process parameters including key findings

Material	Laser type	Laser parameters			Method/Software	Findings	Year	Ref.
		Power, kW	Beam width, mm	Scanning Speed, $\text{mms}^{-1}$				
Ti6Al4V powder	Yb fiber, CW	0.11	0.034	200	FEM, ANSYS 10	0.11 kW laser power and $200 \text{ mms}^{-1}$ is selected by simulation of SLM process which gives maximum depth, $45 \mu\text{m}$ of molten powder layer in $50 \mu\text{m}$ powder bed thickness	2012	[43]
Cu, Tungsten Carbide (WC) composite powder	$\text{CO}_2$ , CW	0.6-0.9	0.3	-	FVM, Fluent 6.3.26	At $17.5 \text{ kJm}^{-1}$ linear energy density (LED) 96% density has achieved. The melt pool sizes are in hundreds of micrometres and increase with LED	2014	[46]
Al-1.5 Fe	Yb fiber, CW	0.6	0.3	40-80	FEM, ANSYS	The depth and width of melt pool increases with decreasing scanning speed linearly. Molten pool loses its regular form at lower than $30 \text{ mms}^{-1}$	2011	[47]

## 2.2 Residual stress of laser melting processes

The localised melting of the surface and remaining cold bulk material result in steep thermal gradient and rapid cooling rates ( $10^5$ - $10^8$  Ks<sup>-1</sup>) [2,47] in the laser melting processes. This large temperature gradient causes non-uniform thermal expansion and contraction between surface and the bulk, which creates irregular distribution of thermal load inside the treated parts. Moreover, the rapid cooling rates encourage diffusion-less phase transformations which incurs micro strain in the treated zone due to the difference in volume of the phases. These phenomena eventually lead to the formation of residual stresses in the laser treated region, interface and the bulk. Dai et al. [46] reported that  $3.9 \times 10^5$  Km<sup>-1</sup> temperature gradient was observed during a SLM process of Cu-WC composite, which was indicative to the presence of significantly high stress field leading to crack formation depending on the type of residual stress. Residual stress in the laser treated surface can be tensile or compressive in nature. It is diverged in type and magnitude for different laser melting processes, materials and parameters. For instance, compressive residual stress was found in a laser cladding process operated by fiber coupled diode laser both in continuous wave and pulse modes. In this process, powder H13 tool steel was cladded on a tempered H13 tool steel substrate. It was reported that, the magnitude of compressive residual stress in the clad was higher in the process operated in pulse laser mode than in continuous wave mode, at equal 133 Jmm<sup>-1</sup> laser energy density. In addition, the increment of compressive residual stress for pulse mode differs for pulse frequency and pulse duration [48]. On the other hand, in laser surface melting of H13 tool steel, tensile residual stress was observed and measured which can reduce the fatigue strength and toughness resulting into crack formation of the treated part at 100 Jmm<sup>-2</sup> energy density after melting occurred. Figure 2.2 has presented the variation in type and magnitude of the average surface stress measured along the scanning direction. It is reported that at lower laser energy the surface stress was compressive due

to the phase change effect. However, at higher energy the tensile stress has been developed due to the solid to liquid phase change [49]. Well, there is exception of the magnitude of stress on the surface at lower energy, because it also depends on other factors including type of materials and nature of constraints. Through thermomechanical modelling of those processes, it is easier to predict the nature and magnitude of the residual stresses. Moreover, the mechanism of residual stress development or tendency of crack formation can also be studied through this modelling. Optimisation of process parameters in minimising induced residual stress during laser melting processes can also be carried out efficiently and effectively.

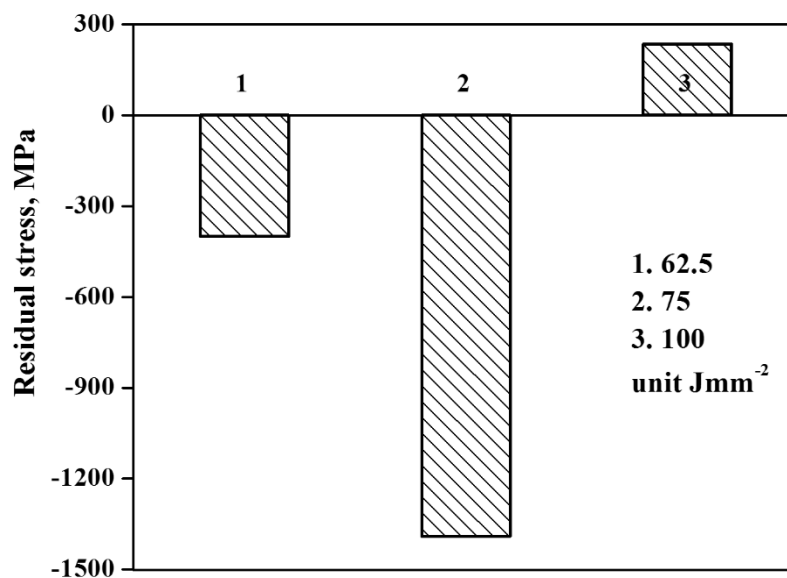


Figure 2. 2 Variation in residual stresses with laser energy density, when surface experience melting the compressive residual stress transforms to tensile [49]

### 2.2.1 Thermomechanical modelling of laser melting processes

For last few years, several works on developing thermomechanical models [17,50–52] of laser melting processes were carried out to predict the residual stresses for different metals and alloys. This section will review some of the recent numerical thermomechanical

models of LW, laser Additive Layer Manufacturing (ALM), Laser Engineered Net-Shaping (LENS), and LC processes. For example, 3D FEM thermomechanical model of hybrid laser-GTAW (Gas Tungsten arc welding) welding process of AISI 1018 steel plates was carried out using ANSYS. The model predicted tensile normal stress in the fusion zone and compressive in the heat-affected zone (HAZ) [17]. LC of stellite (57% Cobalt-28-38% Chromium alloy) powder on the stainless steel substrate was conducted with CW CO<sub>2</sub> laser. The thermomechanical modelling of this process predicted compressive residual stress in the surface of the clad and tensile stress in just below the surface spreading up to interface [53]. Another modelling work of LC also reported similar pattern of residual stress found in clad, interface and substrate [54]. In other models, the effects of laser parameter such as scanning speed and laser power on residual stress were also analysed. For instance, LSM process of 42Cr4Mo steel operated by wide band laser with rectangular heat source, the effect of laser scanning speed on stress fields was evaluated [55]. The model predicted that at low scanning speed compressive residual stress was observed on the surface. However, at higher scanning speed the stress component on the surface turned to tensile in nature. Then, laser melting in ALM of Ti6Al4V alloy powder was modelled using ANSYS FEM solver. This model predicted compressive residual stress on surface layer and correlated with scanning speed. It was reported that decrease in scanning speed increased the longitudinal stress of the Ti6Al4V surface layer [51]. The stress component along the direction of laser scanning is known as the longitudinal stress. 3D thermomechanical models of LENS processes for two different materials were also reviewed. The LENS process also lies in the additive manufacturing process family. In this process, computer aided designed parts are built up in layer-by-layer scanning over the powder metals, similar to the selective laser melting or rapid prototyping. Those models revealed compressive stress in the middle of the surface layer, while tensile stress at the free-ends [56,57]. Important technical information

including treated materials, laser parameters and software used to develop those FEM thermomechanical models of laser melting processes have been enlisted in Table 2.4.

Table 2. 4 Materials, software and parameters used in FEM thermomechanical models of some laser melting processes

Process name	Materials	Laser type	Laser parameters			Software	Ref.
			Power, kW	Beam width, mm	Scanning Speed, $\text{mms}^{-1}$		
LW	AISI 1018 steel	Fiber	2.5-3	0.6	25	ANSYS	[17]
ALM	Ti6Al4V powder	Nd:YAG	0.12	0.01	220	ANSYS	[51]
LENS	AISI 410 steel	Nd:YAG	0.254- 0.344 <sub>avg.</sub>	0.5-0.1	2.4-8.5	SYSWELD	[56]
LENS	H13 tool steel, base-Cu/H13	Nd:YAG	-	-	2-8	SYSWELD	[57]
LC	C/S <sup>1</sup> -Stellite/SS <sup>2</sup>	CW <sup>3</sup> Nd:YAG	1.5	2	5	ANSYS	[53]
LC	C/S <sup>1</sup> -Crucible steel/H13	CW CO <sub>2</sub>	2-3.8	3	200	ABAQUS	[54]
LSM	42Cr4Mo steel	CW CO <sub>2</sub>	3.5	10×1 <sup>4</sup>	2.4-8.5	SYSWELD	[55]
LSM	Al-10WC composite	Pulsed CO <sub>2</sub>	1.5 <sub>peak</sub>	0.3	100	ABAQUS	[52]

1. C/S=Clad/Substrate, 2. SS=stainless steel, 3. CW=Continuous wave, 4. Rectangular laser beam

All those models were developed in generally ANSYS, ABAQUS and SYSWELD commercial finite element solver using coupling techniques between thermal and structural/mechanical analyses. There are usually two kind of coupling techniques shown in Figure 2.2, followed in FEM thermomechanical modelling of the laser processes. Where the results of thermal analysis as thermal loads due to temperature gradient are input in a structural analysis to calculate stresses induced by those thermal loads with the co-efficient of thermal expansion or contraction of materials, is known as load transfer or sequential coupling. Most of the works in Table 2.5 used load transfer or sequential coupling method to calculate residual stress. However, a direct coupling technique based thermomechanical model of laser cladding was also observed [54]. In direct coupling, both thermal and structural analyses are simultaneously conducted by applying both thermal and mechanical boundary conditions together.

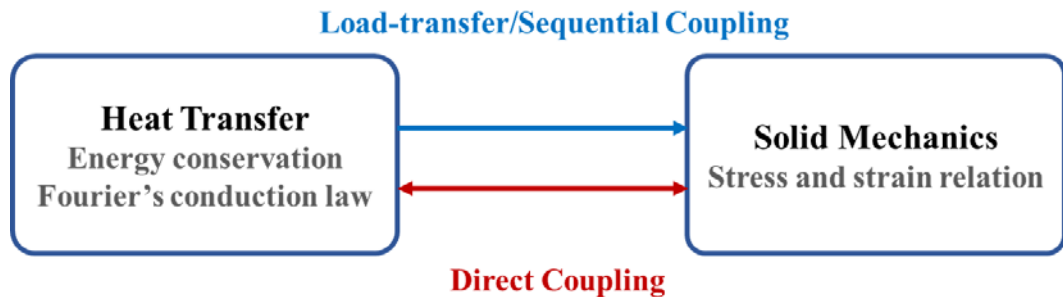


Figure 2. 3 Thermomechanical coupling used in laser melting processes

In those models, residual stress due to temperature gradient was calculated from total strain using classical thermo-elastic-plastic principle. The total strain,  $\epsilon^{total}$ , consists of mainly three parts as in,  $\epsilon^{total} = \epsilon^{th} + \epsilon^{el} + \epsilon^{pl}$ , where  $\epsilon^{th}$  is thermal strain,  $\epsilon^{el}$  is elastic strain and  $\epsilon^{pl}$  is plastic strain. The thermal strain is calculated from temperature dependent coefficient of thermal expansion or contraction, elastic strain follows linear Hooke's law for metals and alloys, plastic strain is calculated from Yield strength, hardening or plasticity models and flow rule of the materials. Two plasticity models,

isotropic and kinematic, have been observed to calculate plastic strain based on classical plasticity theory, details of plasticity models will be described in chapter four. It is observed from Table 2.5 that, most laser melting processes followed isotropic plasticity model. It is worth noting that from the literature review, no numerical thermomechanical model related to laser surface glazing of metallic materials was found in the literature.

Table 2. 5 The plasticity models and coupling techniques used in the thermomechanical model of laser melting processes

<b>Process name</b>	<b>Materials</b>	<b>Plasticity models</b>	<b>Coupling technique</b>	<b>Type of stress</b>	<b>Ref.</b>
LW	AISI 1018 steel	Isotropic	Sequential	Tensile stress in the weld and compression in HAZ	[17]
ALM	Ti6Al4V powder	Isotropic	Sequential	Compressive in the surface, tensile at below the surface and at interface	[51]
LENS	AISI 410 steel	Isotropic	Sequential	Compressive in the centre of the surface and tensile at the free edges	[56]
LENS	H13 tool steel, base-Cu/H13	Isotropic	Sequential	Compressive in the centre of the surface and tensile at the free edges, stress differs with base material type	[57]
LC	C/S <sup>1</sup> -Stellite/SS <sup>2</sup>	Isotropic	Sequential	Compressive-tensile-compressive at surface-interface-substrate	[53]
LC	C/S <sup>1</sup> -Crucible steel/H13	Kinematic	Direct Coupled	Compressive-tensile- compressive at surface-interface-substrate	[54]
LSM	42Cr4Mo steel	Kinematic	Sequential	Compressive at the surface, becomes tensile at higher scanning speed	[55]
LSM	Al-10WC composite	Isotropic	Sequential	Lower von Misses stress in the centre of circular surface and higher near the circumference due to spiral scanning strategy which caused self-annealing at centre	[52]

1. C/S=Clad/Substrate, 2. SS=stainless steel

### 2.3 Miscellaneous coupled model of laser melting processes

There are some other coupled models to predict surface hardness of laser surface melting process were also found in the literature. One method of modelling surface hardness was that coupling thermal model with empirical equations of phase transformation [21]. The heating and cooling curves were extracted from FEM thermal model of the process. Then, percentage of phase fraction were calculated using those curves utilising time-temperature-transformation (T-T-T) diagram of the treated materials following some empirical equations of phase transformation. Figure 2.4 is showing a schematic T-T-T diagram and the discretization into isothermal transformation time and temperature gradient, taken from literature. In T-T-T diagram, phase transformation curve profile is drawn from the measurement of volume fraction of phase with respect to time and temperature. In the figure,  $T_i$  is the temperature of  $i$ -th step corresponding to  $t_i$  time,  $\Delta T$  is the change in temperature between  $i$ -th and subsequent  $i+1$ -th time steps,  $y_i$  is the percentage volume fraction of  $y$ -phase at  $i$ -th step.

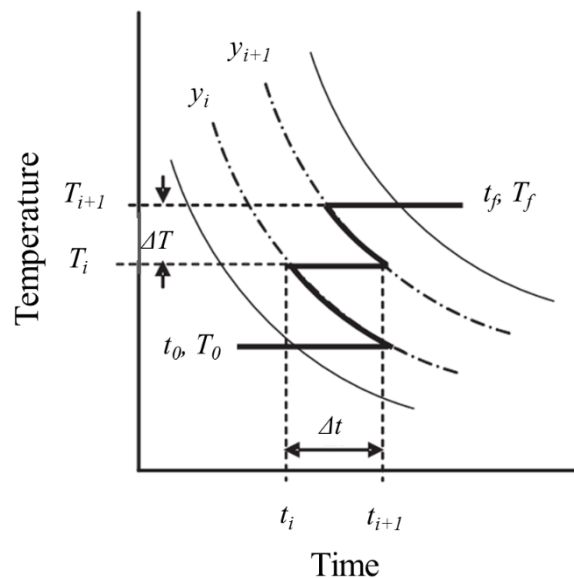


Figure 2. 4 A typical discretization technique of the T-T-T diagram for phase transformation modelling [21]

For the diffusion-controlled transformations, for example, ferrite, pearlite, austenite transformation, Kolmogorov-Johnson-Mehl-Avrami (KJMA) equation was used, shown in Equation 2.1.

$$V_{y,i} = V_y^{\max} \left[ 1 - e^{-b_k t_i^{n_k}} \right] \quad (2.1)$$

In Equation 2.1,  $V_{y,i}$  is the volume fraction of  $y$ -phase at each  $i$ -th step is related to isothermal transformation time  $t_i$ .  $V_y^{\max}$  is the maximum volume fraction of the phases that can be formed under the considered cooling rate. This equation is used for both heating and cooling stage phase transformation. On the other hand, Koistinen-Marburger equation was used for the displacive transformation such as martensite phase transformation [41,58]. The Equation 2.2 is used to calculate phase fraction from austenite to martensite phases.

$$V_{marten} = V_{aus} \left[ 1 - e^{-\gamma(M_s - T_{end})} \right], \quad (2.2)$$

where,  $V_{marten}$  is the volume fraction of martensite,  $V_{aus}$  volume fraction of austenite at martensitic start transformation temperature  $M_s$ ,  $T_{end}$  is end temperature. The coefficient  $\gamma$  depends on the composition of steel or other alloys. Then total hardness is calculated using rule of mixture for the corresponding phase fractions present in laser treated zone. For calculating hardness of tempered martensite another method called thermo-kinetic (TK) model was followed in isothermal conditions which is proposed by Reti et al. [59] followed in modelling of some other laser processes [40,58].

#### **2.4 Controlling factors in modelling of laser melting processes**

From the above literature review, it is observed that modelling of laser melting processes simplifies the physical phenomena through assumptions to find out the important factors which influence the process outcome. The most important factors which regulate the

thermomechanical models of laser melting processes are materials properties, heat source distribution, laser coupling efficiency and plasticity models. To increase the modelling accuracy, it is essential to optimise those factors relative to the processes.

#### 2.4.1 Material properties

The accuracy in predicted results of laser melting modelling is strongly dependent on the material properties employed into modelling. Material properties define the response under the application of laser heat flux in the laser melting process modelling. Specific heat, thermal conductivity, thermal expansion coefficient, Young's modulus, yield strength and Poisson's ratio are the general material properties involved in thermomechanical model of laser melting processes. As laser melting processes are heat treatment processes, therefore the dependency of the material properties on temperature is essential to account in modelling; especially specific heat capacity, thermal expansion coefficient, and thermal conductivity are temperature sensitive. It was reported that, the numerical discrepancies of theoretical and experimental findings of same process is due to the complex temperature-properties relation with equivalent process condition [60]. Some numerical and modelling works of laser processes used constant material properties [28,61,62], which showed very distinctive prediction with the model utilising temperature dependant material properties. It is noted that thermo-physical properties need tuning in many modelling works to conforming data with the experimental works. For example, in selective laser melting of Ti6Al4V powder operated with Yb fiber laser used temperature dependent specific heat ( $\text{Jkg}^{-1}\text{C}^{-1}$ ). Gaussian heat source was employed, and 0.25 value was set for absorptivity. The depth of melt pool was obtained  $40\ \mu\text{m}$  at  $200\ \text{mms}^{-1}$  scanning speed and 110 W laser power [43]. In another Yb fiber laser treated SLM of Ti6Al4V powder with equal scanning speed, achieved  $40\ \mu\text{m}$  melt depth at 80 W laser power presumably due to input specific enthalpy ( $\text{Jkg}^{-1}$ ) instead of specific heat [63]. This kind of adjustment of specific heat is also observed in laser cladding of

Ti6Al4V alloy to achieve correct melt pool dimension conforming with the experimental data [19].

Therefore, employing correct set of the temperature dependent material properties is prerequisite to ensuring accuracy in modelling of laser melting processes.

#### 2.4.2 Heat source model

In laser melting processes, the intensity of laser beam is transformed into thermal energy while irradiating the surface of the treated material. This thermal energy enters into the specimen as heat flux density or power density of absorbed laser beam. The power density is defined as the amount of thermal energy flow per unit surface area at unit time. The amount of thermal energy is decided by the spatial distribution of laser intensity on the surface or beam profile. Depending on the beam optics there are different kind of beam profile can be created. For example, spherical, elliptical, Gaussian, top-hat are the most common in laser melting processes [64]. Imagery software is used to determine the beam intensity profiles. In literature, most of the modelling work of laser melting processes used Gaussian or combination of Gaussian beam profiles such as  $TEM_{00}$  [23,36],  $TEM_{01}$  or combination of them [21], shown in Figure 2.3.

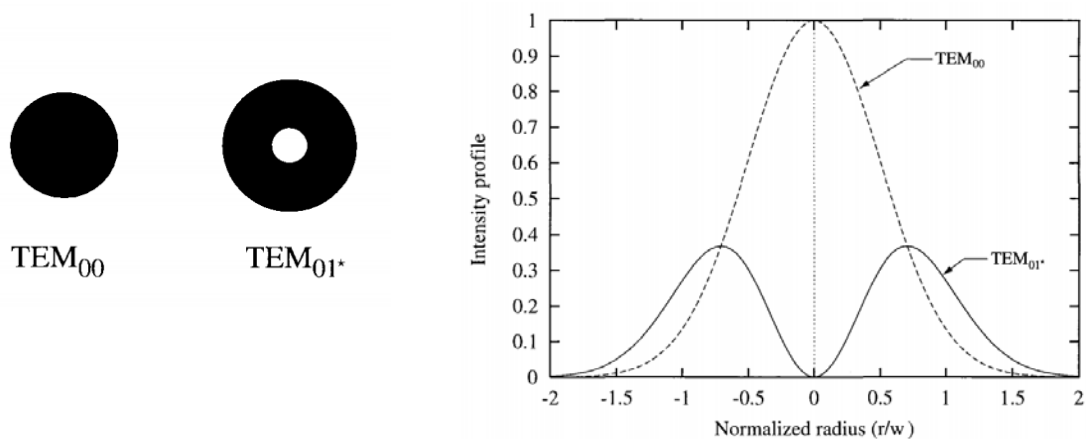


Figure 2. 5 The Transverse Electrical Mode (TEM) profile of intensity distribution of laser beam [27]

In case of Gaussian, the intensity distribution is symmetric along beam radius and in laser melting process symmetry is kept along the direction of scanning laser beam. In laser welding, double ellipsoidal Gaussian distribution of volumetric heat load is suitable [36], since Goldak introduced it for arc welding modelling [65]. A little modification in Goldak's ellipsoidal profile turned into Gaussian spherical distributed volumetric load was considered in laser cladding process to attain correct shape of melt pool [19]. The distribution of laser intensity is a key factor for correct prediction of thermal profile, not only magnitude of the temperature distribution but also the correct shape of the molten and modified zone. The mathematical equations for intensity distribution of various laser heat source have been enlisted in Table 2.6. It is observed that, most of the models utilised Gaussian distribution of laser intensity as volumetric and surface heat source. Volumetric heat source consists of three-dimensional distribution of laser intensity whereas surface heat source distributes in two dimensions. However, a uniform top-hat distribution was employed in a laser melting process using rectangular heat source [40], which was claimed to give good metallurgical bond, low porosity and minimum dimensional distortion [25]. The Gaussian beam profile gives more penetration as the intensity concentrates more towards the centre of the beam whereas the intensity of top hat beam profile is more uniform throughout the beam diameter [66]. Moreover, a volumetric conical heat source with Gaussian distribution was also used in laser engineered net-shaping. The volumetric conical distribution represents maximum penetration of the laser beam where it requires [56]. The parameters related to the laser beam profile used in those equations vary depending on laser mode such as continuous wave or pulse. Therefore, it is essential to calibrate heat source distribution and select correctly for the process modelling to ensure accuracy of the predicted temperature, melt pool profile and residual stress distribution.

Table 2. 6 Various heat source models applied in modelling of different laser melting processes

Processes	Laser type	Beam width, mm	Heat source model	Equations of heat flux density, q	Peak temperature, °C	Ref.
Laser engineered net-shaping	Nd:YAG	0.5-1	Gaussian volumetric conical	$\frac{2P}{\pi r_b^2} \left(1 - \frac{z}{H}\right) \exp\left(1 - \left(\frac{r}{r_b}\right)^2\right)$	1800-2200	[56]
Laser cladding	HPDDL	12×1 <sup>1</sup>	Top-hat uniform	$\frac{AP}{w \times 1}$	1729	[40]
Selective laser melting	Yb fiber	0.035	Gaussian heat flux density	$\frac{2AP}{\pi r_b^2} \exp\left(\frac{-2r^2}{r_b^2}\right)$	6000	[43]
Laser cladding	Nd:YAG	1.8	Gaussian volumetric spherical	$\frac{6AP}{\pi\sqrt{\pi}r_b^3} \exp\left(\frac{-3r^2}{r_b^2}\right)$	2810	[19]
Multi-pulse laser melting	Nd:YAG	0.4	Gaussian pulse heat flux density	$A \frac{E}{\tau\pi r_b^2} \exp\left(-\left(\frac{x - (x + vt)}{r_b}\right)^2\right)$	2750	[64]

1. Rectangular beam

### 2.4.3 Laser coupling efficiency or absorptivity

Laser coupling efficiency or absorptivity is another crucial factor in modelling laser processes effectively. It is the ratio of absorbed laser energy by the material to the total energy provided by laser beam, where no transmission of light through the materials is presumed [21]. In fact the absorptivity is accounted the loss of laser intensity due to reflection or scattering of light [67] as most of the metals reflect laser light [68]. Absorptivity of laser light mainly depends on the wavelength of light, temperature, surface roughness and composition of the material [69,70]. Absorptivity of some common metals with various wavelength has been presented in Figure 2.2.

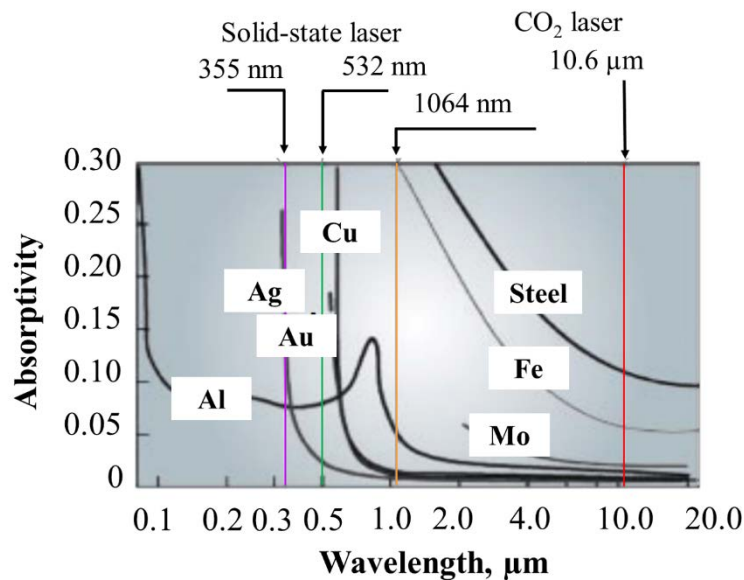


Figure 2. 6 Absorptivity of some metals at different wavelength [71]

It is noted that, Fe and steel can absorb laser light no more than 10-12% for CO<sub>2</sub> laser which is in far-infrared (10.6 μm) zone. All other metals Al, Cu, Mo, Au, Ag absorb very little in this wavelength. The Figure 2.6 is limited up to 30% absorptivity, because any as-received metals surface hardly absorb laser above that range in visible to infrared region. However, with pre-treatments such as sand blasting, chemical etching or painting

of those metals surface, the absorptivity can be enhanced by up to 80% [3,15]. Different values of laser absorptivity for various metals and laser type is listed in Table 2.7.

Table 2. 7 Variation of absorptivity depending on laser and material types in different laser surface modification processes

Process	Laser type	Materials	Absorptivity	References
Laser cladding	HPDDL (808 nm)	C+S <sup>1</sup> -H13 steel+mild steel	0.75	[40]
Laser cladding	HPDDL (975 nm)	C+S-H13 steel+mild steel	0.30	[25,41]
Laser assisted machining	Nd:YAG (1064 nm)	Ti6Al4V plate	0.34	[72]
Selective laser melting	Yb fiber laser (1064-1100 nm)	Ti6Al4V powder	0.25	[43]
Laser cladding	CO <sub>2</sub> (10600 nm)	C+S-TiC/NiCrBSiC+Ti6Al4V	0.30	[67]

1. C+S-Clad+Substrate

From the Table 2.7, it is observed that different absorption coefficient of Ti6Al4V alloy variably used in three distinct processes, laser assisted machining, selective laser melting and laser cladding. An experimental work of calculating absorptivity of Ti6Al4V plate surface revealed that, the value of absorptivity varied between 0.28-0.4 with temperature up to 1400°C. Therefore, an averaged value 0.34 was employed in the subsequent modelling work of laser assisted machining of Ti6Al4V alloy [72]. Additionally, another experimental and modelling work reported 0.45 absorptivity of Ti6Al4V flat-surface and increased to 0.71 for powder [73]. Although, in this modelling work [43] absorptivity for Ti6Al4V powder was adopted 0.25 to get accurate depth of laser melted zone. This kind of deviation in absorptivity of same material is observed in other works [25,40], because of its complex nature of dependency with various factors. It is worth-noting that this

absorption factor also play key role in deciding size and shape of the laser modified zone and enhancing the accuracy of laser process modelling [40,68,74].

#### 2.4.4 Plasticity models

Theoretical prediction of thermally induced residual stress through thermomechanical modelling of laser melting processes follows classical thermo-elasto-plastic constitutive law. Here, the total strain consists of thermal, elastic and plastic strain. In metals and alloys, yield strength is evolved due to plastic strain which eventually is added to the residual part. Similarly, in laser surface melting process, due to the thermal load generated in the surface causes plastic strain. The increment of this plastic strain can be calculated following three possible principle, (i) isotropic, (ii) kinematic and (iii) mixed plasticity models, based on material's response [51]. Therefore, it is important to select appropriate plasticity theory to correctly calculate residual stress from the thermomechanical models. In literature, separate use of both isotropic and kinematic models has been observed. Such as, Yilbas et al. [52] modelled residual stress using ABAQUS FEM code of laser surface melting with aluminum composite. He considered the work-piece as an elastic body and used isotropic hardening to model rate independent plasticity with temperature dependent yield strength. In another work of laser cladding by Paul et al. [75] ABAQUS FEA software was used to model residual stress in H13 tool steel clad and substrate. A kinematic plasticity model with von Mises yield criterion was used to calculate plastic strain in this model. Although the prediction values gave rise to maximum 25% error with experimental data, but the trend in stress distribution was in agreement. Li et al. also followed kinematic hardening rule in predicting stress distribution of laser surface melting of 42CrMo4 steel in SYSWELD commercial FEA code [55]. From Table 2.5, it is observed that, mostly laser melting processes including laser welding, laser melting, LENS, laser cladding processes chose isotropic plasticity models for predicting thermo-

elastic-plastic residual stress. Both isotropic and kinematic plasticity models will be further discussed in chapter 4.

## 2.5 Summary

A detailed literature review on recent numerical modelling works of laser surface melting processes has been conducted and presented in this chapter. A significant number of modelling works in laser welding and laser cladding has been observed followed by selective laser melting, additive manufacturing and laser surface melting. Thermal models of those processes generally predicted temperature distribution, dimension of fusion, heat-affected zones and utilised to optimise the process parameters including laser power and scanning speed. There are also several thermomechanical models of different laser melting processes predicting residual stress in the laser modified surface. From the literature review it is evident that, a single 2D numerical thermal model of LSG for metallic materials has been found which is insufficient to grasp the process mechanism and collect the important criteria for developing FEM model of LSG for metals and alloys. Nevertheless, the information collected from the developed FEM models of other laser melting processes can be set as a guideline for developing LSG model. The lack of works in LSG modelling also requires the initiative of developing a reliable and simple numerical model of LSG from the scratch. Therefore, in this current study, a numerical thermal model of LSG using FEM will be developed which can quantitatively predict temperature distributions, heating cooling rates and depth of modified zone for different range of laser parameters and metallic materials. The thermal model will be extended to thermomechanical model to predict thermally induced residual stress in the surface and sub-surface region and crack formation tendency in LSG process. This model can be used for optimising laser parameters such as laser power and residence time for different materials.

# Chapter 3

## Thermal modelling of LSG

### 3.1 Introduction

This chapter presents the development of FEM thermal model for laser surface glazing of metallic materials. From literature review no FEM model of laser surface glazing for metallic material was found. Therefore, this model will be the first attempt in FEM thermal model development of laser surface glazing for metals using commercial finite element solver. For ensuring availability of material data and establishing the acceptability of this model development, the geometry, materials and laser parameters have been taken from previous experimental works of laser surface glazing for metals and alloys. First, a 2D model has been developed with a circular cross-section of a cylindrical geometry assuming the laser is irradiated on the lateral curvilinear surface of the cylinder. Then the model has been extended to 3D model with cylindrical geometry to explore three-dimensional temperature distribution. The models can predict temperature distributions, rates of heating and cooling and dimension of laser modified zone. Finally, the predicted temperature distribution from the FEM thermal model has been compared with the temperature calculated using an analytical solution of transient heat transfer process for a semi-infinite solid model with identical laser parameters used in the FEM model.

### 3.2 Methodology

The common numerical approaches to solve heat transfer model found in the literature followed finite element method and finite difference method. In a previous work, heat transfer modelling of LSG of porous thermal barrier coating has been solved using finite

difference method [27]. In finite difference method the derivatives of dependent variables are approximated over a computational domain mainly using Taylor series expansion. FDM predicts value of the dependent variables for the discretised points only. The limitation of this method is that it cannot find derivative for any discontinuous function. Moreover, it needs to transform any irregular physical domain to a regular computational space using chain rule to solve the differential sets of equations. On the other hand, FEM divides the complex or irregular physical domain into small finite regions and the dependent variable is solved for those regions through a set of polynomial algebraic equations called interpolation functions, shown in Equation 3.1. The finite regions are called elements and it can be of various shapes (linear, quadratic) in both 2D and 3D dimensions. The predicted value of the dependent variable is calculated for the nodes of the elements and interpolated over the elements. FEM can handle very complex geometry in wide range of engineering problems. Nodal loading such as point heat source as well as element load including surface or volumetric loads, pressure etc. can be easily applied for FEM. However, the main drawback of this process is to invert large coefficient matrix which costs a huge computational space and time.

In the present work, the methodology to develop thermal model of LSG has used FEM. A flow chart has been presented in Figure 3.1 to show the necessary steps followed in developing the thermal model of LSG using FEM. All the steps have been explained in the following subsections.

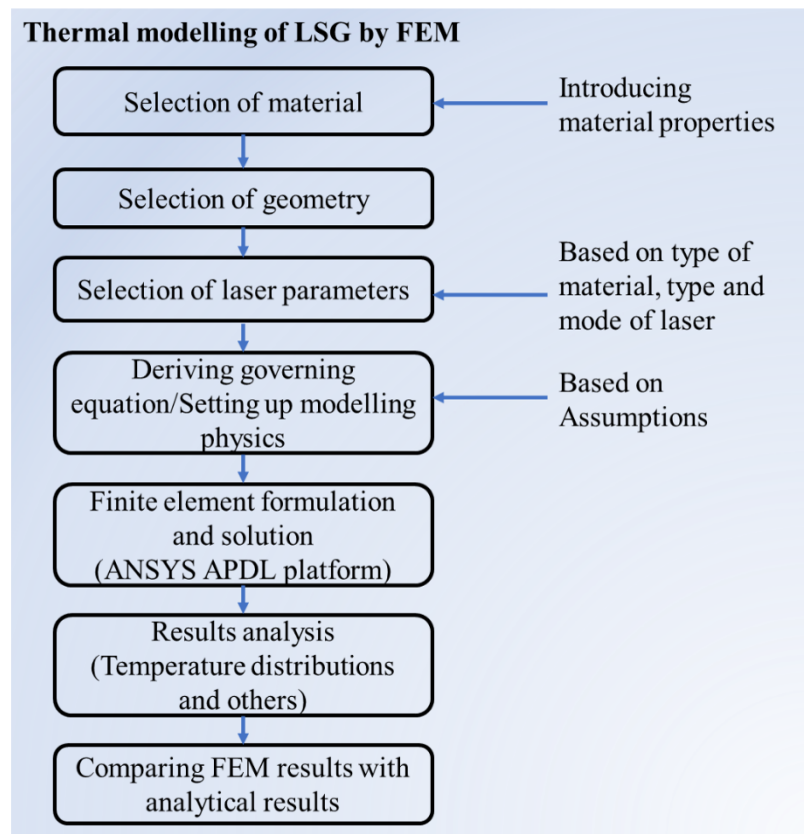


Figure 3. 1 Methodology of developing thermal model of LSG using FEM

### 3.2.1 Materials

The initial development of the FEM thermal model has been done with H13 tool steel taken from a previous experimental work of laser surface glazing [3]. H13 tool steel is predominantly used in the application of tooling industry especially for casting moulds for metals (Cu, Al alloys), forging tools and extrusion dies. However, the surface of the H13 tool steel mould is prone to abrasion and fatigue fracture for experiencing repetitive thermal and mechanical effects caused by high velocity molten metals during casting [10,76]. Therefore, improving surface properties by laser surface glazing of H13 tool steel mould is of significant importance to extend mould's service life [28,76]. The composition of H13 tool steel utilised for modelling work has been presented in Table 3.1.

Table 3. 1 Chemical composition of H13 tool steel in %weight [4]

Element	C	Si	Mn	Cr	Mo	V	Ni	Cu	P	S	Fe
%weight	0.45	1.20	0.50	5.50	1.75	1.20	0.30	0.25	0.03	0.03	Balance

### 3.2.2 Model geometry

The FEM model of laser surface glazing has been developed utilising a cylindrical geometry. The dimension of the cylinder has been taken from the previous experimental work of laser surface glazing [3]. It has 10 mm diameter and 100 mm length. For 2D FEM model circular cross-section of the cylinder has been considered and half-cylinder up to 1 mm length has been taken for 3D model. Although in laser surface glazing the laser is scanned over the surface with a certain scanning speed, but for the simplification in developing the model, laser beam is considered fixed at certain point over the surface of the cylinder. The schematic diagram of the cylindrical geometry with laser spot incident over the surface has been presented in Figure 3.2.

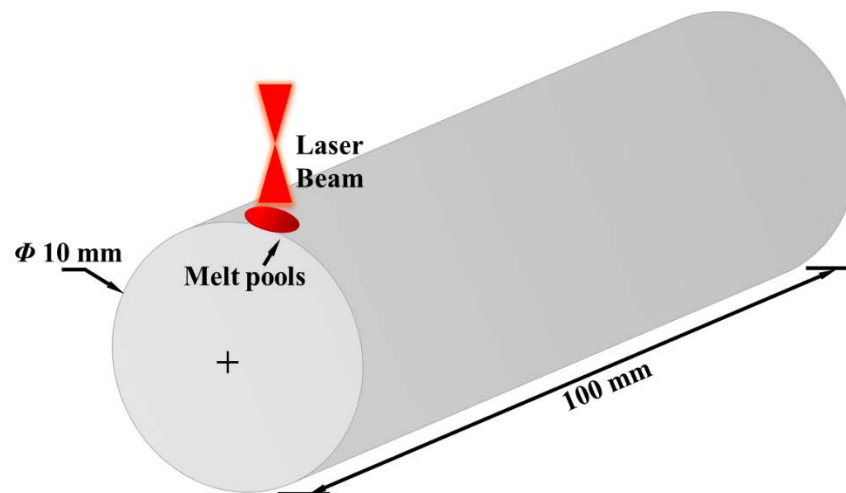


Figure 3. 2 Schematic illustration of cylindrical geometry used in modelling of laser surface glazing with laser beam fixed at one point over the surface

### 3.2.3 Laser parameters

The important process parameters utilised in developing the FEM model of laser surface glazing are laser power, beam width, laser scanning speed. The value of those parameters varies depending on type of laser, wavelength, mode of laser- whether continuous wave or pulse, and type of materials. Initially, the type of laser, wavelength, and beam width have been taken from the experimental work mentioned here [3]. However, the laser mode has been decided as continuous mode and the average laser power has been varied from 100-300 W. As fixed laser beam has been considered, a parameter called residence time has been taken into account instead of scanning velocity. Residence time is defined as the total material-beam interaction time and calculated by dividing laser beam width with scanning speed for continuous wave mode. The value of residence time has been set to 0.15 ms, considering the value used in the experimental work [3] and from typical power density-exposure time relation for laser surface glazing [78]. Table 3.2 presents the laser parameters utilised in developing thermal model of laser surface glazing for H13 tool steel.

Table 3. 2 Laser parameters used in the model

<b>Parameters</b>	<b>Specifications</b>
Laser type	CO <sub>2</sub> laser
Laser mode	TEM <sub>00</sub> continuous wave (CW)
Wavelength	10.6 μm
Power	100-300 W
Beam width	0.2 mm
Residence time	0.15 ms

### 3.2.4 Thermal modelling principle

#### *Governing equation*

The principle of transient thermal phenomena of laser surface melting processes follows the 1<sup>st</sup> law of thermodynamics and Fourier's conduction law where energy is conserved. In the present thermal model of LSG the following assumptions have been considered.

- The laser heat source has been considered fixed at one point of the surface.
- The laser type has been chosen as CO<sub>2</sub> laser of 10.6 μm wavelength and in continuous wave operating mode.
- The heat flux given by laser heat source is assumed constant.
- No internal heat generation within the treated part is considered.
- The convection and radiation loss at the surface exposed to the laser heat source are ignored due to the short interaction time.

A schematic diagram in Figure 3.3 shows the energy transfer in single step thermal model of LSG with stationary laser heat source. When the laser irradiates the surface, the part of the laser light is absorbed by the material surface and transformed to heat energy. The absorbed heat energy  $Q_{laser}$  is the heat generation rate coming from the laser heat source. Additionally, heat flow due to conduction from the heated surface to the bulk is also occurred along both X and Y direction, represented by heat flux rate  $q_x$  and  $q_y$ . From Fourier's conduction law,  $q_x = -k \frac{\partial T}{\partial x}$  and  $q_y = -k \frac{\partial T}{\partial y}$ , where k is thermal conductivity for isotropic material.

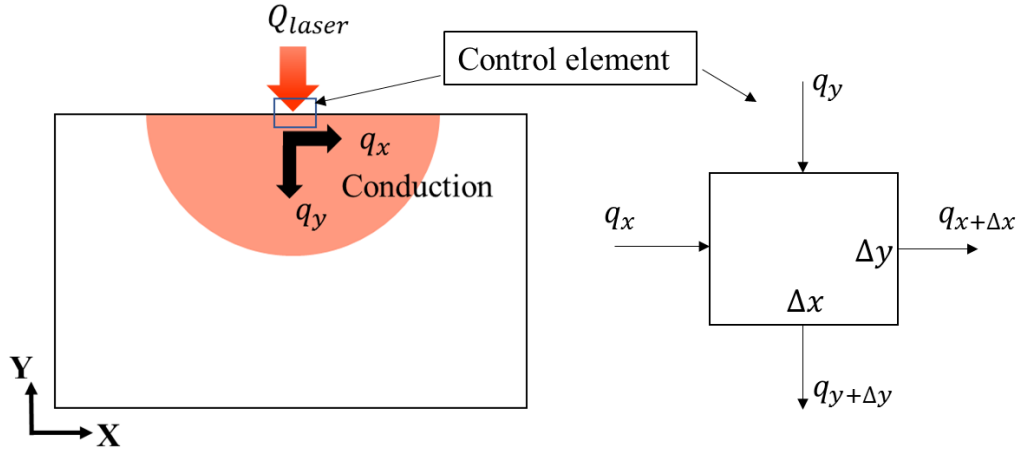


Figure 3. 3 Schematic representation of energy flow during LSG process and the conduction heat flow along x and y directions of a control element taken from the surface exposed to laser heat source

Consider an element near the surface exposed to the laser beam shown in Figure 3.3. Applying the principle of conservation energy to the element for conduction heat flow gives

$$q_x - q_{x+\Delta x} + q_y - q_{y+\Delta y} = \rho C_p \frac{\partial T}{\partial t} \Delta x \Delta y \quad (3.2)$$

Now, using Taylor series expansion, mathematically the  $q_{x+\Delta x}$  can be written as,

$$q_{x+\Delta x} = q_x + \frac{\partial q_x}{\partial x} \Delta x + \frac{1}{2!} \frac{\partial^2 q_x}{\partial x^2} \Delta x^2 + \frac{1}{3!} \frac{\partial^3 q_x}{\partial x^3} \Delta x^3 + \dots$$

As  $\Delta x$  is small enough that the variation of heat flow rate between  $x$  and  $x + \Delta x$  can be considered linear.

$$\text{Therefore, } q_{x+\Delta x} = q_x + \frac{\partial q_x}{\partial x} \Delta x$$

or  $q_x - q_{x+\Delta x} = -\frac{\partial q_x}{\partial x} \Delta x = -\frac{\partial}{\partial x} \left( -k \frac{\partial T}{\partial x} \right) \Delta x = \frac{\partial}{\partial x} \left( k \frac{\partial T}{\partial x} \right) \Delta x \Delta y$ , since  $q_x$  is the heat flux across the plane  $\Delta y \Delta z$  where,  $\Delta z = 1$  is considered for 2D element.

Similarly,  $q_y - q_{y+\Delta y} = \frac{\partial}{\partial y} \left( k \frac{\partial T}{\partial y} \right) \Delta x \Delta y$

Therefore, Equation 3.2 can be expressed as-

$$\frac{\partial}{\partial x} \left( k \frac{\partial T}{\partial x} \right) + \frac{\partial}{\partial y} \left( k \frac{\partial T}{\partial y} \right) = \rho C_p \frac{\partial T}{\partial t} \quad (3.3)$$

For the surface element the heat generation term  $Q_{laser}$  will be added in the Equation 3.4 and the general governing equation describing thermal phenomena of LSG will take the form as follows.

$$Q_{laser} + \frac{\partial}{\partial x} \left( k \frac{\partial T}{\partial x} \right) + \frac{\partial}{\partial y} \left( k \frac{\partial T}{\partial y} \right) = \rho C_p \frac{\partial T}{\partial t} \quad (3.4)$$

#### *Initial and boundary conditions*

The heat transfer phenomena of LSG is a transient process, high thermal gradient is present at the place exposed to the laser beam. Therefore, initial condition applies in this thermal model. The initial condition is considered here  $T(x,y,0) = T_0$ , where  $T(x,y,0)$  is the temperature at any point of the control element at time zero, i.e. before the process starts. The initial temperature is considered the ambient temperature which is 25°C. In the model, it is taken as the uniform reference temperature in SI unit, i.e. 298 K.

Figure 3.4 shows a schematic representation of the boundary conditions considered for the LSG process for stationary laser beam with constant heat flux.

1. At the surface where laser beam is incident,  $y = h$ ,  $l - r_{beam} < x < l + r_{beam}$

$$-k(T)\nabla T = Q_{laser} - h(T)\Delta T - \varepsilon\sigma\Delta T^4, \quad (3.5)$$

In this surface the laser heat flux  $Q_{laser}$  is entering in the surface whereas the conduction heat flow occurs from the surface to inside the bulk. Convection and radiation heat flow

also happen from the heated surface to the environment. Therefore, the Equation 3.5 shows all those energy balance on this surface [19,25].

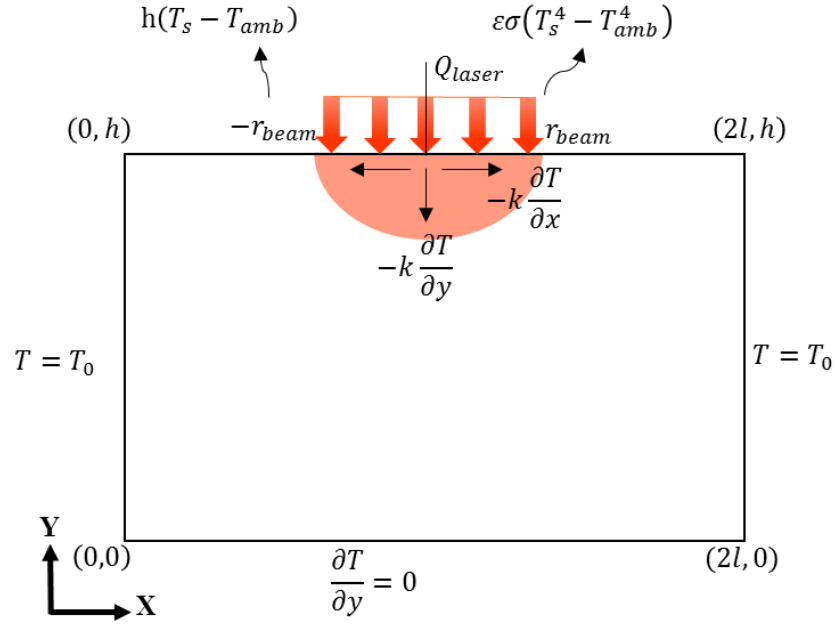


Figure 3. 4 Schematic representation of boundary conditions are applied in LSG process

In equation 3.5,  $Q_{laser}$  is the heat flux rate coming into the surface from laser heat source and  $\Delta T$  is the temperature difference. The film coefficient,  $h$ , is for the convection heat transfer on the surface due to the ambient air present or flowing of noble gases due to avoid oxidation at high temperature. For radiation heat transfer,  $\varepsilon$  and  $\sigma$  are the material emissivity and Boltzmann's constant ( $5.67 \times 10^{-8} \text{ Wm}^{-2}\text{K}^{-4}$ ) for thermal radiation. Because of the very short residence time and small beam diameter caused rapid localised heating and cooling in LSG, the convection and radiation boundary conditions are ignored, thus the boundary condition becomes as Equation 3.6 [31,51].

$$-k(T) \cdot \nabla T = Q_{laser} \quad (3.6)$$

2. The two side surfaces in Figure 3.4 the boundary condition is  $T = T_0$ , considering semi-infinite model.  $T_0$  is the room temperature of the bulk.

3. The bottom surface at  $y = 0$  is considered adiabatic where  $\frac{\partial T}{\partial y} = 0$ .

The laser beam is considered as a TEM<sub>00</sub> continuous wave laser heat source. The beam width is very small 0.2 mm in for LSG compare to other laser surface hardening process.

Hence, the constant heat flux rate or laser intensity has been considered in this thermal model expressed in Equation 3.6 [31,79].

$$Q_{laser} = \frac{AP}{\pi r_{beam}^2} \quad (3.6)$$

where,  $Q_{laser}$  is laser intensity,  $P$  is laser power,  $A$  is the laser absorptivity corresponding to the material and laser wavelength,  $r_{beam}$  is radius of the spherical beam. The summary of governing equations, initial and boundary conditions based on the assumption for the 2D and 3D thermal model of LSG has been presented in Table 3.3

Table 3. 3 Governing equations, initial and boundary conditions of thermal 2D and 3D LSG modelling

Conditions	2D model	3D model
Governing equation	$\rho C_P \frac{\partial T}{\partial t} = \frac{\partial}{\partial x} \left( k \frac{\partial T}{\partial x} \right) + \frac{\partial}{\partial y} \left( k \frac{\partial T}{\partial y} \right)$	$\rho C_P \frac{\partial T}{\partial t} = \frac{\partial}{\partial x} \left( k \frac{\partial T}{\partial x} \right) + \frac{\partial}{\partial y} \left( k \frac{\partial T}{\partial y} \right) + \frac{\partial}{\partial z} \left( k \frac{\partial T}{\partial z} \right)$
Boundary conditions	$-k \frac{\partial T}{\partial y} = Q_{laser}$ , laser irradiated surface $\frac{\partial T}{\partial \vec{n}} = 0$ , any other surface	$-k \left( \frac{\partial T}{\partial x} + \frac{\partial T}{\partial y} + \frac{\partial T}{\partial z} \right) = Q_{laser}$ , laser irradiated surface $\frac{\partial T}{\partial \vec{n}} = 0$ , any other surface
Heat source intensity	Constant, $Q_{laser} = \frac{AP}{\pi r_{beam}^2}$	
Initial condition	Uniform temperature, when $t=0$ , $T_{unif} = 298 K$	

### *Limitation of the present thermal model of LSG*

This thermal models of LSG is based on the classical physics, where the purpose is to investigate thermal distribution within several micrometre (within 100-200  $\mu\text{m}$ ) range caused by generally conduction heat transfer due to the irradiating high intensity laser beam on the surface. The melt thermodynamics in heat transfer process due to the LSG is out of scope of this model at present. Moreover, moving boundary condition due to the sample movement during the process has not accounted in this present work.

## **3.3 FEM model set-up**

### 3.3.1 FEM solver, ANSYS

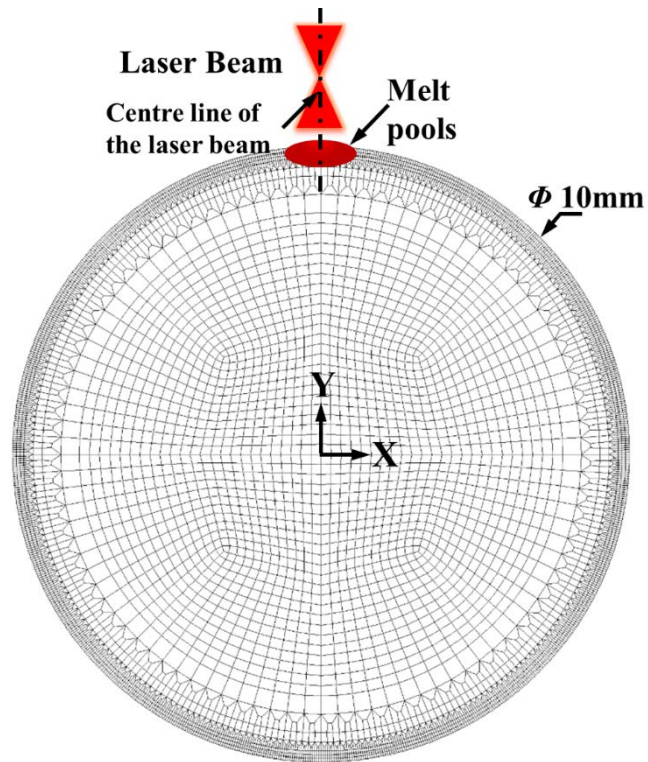
ANSYS mechanical APDL software has been used for finite element formulation (meshing) of the governing equation for thermal model of LSG. The numerical solution has been calculated using the Newton-Raphson iteration technique by the software. ANSYS is a well-known software utilised in numerous FEM modelling of laser processes [19,25,40,80]. The mechanical APDL (ANSYS parametric design language) is chosen for this process for some reasons in particular, the entire model is considered as a solid continuum system, the user can have good control and flexibility in meshing operation and, also application of tabular or functional boundary condition is easier here using the APDL script.

### 3.3.2 2D and 3D models

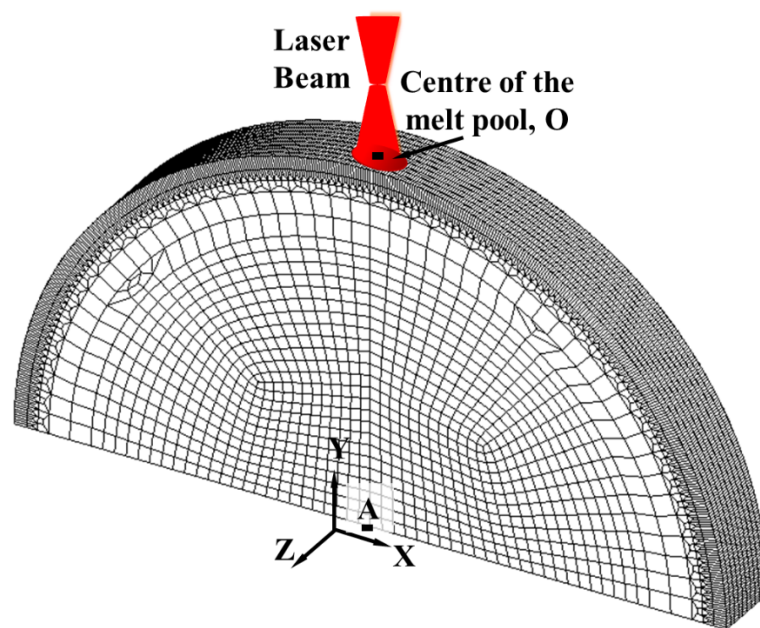
The circular cross-section of the cylinder having 10 mm diameter has been selected for the geometry of the 2D model. To mesh the model, a thermal 2D element Plane 55 has been chosen. Plane 55 element has 4 nodes and single degree of freedom (DOF) which is temperature, hence it is mathematically economical. This element is capable of modelling both 2D steady-state and transient heat transfer analyses, also it can be coupled with mass transfer flow with constant velocity field. Moreover, Plane 55 was used in several 2D

FEM thermal modelling [81–83], which manifests its wide range of reliability and acceptance. The quadrilateral form of Plane 55 element has been taken for mapped meshing of the model geometry. On the other hand, for 3D model, a half-cylindrical geometry has been taken into consideration for reducing simulation time and computational space. The half-cylinder has 10 mm diameter and 1 mm length. The length has been reduced from 100 mm to 1 mm to minimise the simulation time and computational space. The 1 mm length of the cylinder is reasonable to provide enough heat sink because, the workpiece has been assumed as semi-infinite model. This length can also be justified with analysing scale length of thermal diffusion mentioned in A. Issa et al. [84]. The scale length of diffusion  $L_D = \sqrt{\alpha t_R}$ , where  $t_R$  is the residence time of laser heat source and  $\alpha$  is the thermal diffusivity of the material. This gives the idea of the maximum length of heat propagation throughout the part. In this case, the scale length for H13 tool steel is 0.0359 mm calculated using the above formula, where the thermal diffusivity of H13 tool steel is  $8.6 \times 10^{-6} \text{ m}^2\text{s}^{-1}$ . As the scale length is very small due to the short residence time (0.15 ms), this length is sufficient to provide heat sink along the axial direction (z-axis) of the cylindrical surface for the fixed laser beam. Solid 70 thermal brick element type has been selected for meshing the 3D thermal model. It is a 3D brick element with 8 nodes and single DOF which is temperature. This element type is also mathematically reasonable and has been widely used in other thermal modelling of laser melting processes [19,40,43,51]. Choosing appropriate element type is important to ensure accuracy in numerical analysis. Generally, the element type is selected based on 1. Dimension of the model, 2. Analysis type, 3. Shape and 4. The special properties of the element type. Figure 3.5 illustrates the meshed 2D and 3D geometries used in developing thermal model of LSG for the cylindrical specimen using ANSYS APDL. As fixed or stationary laser beam irradiates on the surface, therefore, to capture the effects of the irradiation accurately, the element length in the region of circumference has been kept

smaller than the interior elements of the circle shown in Figure 3.5. This has been done following transitional meshing technique, where a ratio has been maintained during the transition from fine elements to coarse elements. Based on the ratio, it is possible to increase the number of elements near the region of interest of surface exposed to laser beam and reduce the number of elements in the inner unaffected region. Transitional mapped meshing technique helps to reduce total number of elements resulting into saving simulation time. The optimum element length has been chosen by conducting mesh convergence operation. For detail information of mesh convergence operation, please see appendix section A2.1. By employing optimum element length total number of elements of 2D and 3D models have been counted 6673 and 47060 respectively.



(a)



(b)

Figure 3. 5 The meshed geometries of (a) 2D circular and (b) 3D half-cylinder geometries with stationary laser beam on top of the surface; point O is the middle of the melt pool is created due to laser irradiation

A uniform heat flux has been applied as a boundary condition. Time step size for the transient thermal process has been selected as  $1 \times 10^{-6}$  s for 0.15 ms residence time. An iterative time-step scheme has been carried out explicitly for ensuring convergence and accuracy of results and then the above time-step size has been selected. The thermo-physical properties required for the thermal model for H13 tool steel are presented in Table 3.4. The properties are kept constant above temperature 2000 K assuming very few changes in properties at molten state. Solid to liquid phase change has not been accounted at this stage. A constant absorptivity of H13 tool steel having value of 0.3 [3] has been applied for CO<sub>2</sub> laser.

Table 3. 4 Thermo-physical properties of H13 tool steel as a function of temperature  
[41,85]

Temperature, K	298	373	673	873	1073	1273	1473	1673	1873
Density, kgm <sup>-3</sup>	7650	7650	7580	7550	7200	7150	7100	7000	7000
Thermal Conductivity, Wm <sup>-1</sup> K <sup>-1</sup>	29.5	30.3	37	40.5	43.9	47.3	50.7	21.98	24.06
Specific heat, Jkg <sup>-1</sup> K <sup>-1</sup>	447	453	502	537	573	606	642	677	708

### 3.4 Temperature distribution calculation using an explicit solution

The temperature distribution at cooling phase has been also calculated using an explicit solution from an analytical modelling of heat conduction phenomena with source term for a semi-infinite geometry from [86], which is expressed in Equation 3.7.

$$T(y, t) = T_0 + \frac{2Q_{laser} \left(\frac{\alpha t}{\pi}\right)^{1/2}}{k} \exp\left(\frac{-y^2}{4\alpha t}\right) - \frac{Q_{laser} y}{k} \operatorname{erfc}\left(\frac{y}{2\sqrt{\alpha t}}\right), \quad (3.7)$$

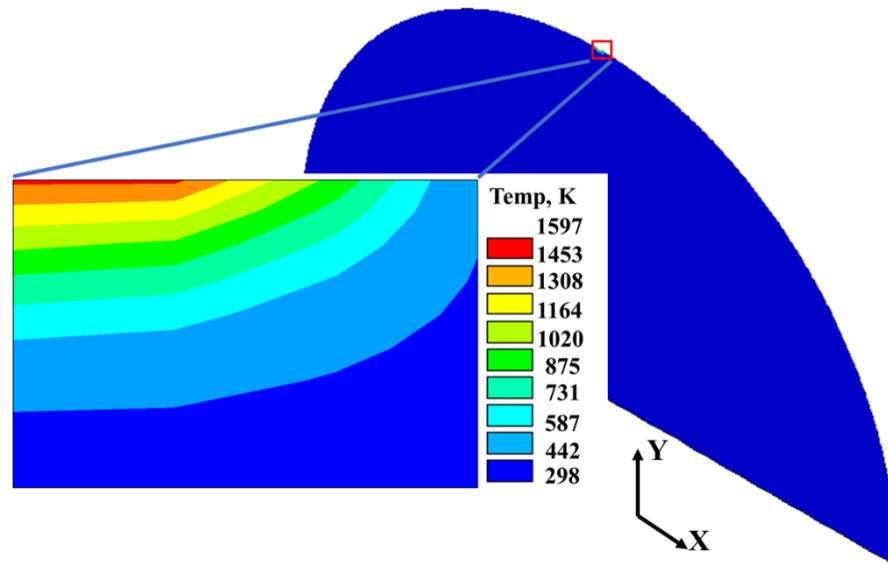
where,  $T_0$  is the initial temperature,  $\alpha$ , the thermal diffusivity is the ratio of  $k$  thermal conductivity and the product of the density  $\rho$  and specific heat  $C_P$ . The temperature has been calculated putting the same parameters used in FEM model to verify the temperature obtained from the FEM model. The time temperature graph using Equation 3.6 for laser glazing parameters has been plotted in MATLAB software. The  $erfc()$ , is called complimentary error function defined as  $1 - erf()$ , where  $erf()$  is twice of the Gaussian distribution with zero (0) mean and variance of 1/2. MATLAB can calculate  $erfc()$  by default using the syntax as  $y = erfc(x)$ . Temperature distribution has been calculated for 200 W laser power with 0.15 ms residence time and 0.2 mm beam width. Constant thermal properties with constant heat flux were used in these calculations, while temperature dependent properties were accounted in numerical cases.

### 3.5 Results and discussion

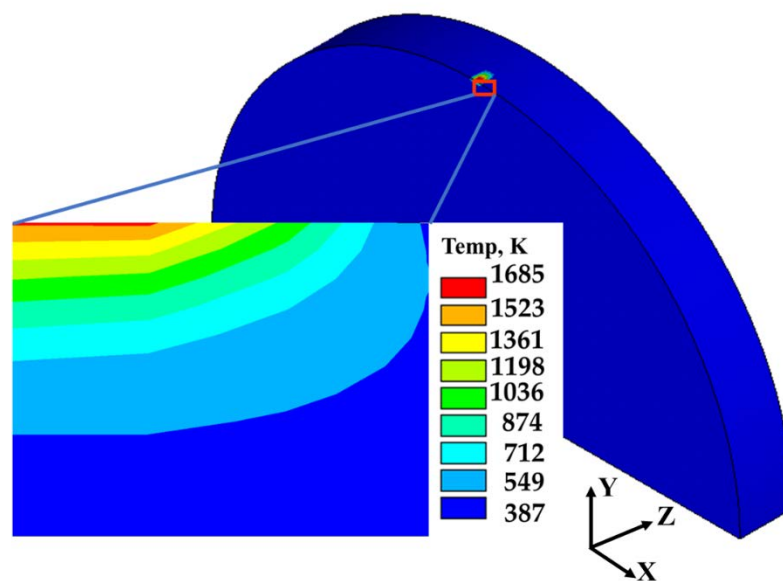
#### 3.5.1 2D and 3D FEM models

##### *Temperature Isotherms*

The FEM thermal model gives temperature distributions at the place where laser was applied on the surface. Figure 3.6a and 3.6b show the temperature distribution on X-Y plane from 2D and 3D thermal model respectively at 200 W laser power at 0.15 ms time. Temperature isotherms of the 2D model shows peak surface temperature 1597 K. For 3D model, the peak surface temperature is 1685 K. 2D model gives the temperature distribution in X and Y directions only, whereas 3D model gives for all three dimensions. The laser heat source for 3D model has been assumed as area heat source which inputs heat flux over an area equivalent to the beam area. On the contrary in 2D model the heat flux is input over the line of equivalent to beam diameter. The total heat input in 3D model is higher than the 2D model. This causes higher peak surface temperature in 3D model



(a) 2D model



(b) 3D model

Figure 3. 6 Temperature distributions on X-Y plane through the depth from (a) 2D and (b) 3D thermal models of H13 tool steel at 200 W laser power at 0.15 ms time

than 2D. To improve accuracy 3D model is better than 2D, however, 3D FEM model costs higher computational time and space.

#### *Heating and cooling rates*

Time-temperature plot from 2D and 3D thermal models at laser power 200 W with residence time 0.15 ms and 0.2 mm beam width has been plotted in Figure 3.7. The peak surface temperature attained in 2D model is 1597 K. For 3D model, peak surface temperature has been obtained 1685 K. It is noted that, the difference in peak surface temperature for both 2D and 3D model is not significant. The peak temperature achieved at 200 W power is slightly below the melting temperature (1727 K) for H13 tool steel. A previous experimental work of LSG for H13 tool steel reported that, at 249 W average power and between 0.12-0.25 ms residence time, melting of H13 tool steel has been achieved [3]. This statement is evident in the result found from the 3D model conducted at 300 W laser power. The peak surface temperature has been achieved 2554 K at 300 W, can be found in the author's published work [87]. However, surface temperature cannot reach to melting point of H13 tool steel below 200 W laser power. Therefore, laser surface glazing of H13 tool steel needs more than 200 W laser power for 0.15 ms residence time and 0.2 mm beam width. The parametric study to optimise the laser power has been presented in chapter 5.

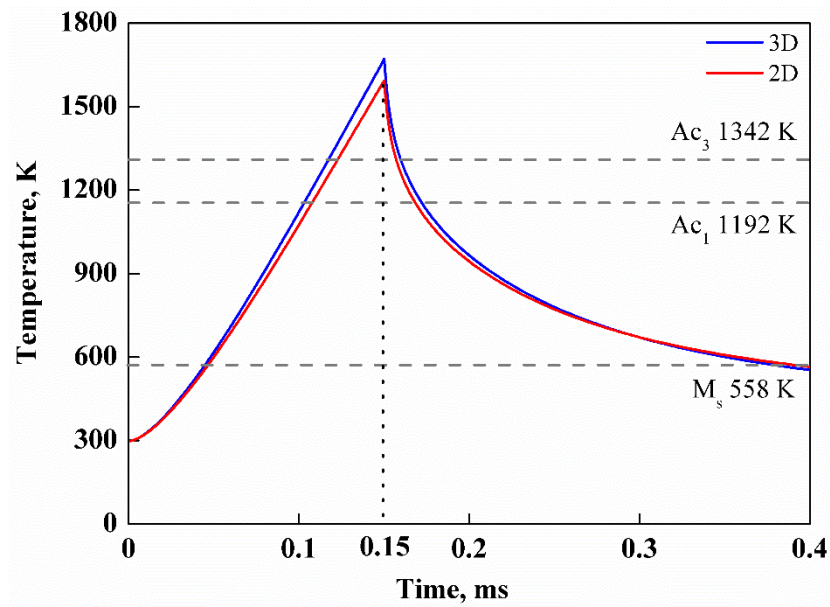


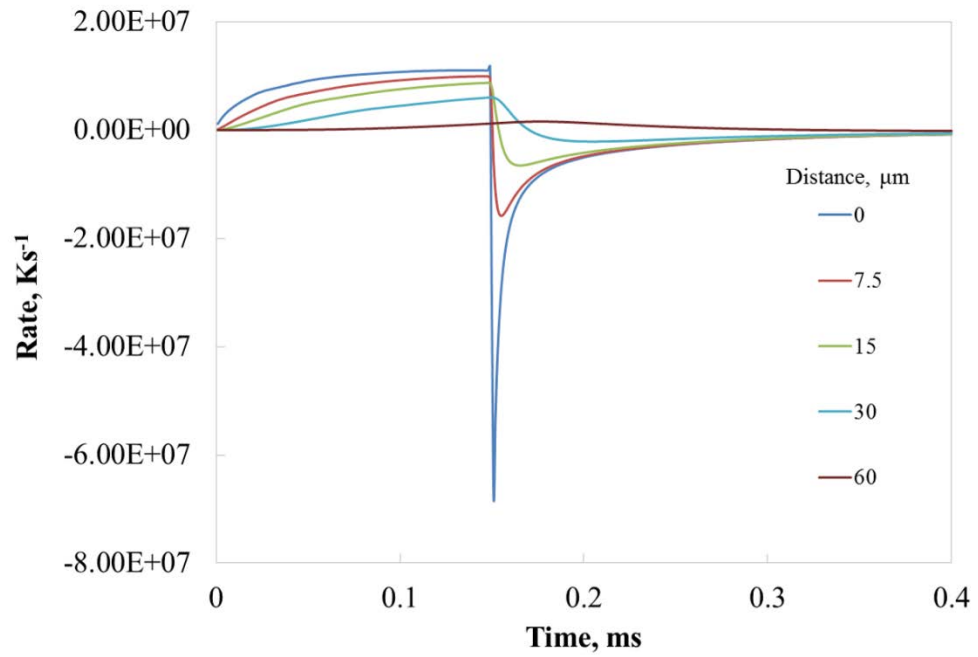
Figure 3. 7 Time-temperature plot from 2D and 3D FEM LSG models of H13 tool steel for 200 W laser power, 0.2 mm beam width and 0.15 ms residence time

It is observed that, the slope of heating curve is steeper than the cooling curve in Figure 3.7. The heating and cooling rates have been calculated from the slopes of this time-temperature plot. Table 3.5 presents the average and maximum calculated heating and cooling rates for 200 W laser power from 3D thermal model. The average heating and cooling rates are respectively  $9.44 \times 10^6 \text{ K s}^{-1}$  and  $3.03 \times 10^6 \text{ K s}^{-1}$ . The rates have been calculated for the temperature range from 298 K to 1685 K, from initial temperature to the maximum surface temperature achieved in 3D model. As 2D model has showed similar maximum temperature, the heating and cooling rates obtained from this model are almost equal to 3D model.

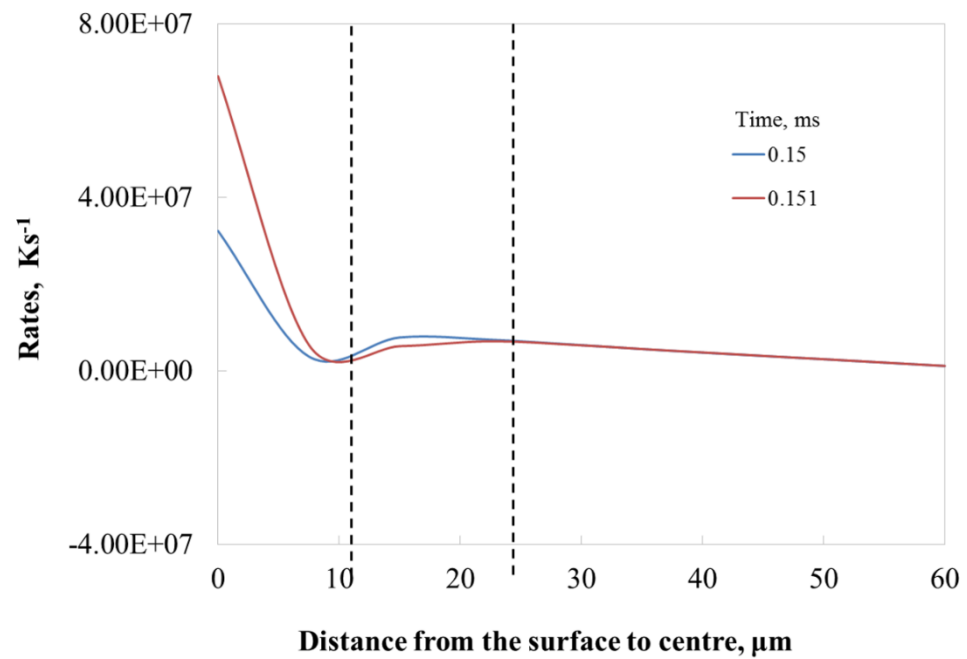
Table 3. 5 The rates of heating and cooling of H13 tool steel at 200 W laser power

$dT/dt, \text{ K s}^{-1}$	Average rate	Max. rate
Rate of heating	$9.44 \times 10^6$ (298-1685 K, 0.15 ms)	$3.50 \times 10^7$ (1685 K, 0.15 ms)
Rate of cooling	$3.03 \times 10^6$ (1685-465 K, 0.55 ms)	$7.27 \times 10^7$ (1603 K, 0.151 ms)

The maximum heating and cooling rates are  $3.50 \times 10^7 \text{ Ks}^{-1}$  and  $7.27 \times 10^7 \text{ Ks}^{-1}$  observed at respectively 0.15 ms and 0.151 ms at onset of cooling. From the 3D thermal model, the variation of both heating and cooling rates over the time have been plotted in Figure 3.8a at different depth from the surface towards the centre of the cylinder. It is observed that the cooling rates are higher than the heating rates. The surface has experienced highest cooling rates than the 7.5  $\mu\text{m}$  depth below the surface. Gradually, rates have reduced more when depth increases. It is noticed that the effect of heat energy has reached up to 60  $\mu\text{m}$  from the surface at 200 W laser power at 0.15 ms residence time and 0.2 mm beam width. Figure 3.8b has presented the cooling rates vs. distance from surface to centre up to 60  $\mu\text{m}$  for time 0.15 ms and 0.151ms. Highest cooling rates are found at 0.151 ms at onset of cooling. From this figure it is observed that change of cooling rates within around 10  $\mu\text{m}$  is significant. In total the variation of cooling rates has been observed up to 22  $\mu\text{m}$  approximately at 200 W laser power. This implied that the zone of 22  $\mu\text{m}$  depth from surface has been affected by laser heating and could be estimated as the depth of modified zone.



(a)



(b)

Figure 3. 8 (a) Cooling rates vs. time for different depths from surface to centre up to 60  $\mu m$  and (b) Cooling rates vs. distance from surface to centre for 0.15 ms and 0.151 ms

time

*Predicting microstructure in the modified zone*

From Figure 3.7, it is also possible to predict surface microstructure of the modified surface based on the critical transformation temperature and heating and cooling rates. The method of predicting microstructure in the modified surface has been also found in the literature [41].  $A_{c1}$ ,  $A_{c3}$  and  $M_s$  are the critical isothermal transformation temperature lines of H13 tool steel, shown in Figure 3.9.  $A_{c1}$  defines transformation from austenite to pearlite and  $A_{c3}$  refers to austenite to ferrite.  $M_s$  is the transformation line from austenite to martensite hard phase. Pearlite and ferrite are called soft phases compare to martensite, which has higher hardness. If the cooling rates is higher than the critical cooling rate of martensite formation, then austenite transforms to martensite rather than ferrite or pearlite. From Table 3.5 it is observed that cooling rate is extremely higher than the critical cooling rate of martensite transformation. Therefore, it is anticipated that there will be martensite in the zone having temperature just below the melting point. Martensite in surface and subsurface regions has been reported in previous experimental work of LSG for H13 tool steel. However, the molten surface due to LSG consists of significant number of micro and nano crystals of  $\delta$ -ferrite with small number of martensite depending on laser parameters [3]. The formation of  $\delta$ -ferrite is caused by extremely higher cooling rates in the molten region which avoid formation of austenite in the glazed region.

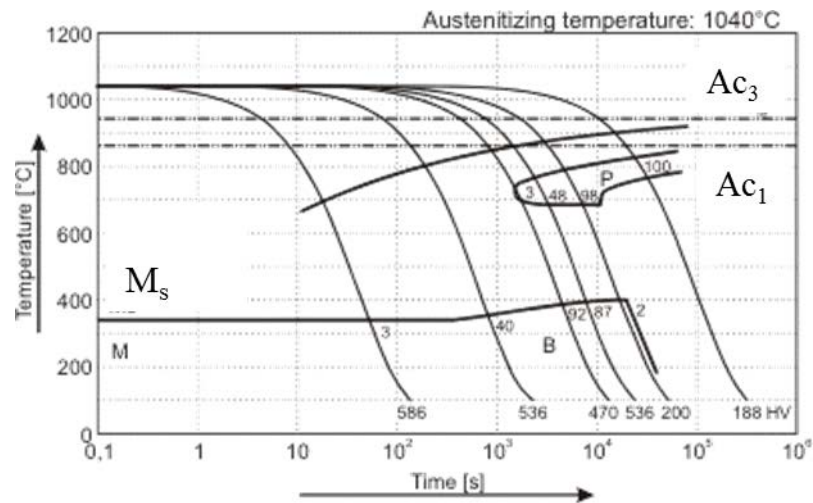
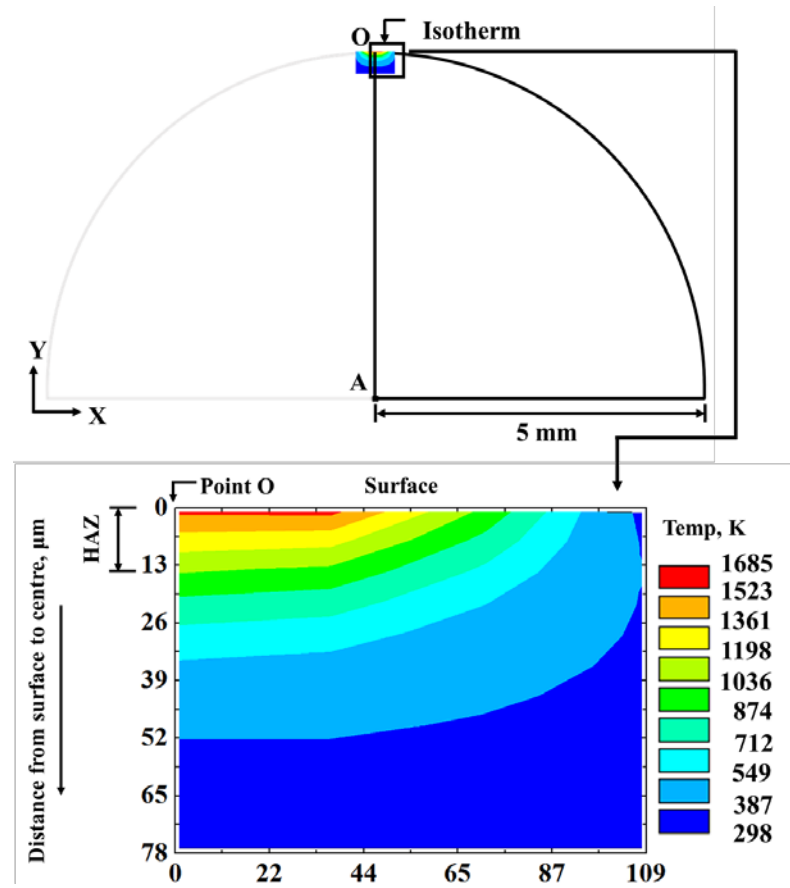


Figure 3. 9 TTT diagram of H13 tool steel [41]

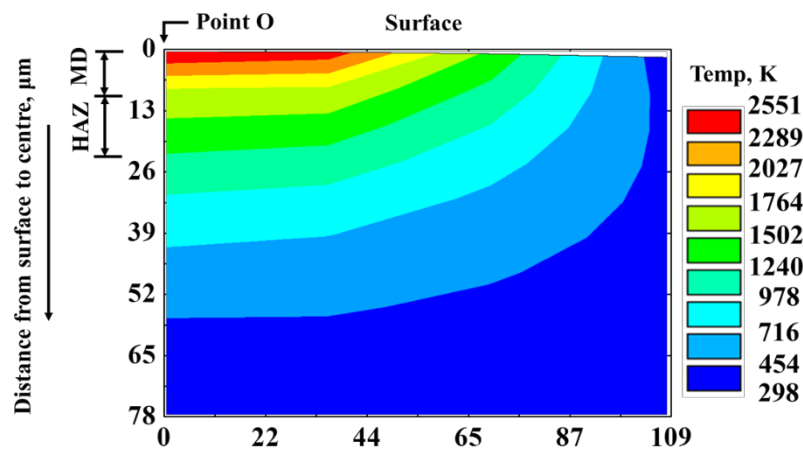
### *Depth of modified zone*

The temperature isotherm or distribution of the laser irradiated zone at 0.15 ms from 3D model has been illustrated in Figure 3.6b. From this temperature isotherm, the depth of modified zone has been calculated based on the temperature range. The depth of modified zone has not varied significantly for 2D and 3D models. A schematic diagram of the cross-section of half-cylinder with the isotherm has also been presented in the Figure 3.10a to locate the isotherm. The area of the isotherm selected is  $109 \mu\text{m} \times 78 \mu\text{m}$ , where all changes in temperature from the surface towards the centre have been captured. From the maximum surface temperature up to the critical phase transformation temperature  $Ac_1$  (1685-1192 K) has been taken as the range where possible phase transformation took place. The maximum surface temperature achieved with 200 W laser power is below the melting point (1727 K) of H13 tool steel and no melting has been occurred. Therefore, the heat-affected zone (HAZ) has been calculated approximately 13  $\mu\text{m}$  from the temperature isotherm at 200 W laser power. Heat-affected zone refers to the area where solid-state phase transformation occurred and temperature of this zone after heating remains between  $Ac_3$  and melting point (austenitic zone). From the temperature isotherm the depth of HAZ has been estimated approximately 13  $\mu\text{m}$  for 200 W laser power.

The temperature isotherm for 300 W laser power has also been illustrated in Figure 3.10b. In this case, melting occurs as the peak surface temperature is 2551 K, which is above the melting point. Therefore, the laser modified zone consists of both melt pool and HAZ. The estimated melt depth (MD) calculated between the 2551-1727 K is around 9  $\mu\text{m}$ , whereas the HAZ depth is 14  $\mu\text{m}$ . Thence, the total depth of modified zone is 23  $\mu\text{m}$ . However, in the previous experimental work of LSG for H13 tool steel reported that, at 305 W average power with 12-25 ms residence time the obtained depth of modified zone was between 48-80  $\mu\text{m}$  [3]. This experiment was performed with pulse CO<sub>2</sub> laser, where other laser parameters such as duty cycle, pulse rate frequency (PRF), pulse width, overlapping ratio were included. Moreover, Kear et al. [2] showed an analytical relationship between cooling rates and melt depth possible to achieve for LSG process. It is reported that for the process attaining average cooling rates of  $10^7 \text{ K s}^{-1}$  will have melt depth in  $10^{-4}$  mm range. 23  $\mu\text{m}$  depth of modified zone attained from this model at 300 W laser power and very high cooling rates is in agreement with this statement.



(a) 200 W



(b) 300 W

Figure 3. 10 Temperature isotherm for two laser power (a) 200 W and (b) 300 W, showing melt depth (MD) and heat-affected zone (HAZ). The schematic diagram of the cross-section of half cylinder is pointing out the location of the isotherm

### 3.5.2 Comparing results from FEM models and explicit solution

The temperature distribution along Y direction from an explicit solution from the analytical analysis of a semi-infinite heat conduction model and the 2D and 3D numerical models have been plotted in Figure 3.11. The horizontal axis of the graph has been defined as the distance from the surface up to the depth of 60  $\mu\text{m}$  towards the centre. The peak surface temperature from the explicit solution has found 1689 K. In numerical 2D and 3D models, peak surface temperatures have been obtained 1570 K and 1685 K respectively. The analytical solution has given slightly higher value than the numerical solutions, although 3D FEM model has calculated almost equal. The both percentage of increment of peak surface temperature from the explicit solution with 2D and 3D FEM model are respectively 7% and 0.2%. The increment in peak temperature from the explicit solution may be because of the constant thermal properties used in this calculation whereas numerical models have been conducted with temperature dependent properties. Nevertheless, the trend in temperature distribution are in good agreement for both numerical and explicit solution. A previous work of LSG for H13 tool steel calculated the depth of modified zone from the temperature isotherm obtained from explicit solution. In this work, the predicted depth of modified zone appeared twice than the measured depth from the experimental for same laser parameters [28].

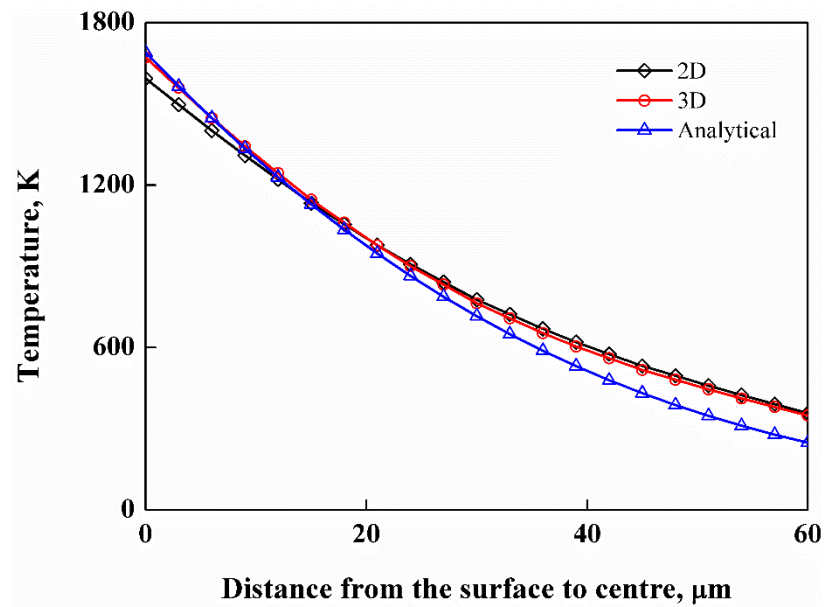


Figure 3. 11 Analytical and numerical temperature distributions along the distance from the surface towards the centre in the cooling phase

However, this explicit solution did not show variation in temperature beyond certain depth (around 60  $\mu\text{m}$ ) from the surface regardless laser power and residence time. Therefore, numerical thermal model is effective and reliable tool in predicting temperature distribution for LSG process for different laser parameters.

### 3.6 Summary

2D and 3D FEM transient thermal model of LSG have been successfully developed. The detail thermal modelling methodology and FEM set-up have been described. The model can predict temperature distribution, heating and cooling rates, depth of modified zone. Both 2D and 3D thermal models have shown equivalent results. Therefore, 2D model can be recommended for the simplification of the modelling process. However, 3D model will be more suitable for the future development of this process simulation when multiple variables such as moving heat source, overlapping will be included. Modelling results have shown that with increasing laser power, the peak temperature has been increased. Heating and cooling rates have been obtained  $9.44 \times 10^6$  and  $3.03 \times 10^6 \text{ Ks}^{-1}$  respectively

for 200 W laser power. Small melt depth has been achieved for 300 W, where at 200 W no melting has occurred. Therefore, conducting LSG for H13 tool steel needs above 200 W laser power, thus using this model the LSG process can be optimised for various materials and laser parameters.

-----X-----

## Chapter 4

# Thermomechanical modelling of LSG

### 4.1 Introduction

This chapter has been outlined the development of 2D thermomechanical modelling of LSG based on constitutive thermo-elasto-plastic theory to predict residual stress in the process. The variation in stress-strain developed on the laser irradiated zone with laser parameters has been demonstrated based on the author's published work [88].

#### 4.1.1 Residual stress in LSG

Laser surface glazing induces residual stress in the surface, sub-surface area of the treated part, due to the extremely fast cooling rates generated from the process. In absence of external load any remaining stress inside the component encountered heat or mechanical treatment is called residual stress. If the induced residual stress goes beyond the elastic limit of the material of the treated component, then it can be detrimental resulting into surface cracks and delamination from the bulk. This causes the reduced service life and incurs repair or reinstallation costs. Therefore, quantification of induced residual stress during the process and knowing the mechanism of residual stress development have paramount importance to get best output from LSG. The high heat flux of laser beam and short residence time are major cause behind the rapid cooling rate, which results into higher residual stress in the modified surface area. Developing residual stress in LSG is complex phenomena. Many factors such as temperature gradient effects, material constraints (stiffness, bonding) and phase transformation within fraction of seconds are also involved in generating stress [55,89]. The phase transformation effect on residual stress development is out of scope in this study. Therefore, the nature of residual stresses

has been explained by the temperature gradient mechanism explained in [51,90]. Figure 4.1 schematically has shown the stress-strain relationship based on the temperature gradient mechanism on the application of laser heat source.

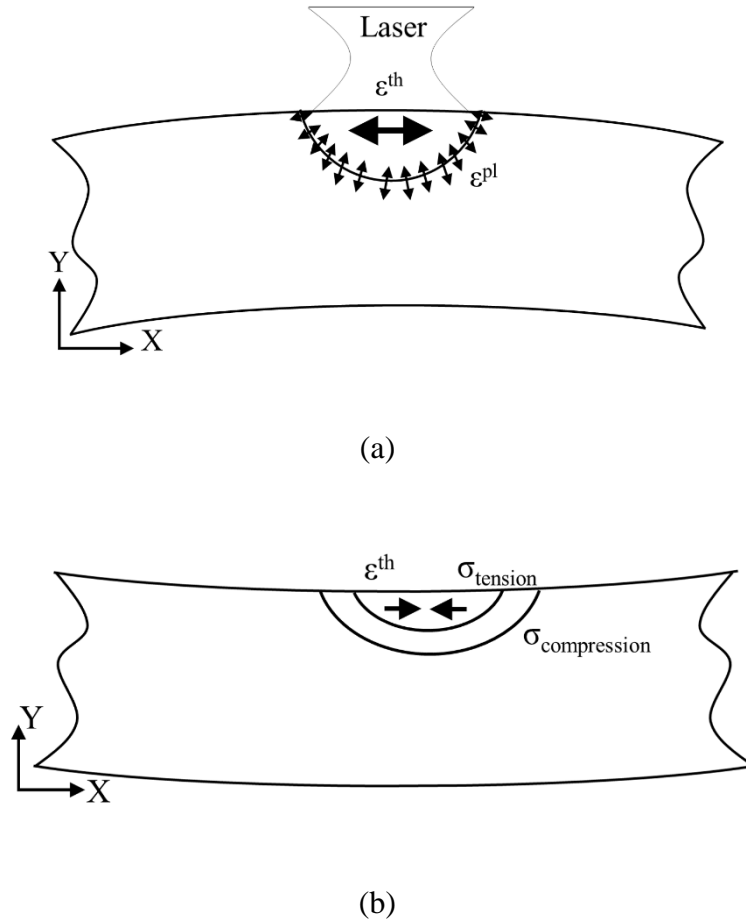


Figure 4. 1 Schematic demonstration of thermal stress development due to thermal strain in temperature gradient mechanism (a) during heating and (b) during cooling [51]

## 4.2 Methodology

### *Governing equation*

The principle of thermomechanical modelling of laser surface glazing is underpinned in the constitutive thermo-elasto-plastic theory of classical mechanics. Due to the temperature gradient and material constraint around the laser heated area the total strain developed in the system is expressed as Equation 4.1.

$$\varepsilon^{total} = \varepsilon^{th} + \varepsilon^{el} + \varepsilon^{pl} \quad (4.1)$$

The following assumptions have been taken into account for this modelling.

- Material treated by the laser is considered as linear elastic-plastic material, shown in Figure 4.2.

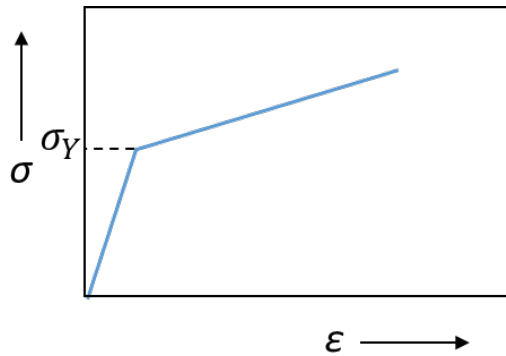


Figure 4. 2 Stress strain relationship in bilinear elastic-plastic material

- No phase transformation induced strain is present.

In Equation 4.1, the total strain,  $\varepsilon^{total}$  consists of thermal ( $\varepsilon^{th}$ ), elastic ( $\varepsilon^{el}$ ) and plastic ( $\varepsilon^{pl}$ ) strains. Thermal strain is calculated from the coefficient of thermal expansion/contraction and temperature gradient, using Equation 4.2 [91].

$$\{\varepsilon^{th}\} = \{\alpha\}\Delta T, \quad (4.2)$$

where,  $\{\alpha\}$  is the coefficient of thermal expansion,  $\Delta T$  is the temperature difference. the elastic strain,  $\{\varepsilon^{el}\}$  is calculated from the total strain,  $\{\varepsilon^{total}\}$  by deducting thermal strain,  $\{\varepsilon^{th}\}$  and plastic strain,  $\{\varepsilon^{pl}\}$  by Equation 4.3.

$$\{\varepsilon^{el}\} = \{\varepsilon^{total}\} - \{\varepsilon^{th}\} - \{\varepsilon^{pl}\}, \quad (4.3)$$

The stress is calculated using Equation 3.4,

$$\{\sigma\} = [D]\{\varepsilon^{el}\} \quad (4.4)$$

In the above Equation 4.4, The stress follows the linear relationship of stress-strain (Hooke's law) and is calculated with the elastic strain and  $[D]$ , the material stiffness matrix.  $\{\sigma\}$  is the stress tensor coming from material constraints and other boundary conditions such as holding chuck. The plastic strain is calculated using bilinear rate-independent von Mises plasticity [55]. Von Mises plasticity follows basically three general flow rules [51] of elastic-plastic material including, isotropic, kinematic and mixed plasticity, as mentioned in section 1.4. In this study, both isotropic and kinematic plasticity rules have been applied separately for determining plastic strain and compare the effects on residual stress. The schematic diagrams of yield surface evolution during both isotropic and kinematic plasticity have been presented in Figure 4.3.

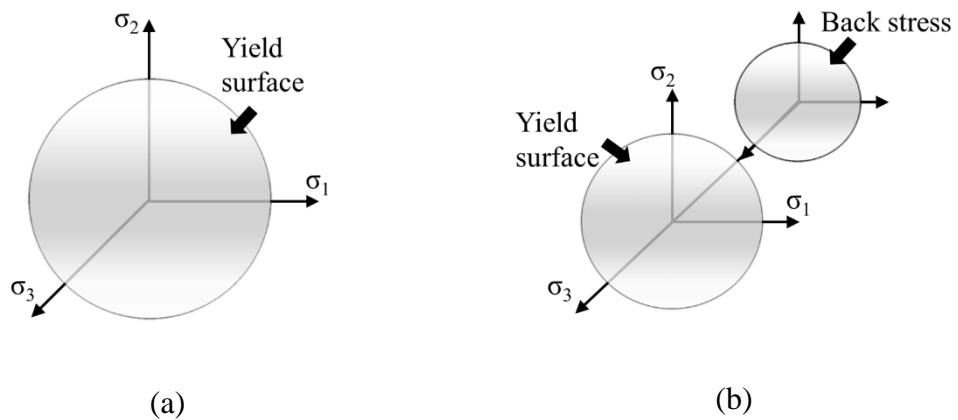


Figure 4. 3 Schematic representation of the evolution of yield surface in the principle stresses space during (a) isotropic and (b) kinematic plasticity rule

The equivalent plastic stress is calculated following the Equations 4.5 and 4.6.

For isotropic plasticity,

$$f[\sigma_{ij}, \kappa(\varepsilon_{ij}^p)] = \sigma_e(\sigma_{ij}) - \sigma_f(\varepsilon_{ij}^p) = 0, \quad (4.5)$$

and for kinematic plasticity,

$$f[\sigma_{ij}, \alpha_{ij}(\varepsilon_{ij}^p)] = \sigma_e[\sigma_{ij} - \alpha_{ij}(\varepsilon_{kl}^p)] - \sigma_s = 0, \quad (4.6)$$

where,  $\sigma_s$  is initial yield strength,  $\sigma_e$  is von Mises stress,  $\sigma_f$  is the new yield stress evolved due to the plastic strain increment  $\varepsilon_{ij}^p$ ,  $\kappa$  is the work-hardening parameter and  $\alpha_{ij}$  is called the back stress which is resulted in because of the translation of yield surface in kinematic plasticity. In practical cases, most metals and alloys show combined behaviour in case of plastic deformation [92]. ANSYS follows an iterative algorithm to calculate plastic strain, for details see the ref. [93].

#### 4.2.1 2D FEM thermomechanical model set-up

The circular cross-section of the cylindrical sample, shown in Figure 3.5a in chapter 3, has been taken as the geometry for the transient 2D FEM thermomechanical modelling. The diameter of the circular section is 10 mm. The direct coupling technique has been used to create the thermomechanical effect. In coupling method, the output temperature distribution of thermal analysis is used as input for structural analysis as thermal loads. Plane 223 element type is selected for the FEM analysis. This element type has direct coupling effect where the thermal and structural both analyses are run simultaneously which saves simulation time. The weak coupling is set prior to the analysis to establish one directional dependency among the degrees of freedom (Temperature, Displacements in X and Y directions), which means only temperature distribution from the thermal analysis dictates the displacement of the material in structural analysis. Plane 223 is a

higher order element with 8 nodes and up to 4 degrees of freedom. Higher order element means, it has middle nodes which can calculate very small deflection with better accuracy and useful for meshing non-linear geometry like circle or cylinder. It is compatible for simulating elastic, plastic deformation and large deflection of metals and alloys. The circular geometry has been meshed using quadratic shaped of Plane 223 element. The outer area along circumference has been meshed with fine elements and inner area with coarse mesh (see Figure 3.5a). The total number of elements in this model is 9444 and nodes is 29173 (because of the middle nodes). For this transient thermomechanical analysis, the length of the time step has been taken  $1 \times 10^{-6}$  s considering the short residence time (0.15 ms). Constant heat flux calculated from Equation 3.6 has been applied as the thermal boundary condition, which ultimately has been applied as temperature gradient for structural analysis. The convection and radiation losses have been ignored as the beam lasts for very brief period and irradiates locally over a tiny small area. For structural boundary condition, the centre of the circular model has constrained to prevent free rigid-body motion as in [75,94]. That means the displacement of central node in both X and Y direction has been set to zero. This minimum fixation of the model has been considered in order to induce residual stress by thermal loads rather from overconstraint model [94]. Temperature dependant physical and mechanical properties of H13 tool steel have been input in the analysis. The values of density, thermal conductivity, specific heat are taken from the Table 3.4 put in chapter 3. The temperature dependent thermal expansion coefficient is listed in Table 4.1.

Table 4. 1 Temperature dependent thermal expansion coefficient of H13 tool steel [87]

<b>Temperature, K</b>	298	373	673	873	1073	1273	1473	1673	1873
<b>Coefficient of thermal expansion, <math>\times 10^{-6} \text{K}^{-1}</math></b>	10.3	11.2	12.1	12.7	12.9	13.6	14.1	14.2	14.2

For elastic and plastic phenomena Young's modulus, Poisson's ratio, yield strength and tangent modulus of H13 tool steel are also considered. These properties have been taken

from the literature and plotted in a graph against temperature [87]. Figure 4.4 shows in graph, the variation of those mechanical properties with temperature.

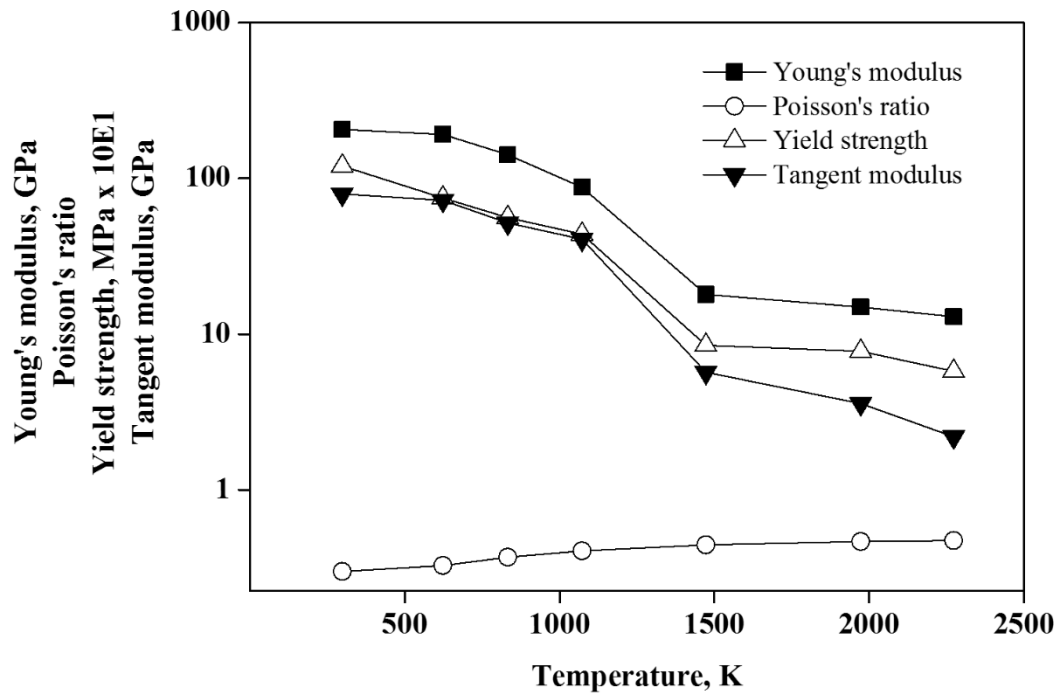


Figure 4. 4 Temperature dependent Young's modulus, Poisson's ratio, yield strength and tangent modulus of H13 tools steels input in the model [89]

The 2D thermomechanical model of H13 tool steel has been conducted for 200 and 300 W laser power at 0.2 mm beam width and 0.15 ms residence time. Temperature change rate, stress and strain have been predicted from this 2D transient thermomechanical model.

### 4.3 Results and discussion

#### 4.3.1 Temperature change rate, $dT/dt$

The temperature change rate ( $dT/dt$ ) has been calculated in ANSYS time-history post-processor. The data  $dT/dt$  for a point (centre of the heat source) on the surface has been plotted against time in Figure 4.5. The rate of heating at 200 W power is almost linear over the heating period. However, it slightly varies after 0.124 ms when the surface

temperature reaches the melting point at power 300 W. This change might be numerical, as in ANSYS thermal properties beyond the melting point (1727 K) has been kept almost constant for H13 tool steel. Sharp cooling has been noticed just after removing heat source at 0.15 ms. Temperature has dropped very quickly almost within 0.003 ms. A large thermal gradient is obvious at that time. After that, the rate of cooling has been decreased because of the reduction in temperature difference between heated area and bulk. The heating rates have been calculated  $1.05 \times 10^7 \text{ Ks}^{-1}$  and  $2.18 \times 10^7 \text{ Ks}^{-1}$  and cooling rates  $6.65 \times 10^7 \text{ Ks}^{-1}$  and  $1.51 \times 10^8 \text{ Ks}^{-1}$  for the laser power 200 W and 300 W respectively. The high temperature gradients (1603-298) K =1305 K, (2459-298) K =2161 K for corresponding laser power 200 W, 300 W and higher cooling rates indicate the presence of thermal residual stress in the system [46].

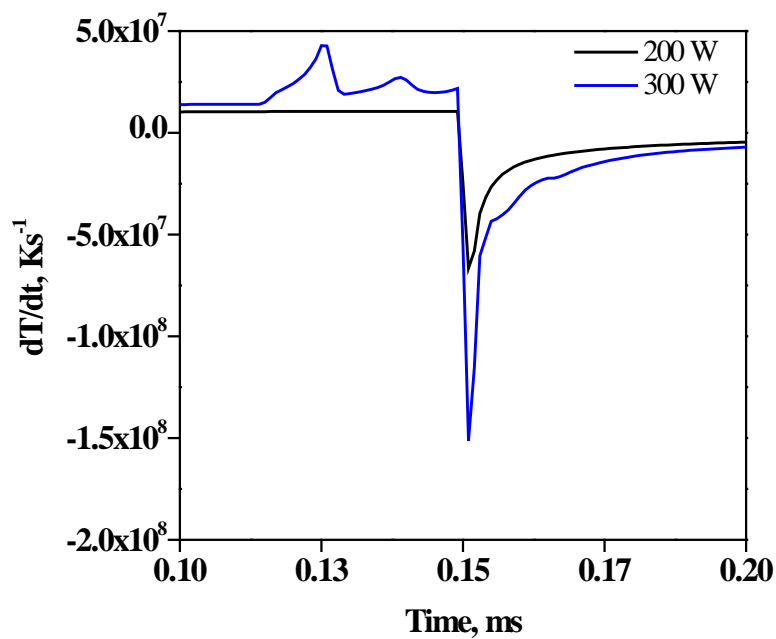
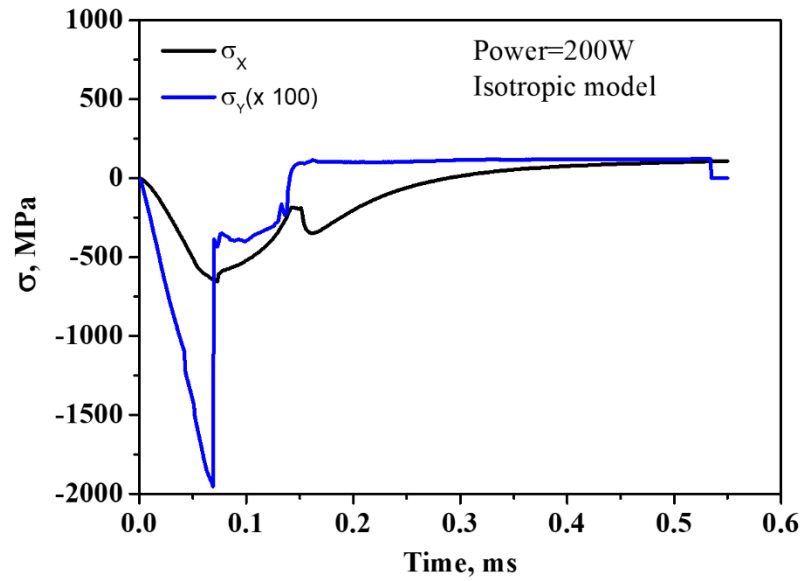


Figure 4. 5 Temperature change rate (dT/dt) vs. time plot for 200 W and 300 W laser power

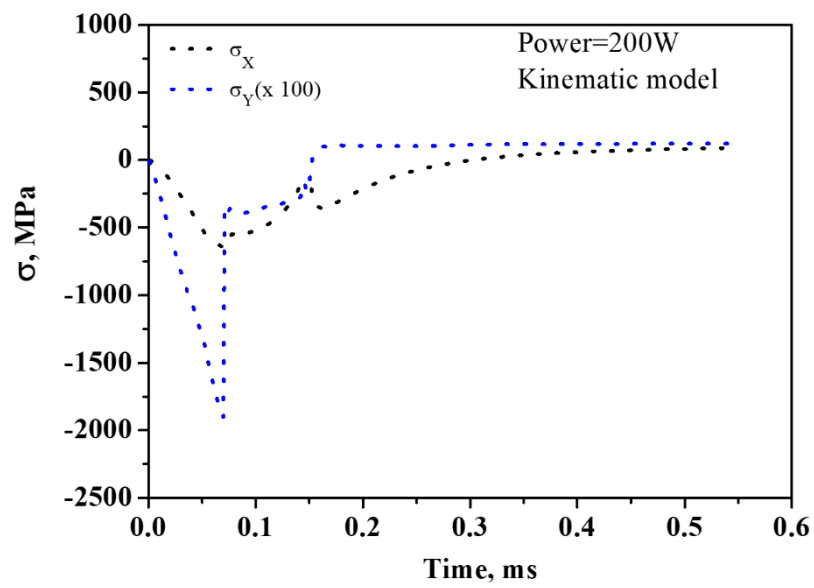
### 4.3.2 Stress and strain

#### *Stress vs. time*

The stress in both X ( $\sigma_X^{total}$ ) and Y ( $\sigma_Y^{total}$ ) directions have been plotted against time for two different power levels 200 W and 300 W applying two different plasticity models. The purpose of this study is to realise the nature of the stress generated in the system due to temperature gradient. Besides, the relation of laser power and plasticity models with the level of stress after the treatment has been observed. Figure 4.6 illustrates stresses predicted for 200 W laser power. The value of  $\sigma_Y^{total}$  stress has been scaled up 100 times as it is smaller than  $\sigma_X^{total}$  value. Therefore, X-directional stress has predominant effect on the modified surface. Both stresses have been taken from the surface where maximum temperature has been achieved, which is in the centre of line heat source (see Figure 3.5a). During heating,  $\sigma_X^{total}$  is compressive shown in Figure 4.6a. After 0.15 ms when cooling started, this stress has transformed to tensile stress. The Y-directional stress,  $\sigma_Y^{total}$ , is also in compression during heating time. After cooling,  $\sigma_Y^{total}$  also has transformed to the tensile state, but in a very fluctuating manner. This fluctuation could be because of the change of material properties at high temperature and mesh quality. Over the heating period, both  $\sigma_X^{total}$  and  $\sigma_Y^{total}$  have started increasing and it goes to a maximum compressive value at 0.07 ms. Then both stresses have decreased until the maximum surface temperature has reached at 0.15 ms. At the onset of cooling the stresses have transformed to the tensile nature and become stable when surface cooled down. In case of kinematic model shown in Figure 4.6b, the trend has been repeated by both  $\sigma_X^{total}$  and  $\sigma_Y^{total}$  in lower values.



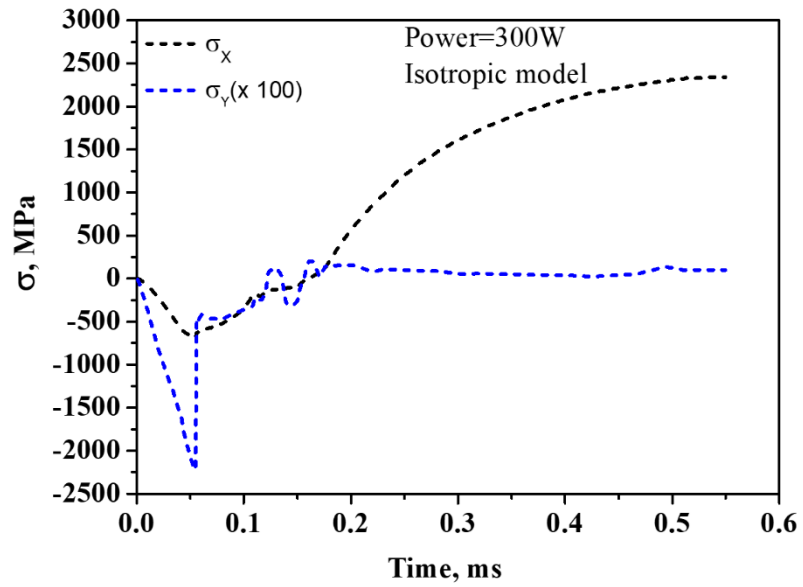
(a)



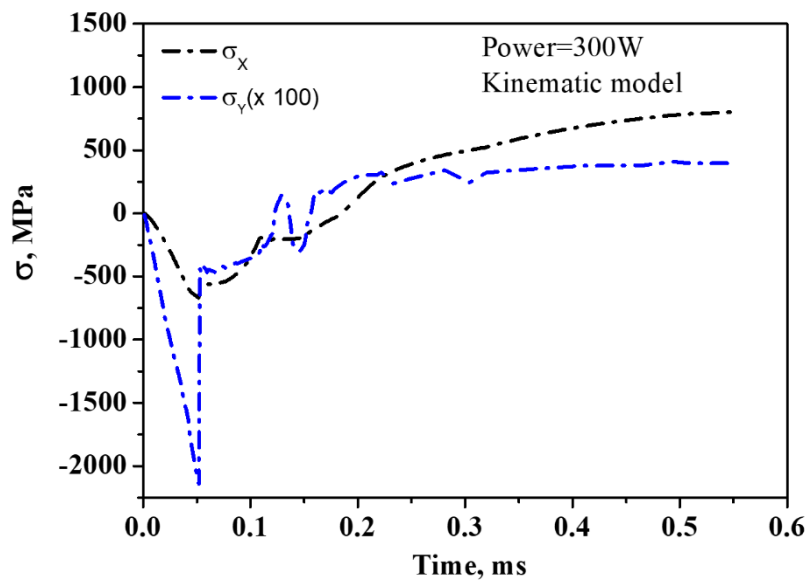
(b)

Figure 4. 6 X and Y directional normal stress distribution with time at 200 W laser power from (a) isotropic and (b) kinematic plasticity models

For 300 W laser power  $\sigma_X^{total}$  and  $\sigma_Y^{total}$  have been plotted over time in Figure 4.7 for both isotropic and kinematic models. The trend of both stress distributions is same as 200 W power. The value for maximum X-directional compressive stress during heating has slightly increased from 649 MPa to 686 MPa. However, after cooling at 0.55 ms, the  $\sigma_X^{total}$  on the surface has increased significantly to 2340 MPa which is beyond the yield strength of H13 tool steel (1280 MPa). Therefore, with increasing laser power stresses are increasing. The X-axis stress has predominating effect on the modified surface. For isotropic model tensile stress increment is significantly higher than the kinematic model.



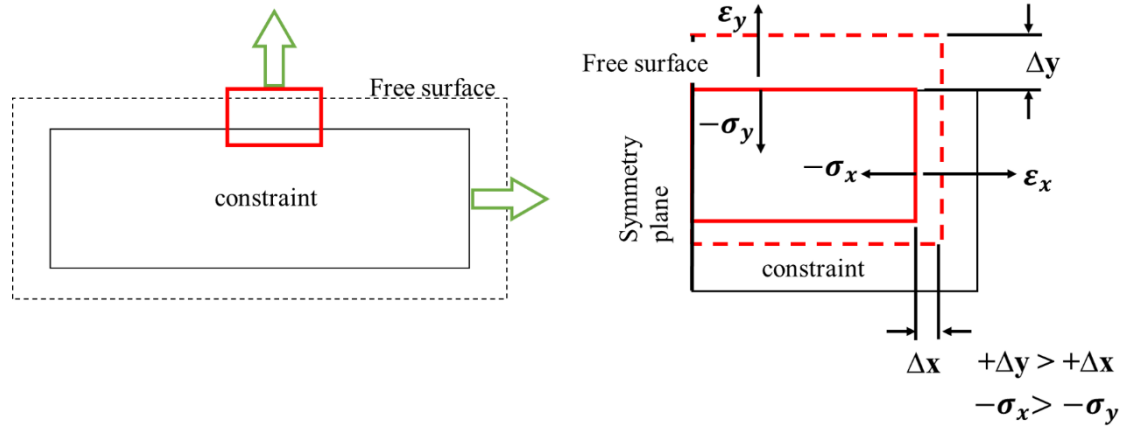
(a)



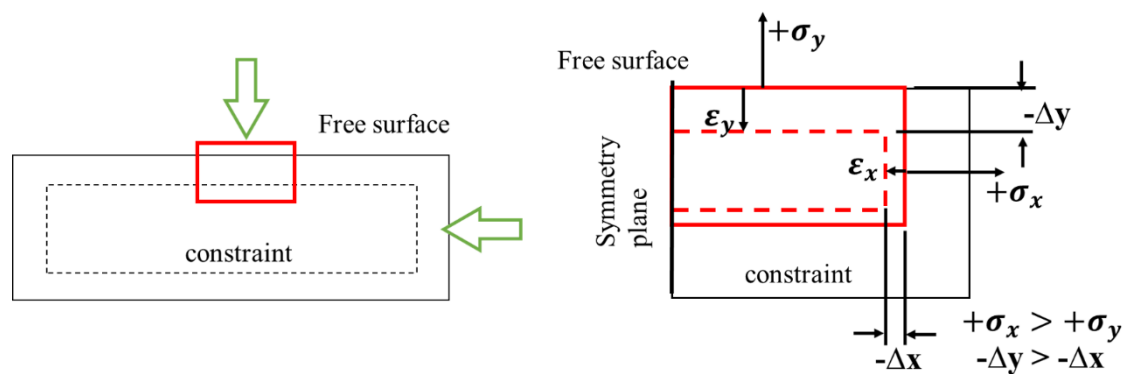
(b)

Figure 4. 7 X and Y directional normal stress distribution with time at 300 W laser power from (a) isotropic and (b) kinematic plasticity models

The compressive to tensile transformation of the resultant stress can be explained by simple relation with thermal strain. A schematic representation of the stress generation mechanism has been illustrated in Figure 4.8.



(a) Heating stage



(b) Cooling stage

Figure 4. 8 Mechanism of stress generation on the surface in (a) X and (b) Y direction based on thermal expansion coefficient and temperature gradient principle

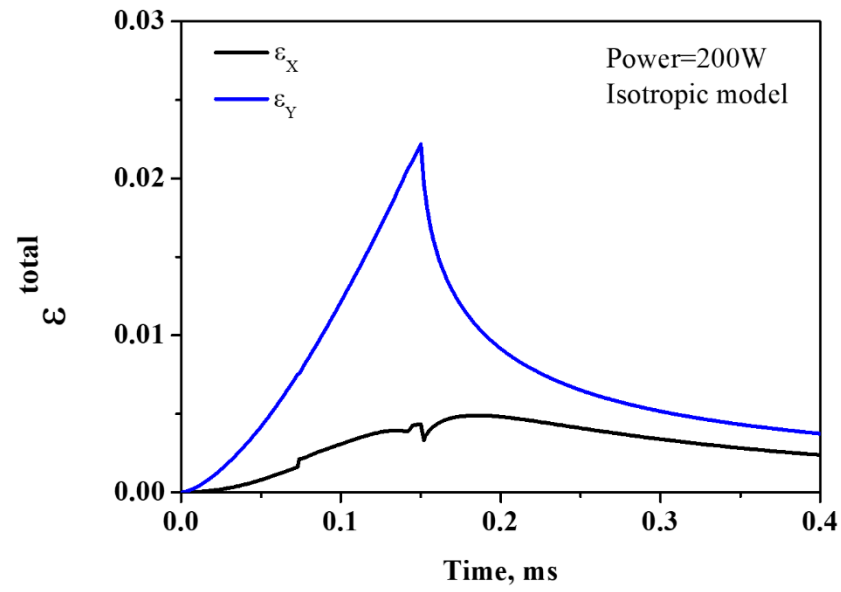
Figure 4.8a shows the compressive stress generation on the surface during heating stage. At this stage, the heated surface area tends to expand because of temperature gradient and thermal expansion coefficient. The expansion will be from every direction because of linear thermal expansion coefficient. If an element is taken from the surface denoted by the red rectangular box in Figure 4.8a, then the right-hand side picture shows that in both

X and Y dimensions material is expanding. In Y direction, the material located on the free surface expands more because it does not have any obstacle on top of it. However, in the X direction, the heated part will expand less because the displacement will be restricted by the cold material next to it. Thus, in Figure 4.8a it is shown that  $+\Delta y$  is greater than  $+\Delta x$ . This displacement creates strain in both X and Y direction which eventually apply force outwardly due to the material bonding. The response of this outward force due to temperature gradient results into compressive stresses in both X and Y directions. The magnitude of Y direction compressive stress is less because of the free surface. On the other hand, the X directional compressive stress shows higher value due to material constraint. Similarly, Figure 4.8b illustrates the tensile stress generation at cooling stage. During cooling material tends to contract inwardly. As a result, the cold part obstructs the contraction due to the bonding. In Y direction, the free surface has less obstacles than the X direction materials. Therefore, the Y directional stress is lower than the X directional tensile stress. Similar concept was found in a conceptual model of developing residual stress for laser cladding process [95]. Increasing laser power elevates peak temperature and consequently thermal gradient increases. The thermal expansion coefficient follows proportional relationship with temperature. Thus, in isotropic model, the magnitude of both X and Y directional stresses have increases with laser power. However, as the current model calculates stress following the thermo-elastic-plastic constitutive law, further investigation will be carried out to understand the effect of separate strain components on the stress. In the kinematic model, correlation between total stress of the modified surface and laser power is also proportional. However, due to the shift strain of the evolved yield surface the stress has reduced value than the isotropic model. Figure 4.8 is the simplified conception of thermal stress generation on the modified surface in LSG. However, there may have some effects of Poisson ratio and plastic strain increments theory on the residual stress generation. This is the limitation of

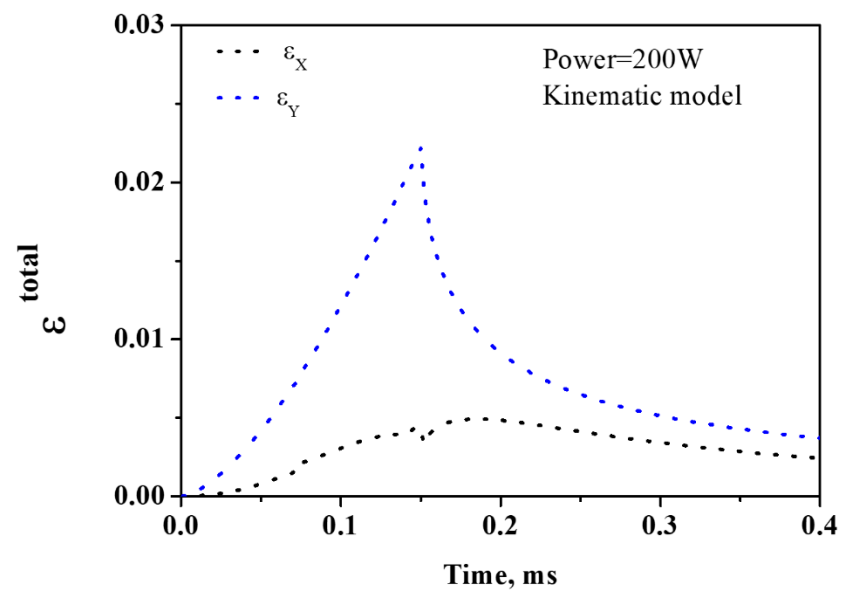
the current thermomechanical model which will be overcome by 3D extension of the model and further analysis.

#### *Strain vs. time*

The total strain for X ( $\epsilon_X^{total}$ ) and Y ( $\epsilon_Y^{total}$ ) directions versus time has been illustrated in Figure 4.9. Both X and Y directional strains have increased as heating progressed and reached to the maximum values when surface achieved the peak temperature at 0.15 ms. After cooling both directional strains have decreased. The magnitude of the  $\epsilon_Y^{total}$  is higher than the  $\epsilon_X^{total}$  which is already described in Figure 4.8. Therefore,  $\epsilon_Y^{total}$  has higher value due to the larger displacement allowed by the free surface, while  $\epsilon_X^{total}$  shows lower value due to the material constraint. The peak value of both X and Y directional strains have increased with laser power at 0.15 ms. At 300 W laser power both  $\epsilon_X^{total}$  and  $\epsilon_Y^{total}$  fluctuates during the transition period from heating and cooling. The fluctuation is mainly caused by the material properties input in the analysis. The correct relationship of material properties during transition of solid to liquid transformation is important to know for better accuracy. It is also observed that strain in X-direction is smaller than the Y-direction. The magnitudes of both directional strains are slightly higher in case of isotropic model than kinematic.

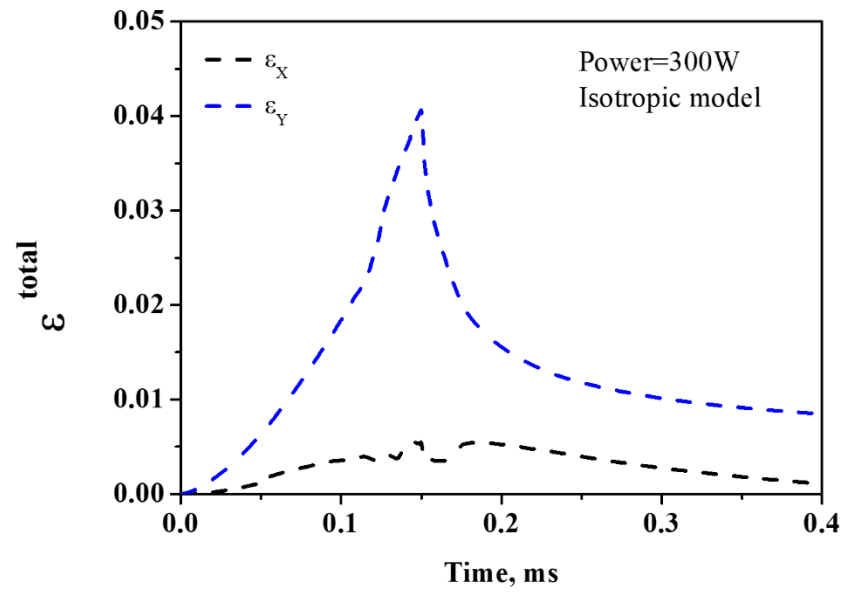


(a)

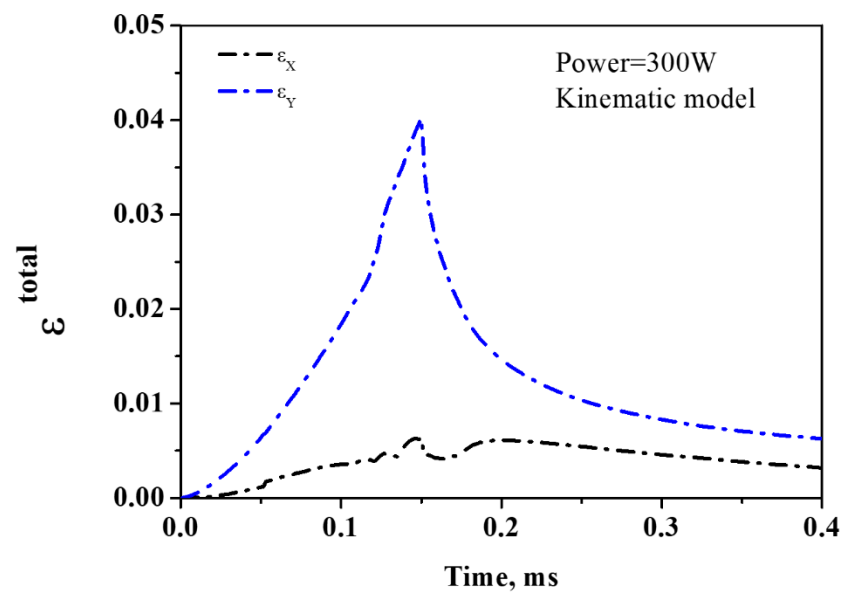


(b)

Figure 4. 9 X and Y directional normal strain vs. time at 200 W laser power from (a) isotropic and (b) kinematic plasticity models



(a)



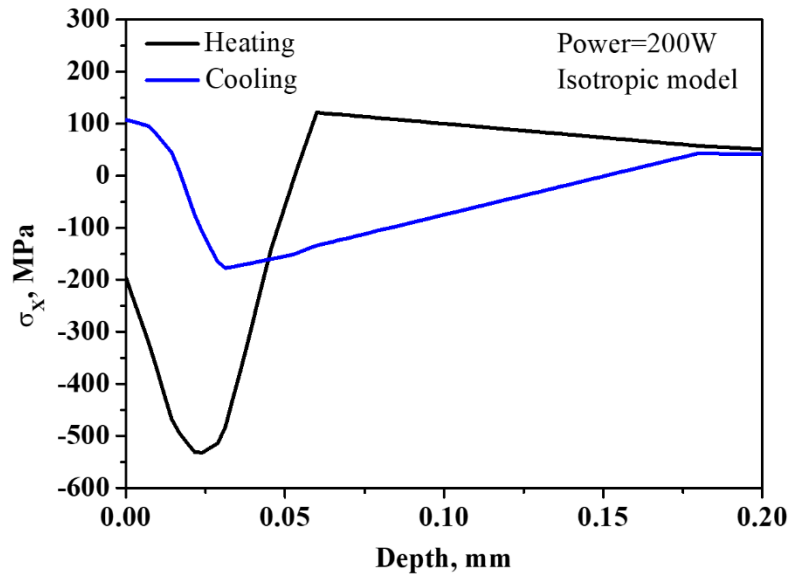
(b)

Figure 4. 10 X and Y directional normal strain vs. time at 300 W laser power from (a) isotropic and (b) kinematic plasticity models

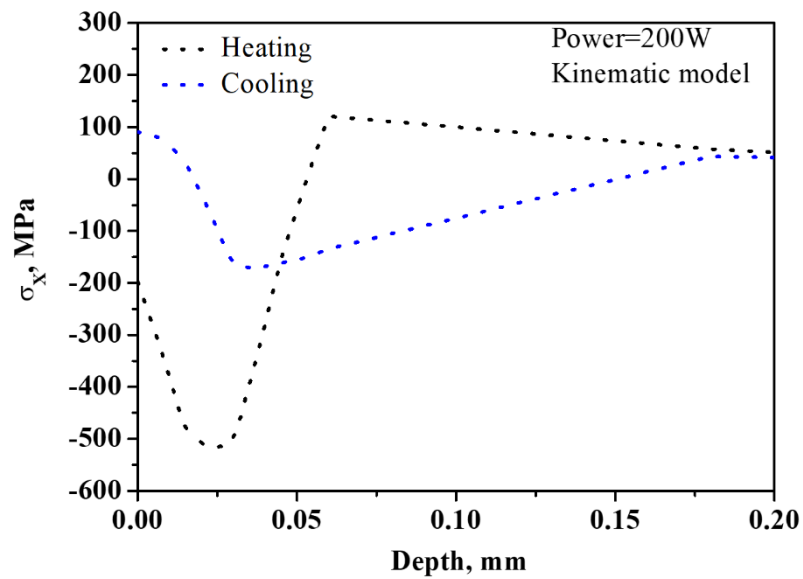
*Stress vs. distance from the surface to centre*

Figure 4.11 and 4.12 present  $\sigma_x^{total}$  along distance from surface to centre of the circular model for 200 W and 300 W laser powers respectively. Both isotropic and kinematic plasticity models have been examined for each laser power. During heating, when surface is at peak temperature at 0.15 ms, the  $\sigma_x^{total}$  on the surface is in compression for the maximum expansion of the surface material. Therefore, the underneath materials go in tension due to the bonding with surface material. Similar trend was reported for laser cladding of H13 tool steel substrate at laser power 2200 W, beam width 3 mm, scan speed 200 mm.min<sup>-1</sup> [54]. During cooling, the surface experiences highest tensile stress because of the contraction. The underneath material then goes in to compression. The concept mentioned in Figure 4.8 has reflected in the numerical data of stress distribution through the depth. In Figure 4.11a isotropic model shows that, highest compressive stress achieved 532 MPa at 0.024 mm depth from the surface at heating. The highest tensile stress is 108 MPa on the surface after cooling. Isotropic and kinematic models show same pattern over heating and cooling at laser power 200 W. The values of tensile and compressive stresses are slightly lower in kinematic case, shown in Figure 4.11b. For the laser power 300 W and isotropic model (Figure 4.12a), the highest compressive stress 577 MPa is achieved at 0.036 mm depth during heating. However, after cooling period at 0.55 ms, the surface gets 2340 MPa tensile stress, which is significantly higher than the yield strength of H13. For kinematic model shown in Figure 4.12a,  $\sigma_x^{total}$  on the surface decreases to 800 MPa than the isotropic case. The highest compressive stress is 550 MPa at 0.036 mm depth, almost same as isotropic case. Therefore, stress on surface after cooling increases with laser power for both isotropic and kinematic plasticity models. The isotropic models give higher value than the kinematic but showed same trend. This is due to the evolution of yielding which may increase proportionally with thermal gradient

resulting into higher residual stress in isotropic case, whereas in kinematic model, the surface stress reduced due to the shift strain of yield surface.

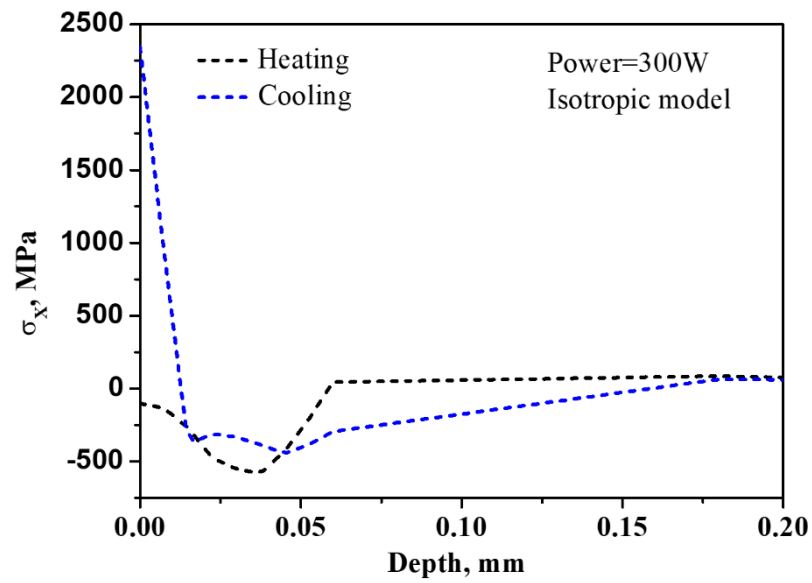


(a)

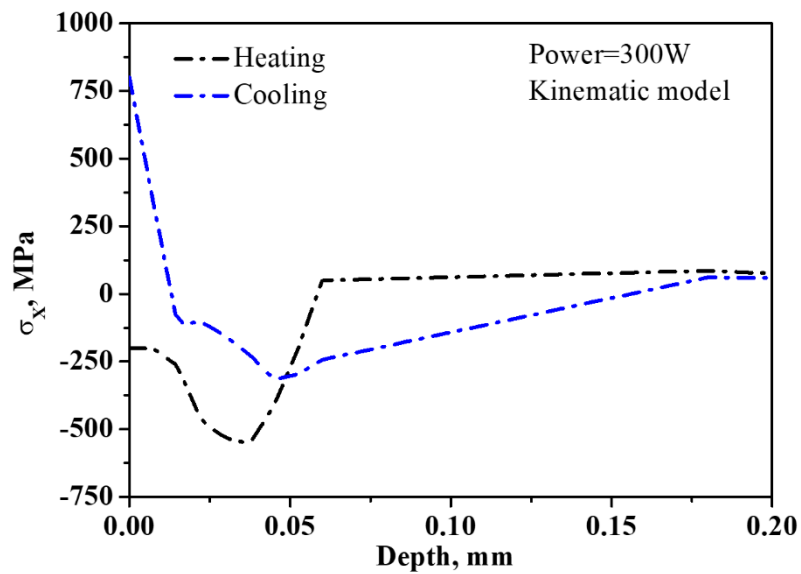


(b)

Figure 4. 11 Stresses in X direction ( $\sigma_x^{total}$ ) vs. distance from surface to centre during from the (a) isotropic and (b) kinematic models at 200 W laser power after both heating (0.15 ms) and cooling (0.55 ms)



(a)



(b)

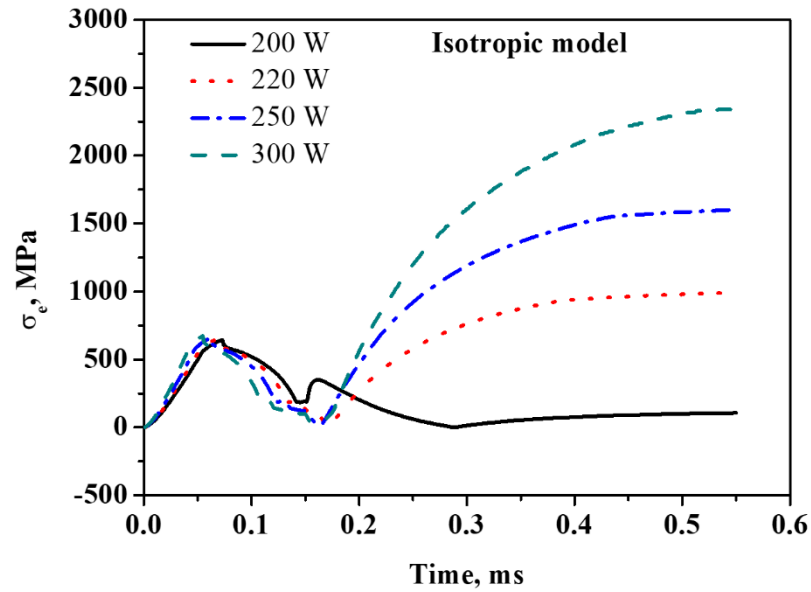
Figure 4. 12 Stresses in X direction ( $\sigma_x^{total}$ ) vs. distance from surface to centre during from the (a) isotropic and (b) kinematic models at 200 W laser power after both heating (0.15 ms) and cooling (0.55 ms)

### 4.3.3 Prediction of crack formation

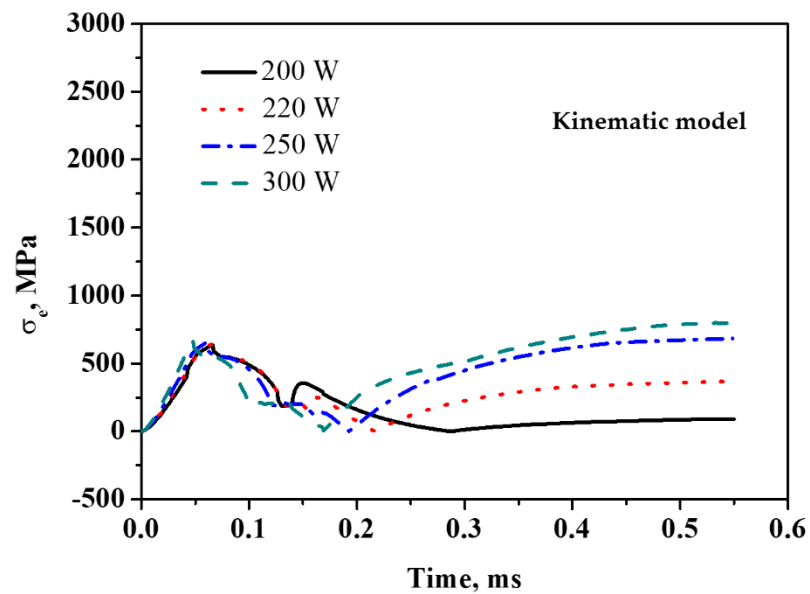
The equivalent stress,  $\sigma_e$  (von Mises stress), is an important indicator to understand the crack formation of the sample surface due to the residual stresses developed during LSG treatment. Figure 4.13 depicts equivalent von Mises stress of a point on surface (centre of the projected beam, see Figure 3.5a) over processing time for various power levels. In this plane stress model, the equivalent stress is reflecting the value of  $\sigma_x^{total}$  as the X-axis stress has significantly higher value than the Y-axis stress. The important aspect of this graph is to examine the highest tensile stress reaching after cooling at 0.55 ms for four power levels shown in Table 4.2. Therefore, the lowest tensile stress has been observed 108 MPa for 200 W. Highest tensile stress 2340 MPa has been achieved at highest laser power 300 W, which is beyond the yield strength of H13 (1280 MPa) showing crack formation tendency. The two intermediate laser powers 220 W and 250 W have shown respectively 992 MPa and 1600 MPa. Therefore, the residual stress in the laser modified surface can cross the yield point if the operated laser power during LSG process is set within 220 W to 250 W. Thus, the present developed thermomechanical model can be used to optimise the laser power to avoid crack formation on the laser glazed surface. For kinematic rule, the equivalent stress distribution followed similar trend like isotropic model with variable laser power. However, the tensile stresses generated after cooling have given lower value given in the Table 4.2. Therefore, the isotropic plasticity model gives higher value than the kinematic model which also reported in [51].

Table 4. 2 The equivalent Mises stress for different power levels and plasticity models

Laser power, W	$\sigma_e$ , MPa (isotropic)	$\sigma_e$ , MPa (kinematic)
200	108	90
220	992	368
250	1600	684
300	2340	800



(a)



(b)

Figure 4. 13 Variation in the equivalent von Mises stress ( $\sigma_e$ ) over time for the (a) isotropic and (b) kinematic plasticity models for different laser powers

#### 4.4 Summary

A 2D thermomechanical coupled model of LSG for H13 tool steel has been successfully developed. The model can predict thermo-elasto-plastic residual stress based on

temperature gradient approach. The model has been conducted for 200 W and 300 W laser power with constant 0.2 mm beam width and 0.15 ms residence time. Plastic part of residual stress has been modelled for two different rate-independent plasticity theory, isotropic and kinematic. Results have shown that at peak temperature surface has experienced compressive stress and it has turned to tensile stress after cooling. The X-axis stress shows significantly higher value than the Y-axis stress, thus, is predominant in the system. The total stresses in both X and Y directions has increases with increasing laser power in both plasticity models. However, Isotropic model gave higher values of X and Y directional stresses than the kinematic model. The total strain increments for both X and Y directions are proportional to the temperature rise. The Y-directional strain is higher than the X-directional strain. Both isotropic and kinematic models have given same strain value for different laser powers. After cooling, the X-axis stress becomes tensile on the surface and changes to compressive along the depth inside from surface. The von Mises equivalent stress on surface after cooling increases with laser power. Laser powers 250 W and 330 W give the stress respective 1600 MPa and 2340 MPa which are above the yield strength of H13 steel for isotropic model. For kinematic model, highest von Mises stress has achieved 800 MPa at 300 W which is below the yield strength. To decide the applicability of plasticity models will need validation of stress measurement of LSG treated surface part. However, to understand the residual stress generation mechanism and selecting laser parameter windows, the FEM model will be the useful way along with experimental method.

-----X-----

# Chapter 5

## Parametric study of the LSG model

### 5.1 Introduction

In this chapter, a parametric study has been carried out with the developed FEM thermal model of LSG for metallic materials. Initially, the 3D thermal model with cylindrical geometry and uniform heat source has been analysed by varying laser power for both H13 tool steel and Ti6Al4V alloy. Then this 3D thermal model for Ti6AL4V alloy has been optimised for two surface and volumetric heat source models.

#### 5.1.1 Laser surface glazing of Ti6Al4V alloy

Since 1930, Ti6Al4V alloy is introduced as a bio-implants material [96] for its high strength-to-weight ratio, good corrosion resistance [5,72,97] and better ability of joining bones with implants (known as Osseo-integration) [98]. These properties make Ti6Al4V alloy preferable as bone and dental implants [99,100], over the other biocompatible metallic materials such as 316L stainless steel, Cobalt and Vanadium steels [96]. However, the implants surface made of Ti6Al4V alloy erodes easily due to the poor hardness and wear resistance. The debris coming off the worn surface gets mixed with blood and bone cells which causes serious infection in the human body [15,101]. Therefore, over the last two decades, laser surface modification techniques [102–105], especially LSG [5,99], have been used to improve surface hardness and wear resistance of Ti6Al4V alloy. Comparing to other laser surface modification processes [102,103,105], E. Chikarakara et al. reported that LSG offered an outstanding increment (67%) in surface hardness of Ti6Al4V alloy than the untreated surface [5,99]. Along with improving hardness LSG also enhances wear, corrosion resistance and biocompatibility

of the treated surface. Therefore, it is important to optimise laser parameters for Ti6Al4V alloy to achieve required surface hardness. As surface hardness depends on the temperature distribution, through modelling it is easier to analyse peak surface temperature on the surface for variable laser parameters and can be optimised. The composition of Ti6Al4V alloy has been presented in Table 5.1.

Table 5. 1 Chemical composition of Ti6Al4V alloy in %weight [44]

<b>Element</b>	C	Si	Fe	O	V	Al	Ti
<b>%weight</b>	0.14	0.01	0.16	0.17	3.97	6.36	Balance

### 5.2 3D thermal model of LSG for different laser power

A parametric study with varying laser power of 3D thermal model has been carried out for both Ti6Al4V alloy and H13 tool steel. The 3D thermal model was developed in chapter 3 with half-cylindrical geometry. The model was analysed with H13 tool steel for 200W and 300W laser power with 0.2 mm beam width and 0.15 ms residence time. The analysis showed that more than 200 W laser power needs to initiate melting in LSG of H13 tool steel. In a previous experimental work of LSG for H13 tool steel reported that 249 W laser power of CO<sub>2</sub> pulse laser required to achieve molten zone with 0.2 mm beam width [3]. Then the established 3D thermal model of LSG has been utilised in this parametric study for different metal, Ti6Al4V alloy. Ti6Al4V alloy and H13 tool steel both have nearly similar melting points. However, Ti6Al4V alloy has lower thermal conductivity than H13 tool steel. The aim of this study is to find out the starting or threshold laser power required to initiate melting of both Ti6Al4V and H13 tool steel alloys by varying laser power within the selected range. Laser power is an important processing parameter for LSG process because appropriate laser power ensures the correct temperature distribution on the surface. This temperature distribution ultimately

controls the surface structure and expected level of surface hardness. Moreover, the required laser power will indicate the capacity of laser machine essential to process the specific materials. The range of laser power has been varied from 100 W to 140 W for Ti6Al4V alloy and for H13 tool steel from 200 W to 240 W. The starting power for Ti6Al4V alloy [15] and H13 tool steel [3] has been decided from the experimental works. The beam width and residence time have been kept constant at 0.2 mm and 0.15 ms respectively for comparison between two alloys. The laser parameters used for Ti6Al4V alloy and H13 tool steel have been presented in Table 5.2.

Table 5. 2 Laser parameters used for Ti6Al4V and H13 tool steel alloy

<b>Materials</b>	<b>Beam width, mm</b>	<b>Residence time, ms</b>	<b>Laser power, W</b>
Ti6Al4V	0.2	0.15	100-140
H13 tool steel	0.2	0.15	200-240

The FEM model has been set up as mentioned in chapter 3. The heat flux has been considered constant surface heat flux with uniform heat distribution, expressed in Equation 5.1 for the CO<sub>2</sub> continuous wave laser beam.

$$Q_{laser} = \frac{AP}{\pi r_{beam}^2} \quad (5.1)$$

where,  $Q_{laser}$  is laser intensity,  $P$  is laser power,  $r_{beam}$  is beam radius and  $A$  is the absorptivity of material to the laser light. The thermo-physical properties of Ti6Al4V alloy has been presented in Table 5.2, whereas for H13 tool steel the physical properties have been given in Table 3.3 of chapter 3.

Table 5. 3 Thermo-physical properties of Ti6Al4V alloy as a function of temperature

[41,72]

<b>Temperature, K</b>	298	373	573	773	973	1173	1373	1573	1773
<b>Density, kgm<sup>-3</sup></b>	4420	4406	4381	4350	4324	4294	4267	4240	4205
<b>Thermal Conductivity, Wm<sup>-1</sup>K<sup>-1</sup></b>	6.8	7.4	9.8	11.8	13.5	20.2	21	23.7	25.8
<b>Specific heat, Jkg<sup>-1</sup>K<sup>-1</sup></b>	546	562	606	651	694	734	660	696	732

### 5.2.1 Results and discussion

Figure 5.1 illustrates the peak surface temperature against various laser power within the ranges selected for Ti6Al4V alloy and H13 tool steel. For Ti6Al4V alloy, laser power 100 W gives 1670 K which is below the melting point. With increasing laser power, the peak surface temperature has increased. From Figure 5.1, it is observed that at 130W Ti6Al4V alloy attains 1938 K peak surface temperature which is just above the melting point (1933 K). Similarly, H13 tool steel has achieved 1669 K surface peak temperature at 200 W laser power that is below the melting point. At laser power 210 W, temperature has risen to 1735 K peak surface temperature above the melting point (1727 K). This study shows the ranges of laser power level more precisely to occur melting in the surface for both Ti6Al4V alloy and H13 tool steel at 0.15 ms residence time. Moreover, the threshold laser power has also been identified which helps to straightforwardly decide operating laser power during the experiment. However, this range of laser power can be changed by altering residence time. With increasing residence time, the lower laser power can give higher surface peak temperature. For instance, in a previous experimental work of LSM of Ti6AL4V alloy melting occurred at 100 W laser power for 2.16 ms residence

time [15]. The effect of residence time of LSG will be accomplished in future work with this 3D model.

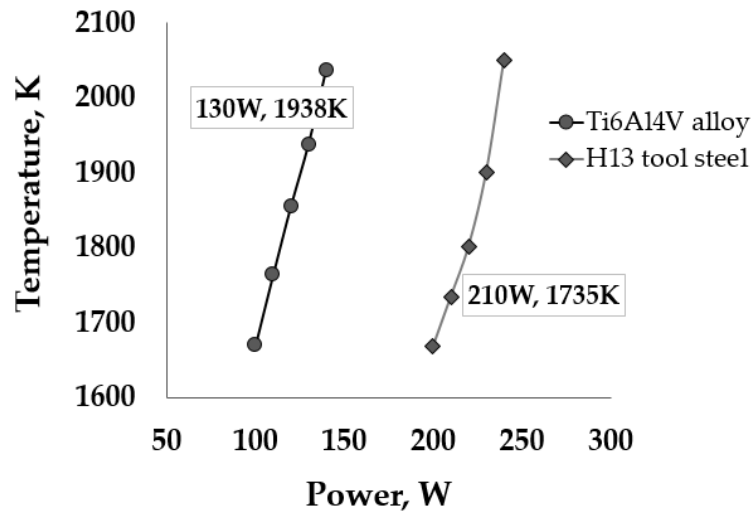


Figure 5. 1 Variation of peak temperature at different laser powers from the 3D FEM thermal model of Ti6Al4V alloy and H13 tool steel using surface heat flux

Figure 5.1 shows that with increasing laser power peak surface temperature is increasing. The higher peak temperature, the larger the molten area which will give higher depth of modified layers from LSG. From the linear relationship with laser power and peak temperature, it is understood that laser power above 140 W will increase peak temperature linearly for Ti6Al4V alloy. Similarly, above 240 W laser power H13 tool steel will attain higher surface peak temperature which is obvious in the analysis at 300 W laser power presented in chapter 3. Therefore, this parametric study will be helpful to determine the starting parameters and regulate peak temperature, depth of modified layers by optimising laser parameters for LSG.

This study also shows that the correlation of the physical properties of material with the operating laser power in LSG process. Figure 5.1 shows that, although Ti6Al4V alloy has higher melting point, surface melting of this alloy occurs at lower laser power. On the other hand, the surface of the H13 tool steel melts down at higher laser power instead of

having lower melting point. The reason behind this can be explained with the thermal diffusivity  $\alpha$  ( $\text{m}^2\text{s}^{-1}$ ) for those materials [84]. Thermal diffusivity,  $\alpha = \frac{k}{\rho C_p}$ , which is the ratio of the thermal conductivity,  $k$ , and the product of the specific heat,  $C_p$ , and density,  $\rho$ , of the material. The thermal diffusivities are calculated  $2.9 \times 10^{-6} \text{ m}^2\text{s}^{-1}$  for Ti6Al4V alloy and  $8.6 \times 10^{-6} \text{ m}^2\text{s}^{-1}$  H13 tool steel. Ti6Al4V alloy has lower thermal conductivity than the H13 tool steel. Low thermal conductivity causes lower rate of heat diffusion through the material. This helps to accumulate heat locally resulting into higher surface temperature at lower heat flux as well as lower laser power. Therefore, material with lower thermal conductivity needs lower power to operate in LSG which is also revealed in [106]. This thermal model of LSG will help to select type of laser machine, high power or low power required for processing based on material type.

### 5.3 3D thermal model for different heat source

In this section, the 3D FEM thermal model has been conducted for Ti6Al4V alloy for two different types of heat source. The 3D half-cylinder has been taken as the model geometry as shown in Figure 3.5b. The laser heat source has been considered as CO<sub>2</sub> laser in continuous wave mode of 10.6  $\mu\text{m}$  wavelength. The heat flux from the laser beam has been assumed to have Gaussian distribution of TEM<sub>00</sub> mode. The thermo-physical properties, thermal conductivity and density have been applied from Table 5.2, but the values for specific heat has been modified considering the latent heat of fusion to include phase change (solid to molten) as in [19]. The model has been conducted using two types of heat source mentioned in following sub-sections for 100-300 W laser power. The starting range of laser power has been chosen 100 W because, a previous experimental study reported surface melting of Ti6Al4V alloy at that power for laser modification [15]. The beam width and residence time have been kept constant at 0.2 mm and 0.15 ms

respectively. The surface heat flux expressed in Equation 5.9 is applied in FEM model with SF command and the volumetric heat load with BF command.

### 5.3.1 Surface heat source

The surface heat source is assumed where heat flux is distributed on the surface over cross-sectional area of the projected beam. This is due to the absorption of the heat flux limited on the surface, the energy cannot penetrate inside the material. The limited absorption is due to the high reflection of laser beam for metals and alloys [31]. The Gaussian surface heat source is expressed in Equation 5.2 [43].

$$Q_{laser}(x, y) = \frac{2AP}{\pi r^2} \exp\left(\frac{-2(x_0^2 + y_0^2)}{r^2}\right) \quad (5.2)$$

where,  $Q_{laser}$  is heat flux or laser intensity,  $P$  is laser power,  $r$  is beam radius,  $A$  is the absorptivity and  $(x_0, y_0)$  is the origin of the spherical beam on the surface. The value of the absorptivity of Ti6Al4V alloy is taken 0.4 considering the flat surface absorption at 10.6  $\mu\text{m}$  wavelength [73].

### 5.3.2 Volumetric heat source

The volumetric heat source is considered when the laser beam penetrated beneath the surface by over a certain volume following the Beer-lambert's law. The heat flux or laser intensity distribution of a Gaussian volumetric heat source is expressed in Equation 5.3 [19].

$$Q_{laser}(x, y, z) = \frac{6AP}{\pi\sqrt{\pi}r^3} \exp\left(\frac{-3\{(x-x_0)^2 + (y-y_0)^2 + (z-z_0)^2\}}{r^2}\right), \quad (5.3)$$

where,  $Q_{laser}(x, y, z)$  is laser intensity as volumetric heat load,  $P$  is laser power,  $r$  is beam radius,  $A$  is the absorptivity and  $(x_0, y_0, z_0)$  is the origin of the spherical beam.

### 5.3.3 Results and discussion

The Time-temperature plot of this model at laser power 200W has been presented in Figure 5.2. Surface peak temperature has varied significantly for surface and volumetric heat load. Peak temperature for surface heat load has been obtained 4997 K which is significantly higher than the melting point (1933 K) of Ti6Al4V alloy. On the contrary, volumetric heat load has shown 1662 K peak temperature below the melting point. Laser power 100 W and 200 W were insufficient to raise temperature for volumetric heat load. The study has showed that application of volumetric heat load requires higher laser power than the surface heat load.

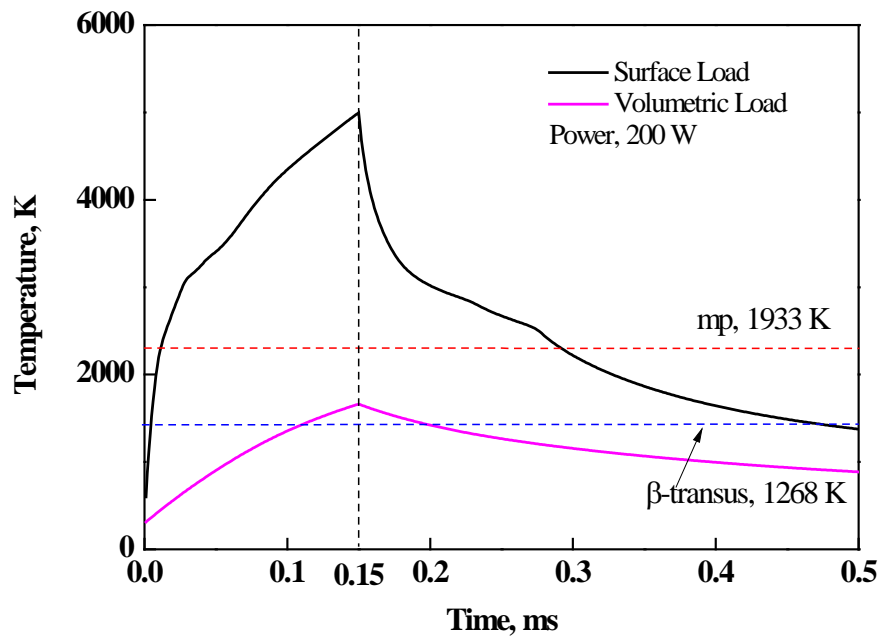


Figure 5. 2 Variation in temperature distribution for surface heat source and volumetric heat source at 200 W laser power for Ti6Al4V alloy

### 5.4 Summary

The parametric study of 3D thermal model of LSG has shown that this thermal model can be a useful tool in selecting process parameters for LSG for different metallic materials. The threshold laser power to initiate melting for H13 tool steel and Ti6Al4V alloy are 210 W and 130 W respectively using uniform heat source. There is no account found on

the suitability of surface heat source or volumetric heat source for LSG thermal modelling in the literature. Therefore, in this present work a parametric study has been carried out with both types of heat source. The results have shown that for volumetric heat load requires higher laser power than the surface heat load. Further analysis will be carried out to conclude the appropriate heat source model in order to improve the accuracy of LSG thermal model.

-----X-----

# Chapter 6

## Application of LSG thermal model in quenching and tempering

### 6.1 Introduction

In this chapter the developed FEM thermal model of LSG will be applied in similar surface treatment of structural steel. The quenching and tempering stage of thermomechanical hot rolling treatment produce dual phase steel for the application in the structural industries as high strength structural steel. The motto of this chapter is to verify the developed thermal model methodology in similar field of thermal treatment of metals and alloys.

#### 6.1.1 Quenching and Tempering in TMT

Thermomechanical treatment or TMT is an advanced hot rolling treatment to produce high strength low alloy (HSLA) steels with severe degree of deformation. The purpose of this process is to produce structural steel having very small grain size (2.5-50  $\mu\text{m}$ ) which renders very high strength with a little amount of carbon content (0.05 to 0.16 %) [107–109]. In TMT process quenching and tempering stage is integrated to produce dual phase steel with harder case and softer core of a rolled steel bar. The quenching step consists of a flow of water jet with a certain pressure and temperature along the surface of the rolled product right after last pass of rolling. This is happened in a closed chamber where the long product is kept in higher temperature (1200 °C or 1000 °C), above austenitic transformation temperature and allowed to pass for a few seconds. The surface temperature is suddenly dropped due to the quenching effect by convection and radiation heat transfer. A large thermal gradient between surface and inside core is caused leading

to the conduction of heat from core to the surface. This causes tempering of the surface which is called self-tempering. The austenite to martensite phase transformation occurs in the surface and sub-surface area due to cooling at faster rate than critical cooling rates. These martensites are decomposed to tempered martensites in the self-tempering stage. The austenites in the core cool down slowly and are transformed into ferrites and pearlites. A schematic diagram was illustrated in Figure 6.1 describing the quenching and tempering of TMT process.

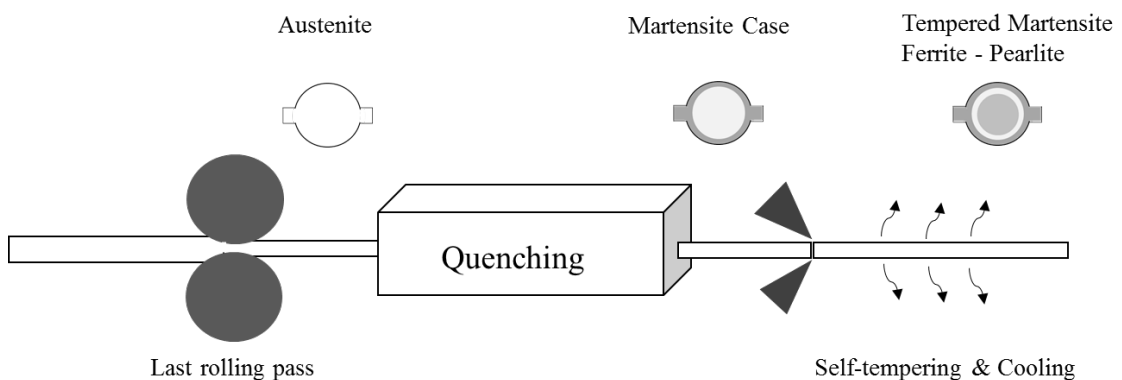


Figure 6. 1 Schematic diagram of quenching and tempering in TMT process after last rolling pass

### 6.1.2 Structure of TMT steel

The structure of TMT treated bar composed of three distinct zones of different microstructures and properties. These three zones are respectively a hard outer case, soft core and between two zones a transition area of having mixed structures and properties. High strength and hardness come from the outer case and soft core renders ductility which in combination improve the toughness of the reinforcing bars. Due to high hardness in outer surface TMT bar has good fatigue resistance. Generally in the structural application like constructing high rise building, marine structures and fire resistant structures, TMT treated steel bars are being used in a large scale [110–112].

The depth of case and the microstructures play vital role in the ultimate properties of TMT processed bar [111,113]. The temperature after last pass of rolling and equalization temperature or tempering temperature is very important in deciding the microstructures of case and core. The depth of case depends on the impingement density of quenchant medium, temperature of quenchant, and time of quenching. Impingement density defines total mass of quenchant sprayed on surface per unit area and time. All these parameters need to be optimised to attain required case depth, microstructures, and properties of TMT bars.

### 6.1.3 Previous relevant modelling works

There are some modelling works using analytical and numerical approach been conducted for quenching and tempering heat treatment processes for steels [114–119]. In early of the millennium, a mathematical model of quenching process of low Cr steel was done following finite volume method. In this simulation a transient cooling phase is modelled with hardening mechanism to predict cooling rates. This cooling rates is further used by Jominy end quench method to determine hardness for that steel. Microstructure and mechanical properties of this quenched steel were also predicted based on hardness and chemical composition. The accuracy of the estimated data from this numerical modelling is not mentioned in this study [114]. Later in 2006, a detail finite element (FE) modelling was done for quenching process for cylindrical sample to predict temperature fields, phase evolution, residual stress, and hardness distributions. The newly developed modelling technique was verified by 2-D analytical modelling of transient heat transfer problems and end-quench test using P20 steel. In this study metallo-thermo-mechanical coupled model was developed to predict temperature, phase transformation and stress or strain through numerical code in computer software [115]. Another FEM modelling was performed for quenching of steel in water with asymmetric model. This work concentrated on the effects of eccentric geometry on the residual stress distribution when

subjected to quenching process. The FEM model was implemented in a commercial finite element analysis (FEA) software MSC.MARC<sup>®</sup> by user subroutine. This work was verified by experimental characterisation using XRD technique to measure residual stress [116]. To get accurate data in quenching modelling, to input correct values of heat transfer coefficient and heat flux as boundary condition are important. An in-house modelling software (HT-mod) was developed using combination of finite element and finite difference methods which can predict the thermal phenomena and phase transformation of quenching 4140 steel in vegetable oil medium. Most popular FEM commercial software ABAQUS was also used along with HT-mod to predict residual stress distribution for 2D model [117]. Another finite element code was developed for quenching and tempering process for J55 steel which can predict temperature history, microstructure development and residual stress concentration in steel after quenching and tempering [118]. any finite element modelling (FEM) simulation of TMT process with quenching and self-tempering stage was not found in the literature. A technical research report states that there are some modelling works carried out of thermomechanical process to produce long product by hot rolling, warm rolling [120]. In this report a description of modelling techniques of microstructure or austenite phase structure evolution, the effects of deformation on microstructures for hot rolling of steels and other alloys was presented from different individual works. The validation, applications and needs of new modelling techniques were also reported. No works mentioned about the modelling of TMT technique after hot rolling to produce high strength structural steel. Therefore, in this study a FEM model of quenching and tempering stage of TMT steel bar has been developed following the methodology developed for thermal model of LSG in previous chapters. Due to the quenching and tempering stage the TMT steel bar attain dual composite structure including hard outer case and soft inner core similar to the LSG process. The FEM model of quenching and tempering will predict the case depth of the

TMT treated structural steel cylindrical bar and will be compared with experimentally measured case depth of the TMT treated steel bar with same chemical composition and geometry. The purpose of developing the quenching and tempering model is to verify the methodology used in LSG thermal model development.

## 6.2 Methodology

### 6.2.1 Materials selection

In the structural application the high strength reinforcement bars usually made of low carbon (C) steel (0.16-0.18 %wt. of C) [112] are used for the need of high ductility and toughness. Therefore, in this model a low alloy carbon steel was considered as materials properties. The diameter and length of the steel cylinder is set to 20 mm following an experimental work done in TMT structural steel bars for the model analysis [111].

### 6.2.2 Principle of quenching and tempering model

The principle of quenching and tempering processes follows the first law of energy conservation and Fourier's heat conduction rule mentioned in Equation 6.1 [115,116]. It is a transient heat transfer process without mass transfer effect as no molten state is present.

$$\frac{\partial}{\partial x} \left( k \frac{\partial T}{\partial x} \right) + \frac{\partial}{\partial y} \left( k \frac{\partial T}{\partial y} \right) = \rho C_p \frac{\partial T}{\partial t} \quad (6.1)$$

where,  $\rho$ ,  $C_p$ , and  $k$  are the density, specific heat, thermal conductivity respectively of the material given as a function of temperature  $T$  and  $t$  is time.

The boundary conditions in the thermal analysis is the convection due to the difference in temperature in the film of quenching medium and the surface of the rolled bar written in Equation 6.2.

$$T_s = h(T_s - T_\infty) \quad (6.2)$$

here,  $T_s$ ,  $T_\infty$ , and  $h$  are respectively surface temperature, quenchant temperature, and temperature dependant heat transfer coefficient. The percentage of heat loss due to radiation from the boundary of the bar is very small. Therefore, the radiation boundary condition is ignored for this analysis. The symmetry and other surface which are not in contact with the quenchant is considered adiabatic, that means, there are no heat transfer from the boundary to the environment [121].

### 6.2.3 FEM model set-up

A 3D cylinder of 20 mm for both diameter and length was taken as geometry for the simulation of quenching and tempering process of structural steel bars using ANSYS mechanical APDL. For meshing, Solid 70, 8 node brick element has been selected as in chapter 3. Solid 70 has temperature degree of freedom (DOF) for each node and hence mathematically economic. Figure 6.2 has illustrated the cylindrical geometry and meshed model. Hexahedral element shape has been chosen for meshing. The total number of elements is 48000 which is selected from a mesh convergence study (See Appendix A2).

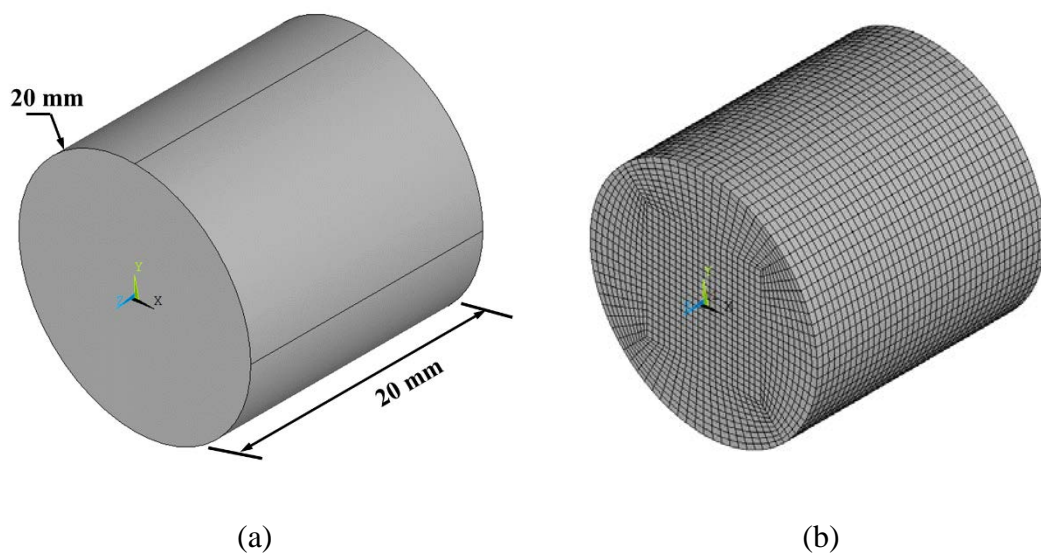


Figure 6. 2 (a) The cylindrical geometry of TMT steel bar and (b) the meshed model

The temperature dependant physical properties of structural steel and film coefficient value shown in Figure 6.2 has been applied in the model. The value of film coefficient,  $h_f$ , for convection heat transfer in water medium during quenching was calibrated through the modelling for required level of cooling rate. Usually the value of  $h_f$  for forced convection in water medium remains in the range of  $1000-15000 \text{ Wm}^{-2}\text{K}^{-1}$  [122]. In TMT process the pressure of water jet and temperature decides the appropriate value of convection film coefficient. In this case simulation process plays a vital role to decide film coefficient rather than measuring experimentally.

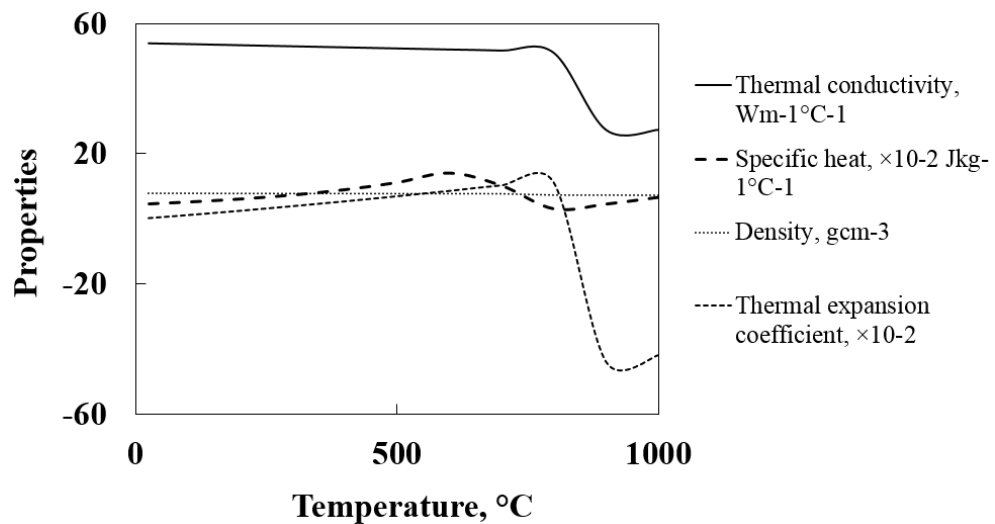


Figure 6. 3 Temperature dependant physical properties of structural steel taken from literature [123–125]

## 6.3 Results and discussion

### 6.3.1 Temperature distribution and cooling rate

The temperature isotherm of the cylinder for different time during quenching has been presented in Figure 6.3. When the rolled product crosses the last strand of rolling, in case of TMT process, the temperature of the rolled bar is kept around  $1200^\circ\text{C}$  in the austenite phase region. It is assumed here that the rolled product takes 0.1 second from last strand of roller to enter the quenching box.

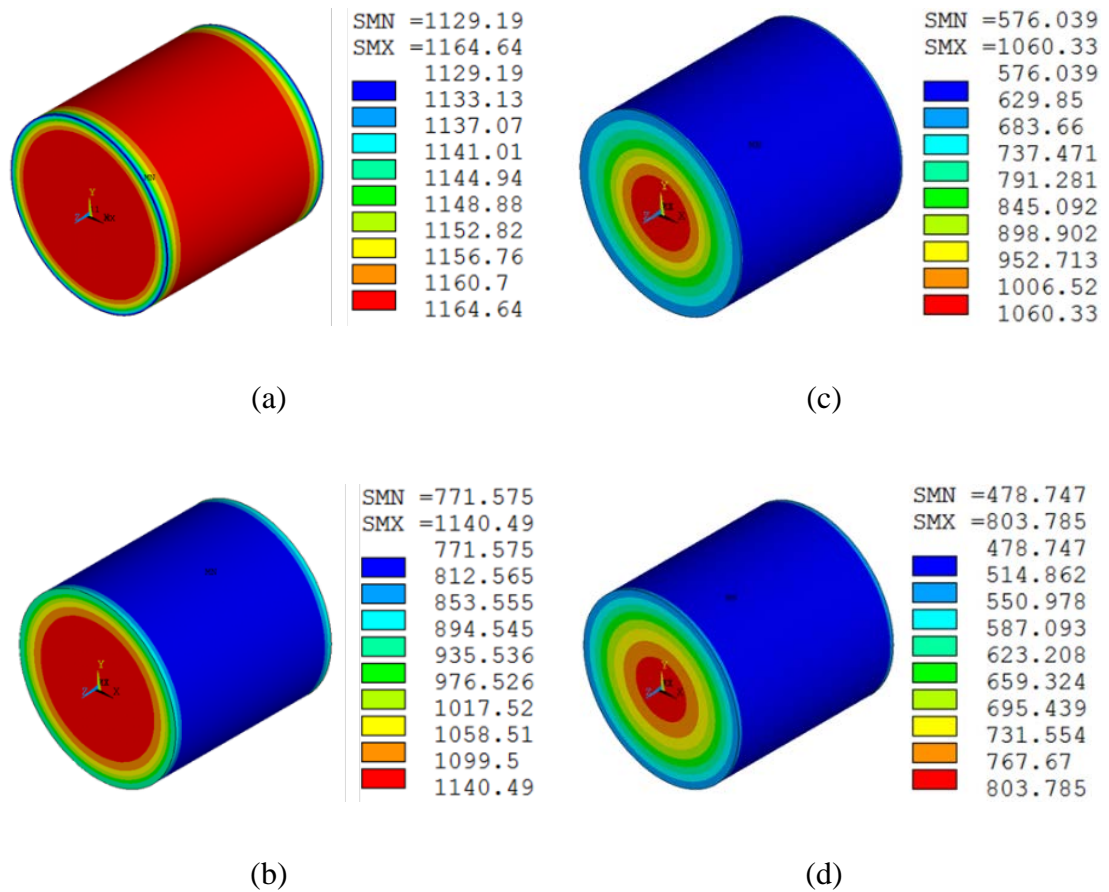
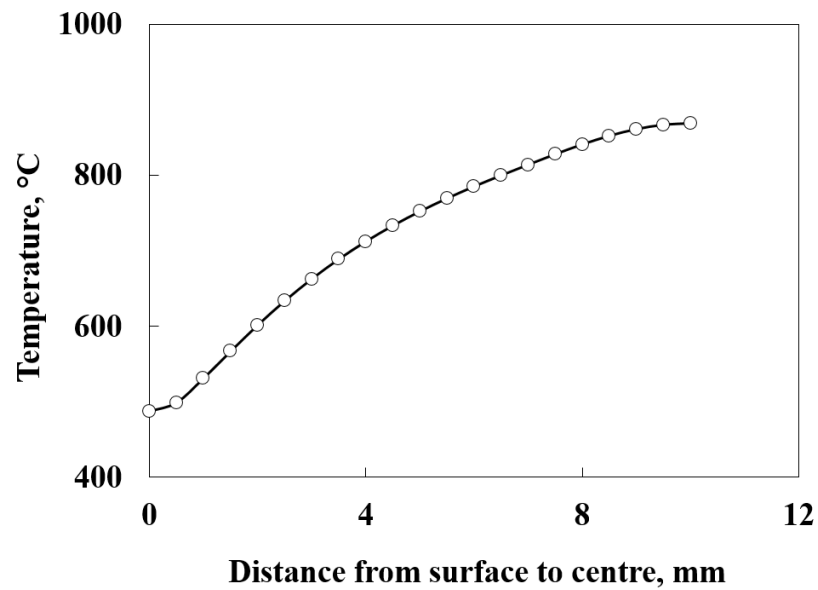


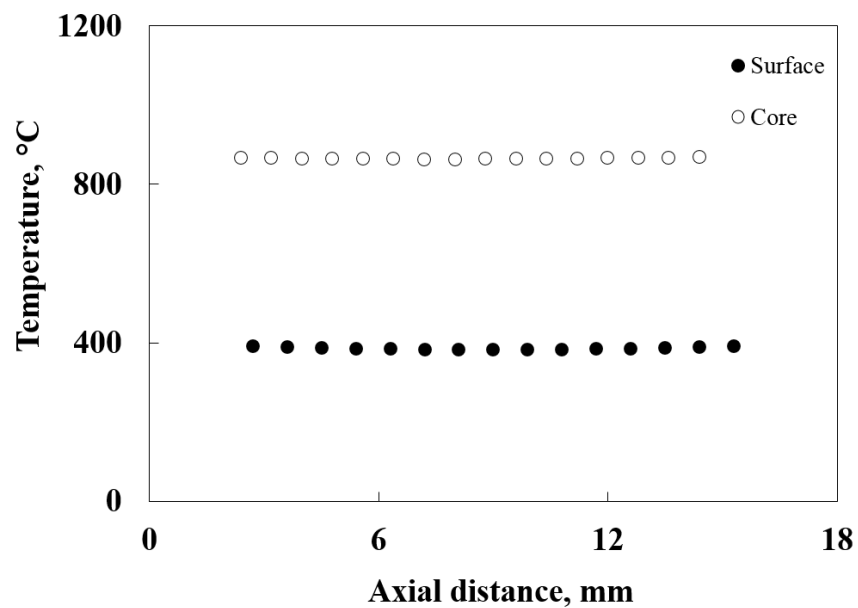
Figure 6. 4 Temperature distribution (a) just before the rolled bar subjected to quenching at 0.1 sec, (b) just after quenching starts at 0.3 sec, (c) at the middle of the quenching stage at 1.1 sec, and (d) just after the quenching finish at 2.1 sec

In Figure 6. 4a, it is observed that the temperatures of the surface and centre of the sample are same. When it enters the quenching box due to cold water flow at the high pressure the surface temperature of the bar drops within a moment. Figure 6. 4b shows that the temperature of surface drops to 771.57 °C at 0.3 seconds which is just after quenching started. The temperature inside the bar is still very high around 1140 °C at that moment. Similarly, Figure 6. 4c and Figure 6. 4d presents the temperature distribution from surface to centre of the bar at time 1.1 sec and 2.1 sec during quenching. Quenching lasts for only 2 sec in this analysis. Therefore, final temperatures of surface and centre of the bar just after the quenching are achieved respectively 478.7 °C and 803.8 °C (See

Figure 6. 4d). Thus, from the simulation results temperature distribution at different time during the quenching process can be analysed.



(a)



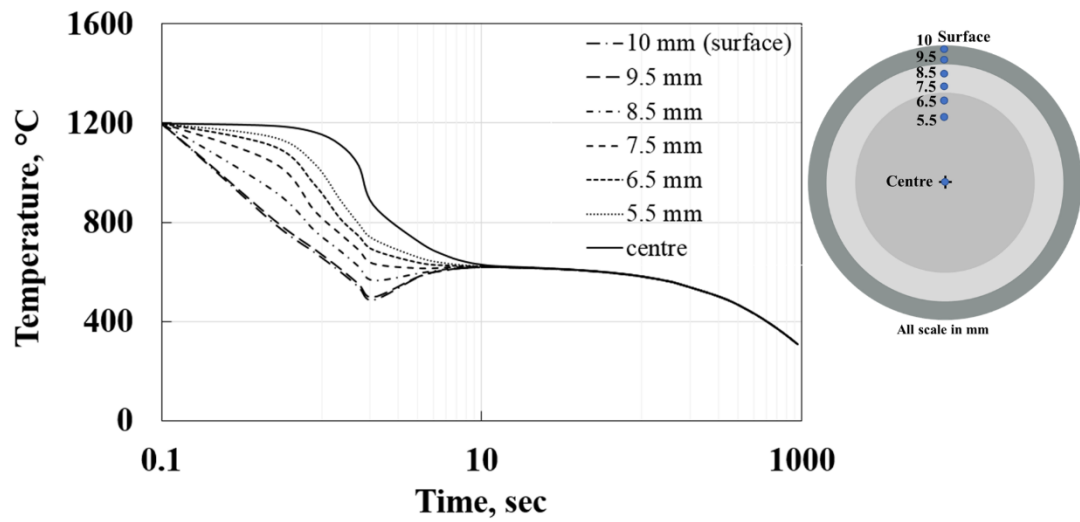
(b)

Figure 6. 5 Temperature variation along (a) radial and (b) axial distance of the bar

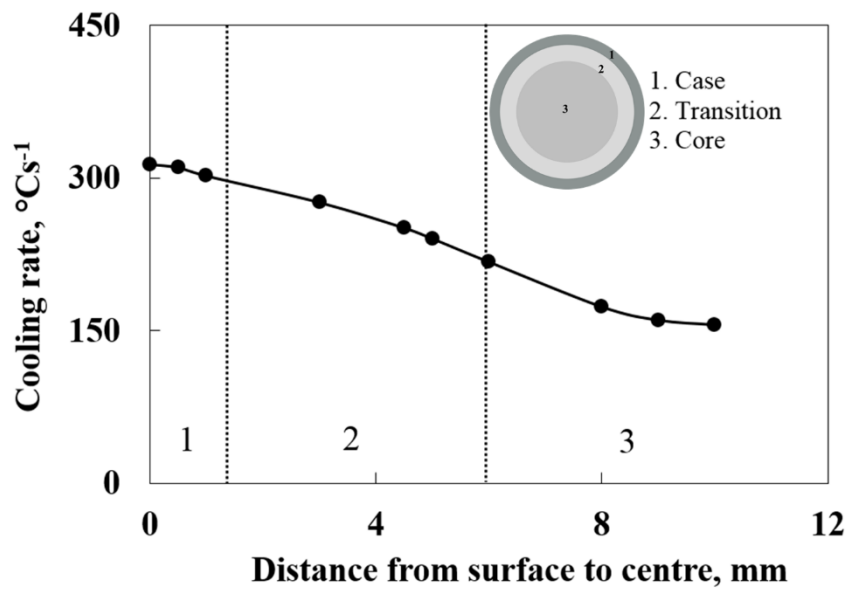
Temperature variation along the radial distance from surface to the centre and along the axial direction has been plotted in Figure 6.5. In the quenching stage the temperature has

varied from the surface to centre along the radial distance of the bar (Figure 6. 5a). The minimum temperature at surface after quenching is  $483^{\circ}\text{C}$  at 2.1 sec and at same time the core temperature remains around  $878^{\circ}\text{C}$ . However, temperatures of surface and core have remained equal along the axis shown Figure 6. 5b. The uniform temperature distribution of surface along the length is important to ensure during the practical process to maintain uniform properties.

Figure 6. 6 shows time-temperature plots at different depths from surface to centre. The surface temperature drops quite rapidly when the quenching starts until the minimum temperature is achieved. Whereas the core of the bar cools slowly for almost entire quenching period and remains quite higher than the surface until it finishes. Therefore, a good temperature difference prevails between the core and the surface of the bar after quenching. Due to the temperature difference between core and surface, the cold surface is heated up again by the heat conducted from hot core. This is called the self-tempering stage of bar without any external heating source. This step is over when both surface and core achieve an equal temperature which is called equalization temperature. In this study, equalization temperature is achieved at around  $600^{\circ}\text{C}$  where the quenched surface gets tempered. After that whole bar cools slowly to room temperature. Cooling rates have been calculated from the time-temperature plot. Figure 6. 6b shows cooling rates varied from surface to centre. The mean surface cooling rate is attained around  $300^{\circ}\text{C}\text{s}^{-1}$ . This rate has been gradually decreased and become almost half at core, 10 mm distance from surface.



(a)



(b)

Figure 6. 6 (a) Time-temperature plot at different depth and (b) mean cooling rate

variation from surface to centre

### 6.3.2 Case and core depth

The three distinct zones attained from the quenching and tempering model have been depicted in Figure 6.7. The schematic diagram of the quenched and tempered steel bar with hard case, transition zone and soft core has been presented. The case depth and transition zone have been estimated 1.5 mm and 2 mm approximately based on differential cooling rates mentioned in Figure 6. 6b. A previously done experimental work characterised the case depth of 2 mm shown in Figure 6.7b. The variation in case depth between modelling and experimental bar is due to the difference in film coefficient, quenching time and last pass temperature

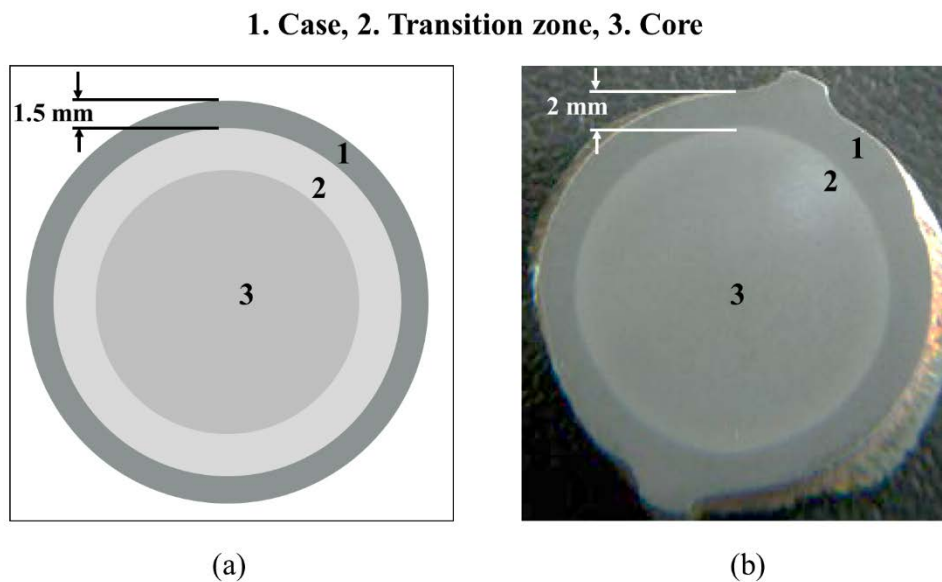


Figure 6. 7 (a) schematic of the composite structure predicted from simulation and (b) experiments from literature revealed three different zones 1. Case, 2. Core, and 3.

Transition

### 6.4 Summary

A successful attempt has been taken to simulate quenching and tempering of TMT process for structural steel applying the LSG thermal modelling method. Three different zones respectively case, core and transition have been identified from this model. This model

can predict the case depth, temperature distribution and cooling rates for different zones. Simulation results showed that the hard case occupies 19% of the total surface area of the TMT bar and so that of 81% for the soft core including transition zone. The cooling rates in case is higher than the core. Therefore, the possible martensitic structure is present in outer case which turned into tempered martensite at tempering stage around 600°C. The case depth has been calculated from the model is 1.5 mm which is nearly equal to the experimentally measured case depth of the TMT treated steel sample with same chemical composition and geometry. From this study it can be concluded that FEM of quenching and tempering stage of TMT process is an effective way to optimise the process prior to the implementation for different materials and parameters. Thus, it can also be realised the FEM methodology used to develop thermal model of LSG can be successfully applied in similar heat treatment modelling.

-----X-----

# Chapter 7

## Conclusions and future recommendation

### 7.1 Thermal modelling of LSG

- Both 2D and 3D thermal model of LSG for H13 tool steel with cylindrical geometry has been successfully developed in ANSYS mechanical APDL FEM software.
- The model predicted temperature distribution, heating, cooling rates and depth of the modified zone for 200 W and 300 W laser power, 0.2 mm beam width and 0.15 ms residence time for H13 tool steel.
- Around 4% variation in peak surface temperature for 2D and 3D thermal model was observed, which is negligible. Predicted peak temperature from the numerical model showed well-agreement with analytical analysis.
- The peak surface temperature, heating, cooling rates and depth of modified zone increased with increasing laser power.
- In 3D model of H13 tool steel the peak temperature was 1597 K for 200 W which increases to 2532 K for 300 W. Similarly, the heating and cooling rates were  $8.7 \times 10^6 \text{ Ks}^{-1}$  and  $3.4 \times 10^6 \text{ Ks}^{-1}$  for 200 W laser power and the value has increased to  $1.6 \times 10^7 \text{ Ks}^{-1}$  and  $6.5 \times 10^6 \text{ Ks}^{-1}$  respectively for 300 W due to the increase of temperature gradient. The depth of modified zone also showed proportional relationship with laser power. For 200 W laser power the depth was 30  $\mu\text{m}$  which increases to 37.5  $\mu\text{m}$  at 300 W predicted from 3D model.
- Predicted temperature along the distance from surface to centre of the semi-infinite cylindrical model was well-agreed with the calculated temperature from the explicit solution of transient heat transfer for 200 W laser power, 0.2 mm beam width and

0.15 ms residence time. Although the explicit solution did not show variation in temperature beyond certain depth (around 60  $\mu\text{m}$ ) from the surface regardless laser power and residence time. Therefore, numerical thermal model is effective and reliable tool in predicting temperature distribution for LSG process for different laser parameters.

## **7.2 Parametric study of 3D LSG thermal model**

- Parametric study of 3D half-cylindrical thermal model has been carried out for H13 tool steel and Ti6Al4V by varying laser power. Two power range from 200 W to 240 W and from 100 W to 140 W have been selected for H13 tool steel and Ti6Al4V alloy to find out the threshold laser power required to occur melting in LSG by considering uniform heat source of CO<sub>2</sub> laser at 0.2 mm beam width and 0.15 ms residence time. Study showed that 210 W and 130 W are required to initiate melting for H13 tool steel and Ti6Al4V alloy respectively which well-agreed with literature.
- The developed thermal model has potential use in industry to optimise laser power for operating LSG process with different materials by utilising appropriate materials properties.
- The effect of Gaussian distributed heat source as surface and volumetric load has been studied for 3D thermal modelling of LSG. Results showed that volumetric heat load required higher laser power to initiate melting than surface heat load because of the penetration of laser beam.

## **7.3 Thermomechanical modelling of LSG**

- A 2D thermomechanical coupled model of LSG have been successfully developed to predict residual stress.

- The model has been conducted with H13 tool steel at 200 W and 300 W laser power with 0.2 mm beam width and 0.15 ms residence time for two different rate-independent plasticity theories, isotropic and kinematic in plane stress condition.
- During heating surface experiences compressive stress which has turned in to tensile stress after cooling. Both compressive and tensile stresses increased with laser power increment.
- At peak temperature surface experienced compressive stress which turned into tensile below the surface. After cooling the surface stress became tensile and the sub-surface area experienced compressive.
- The isotropic model gave higher values of the stress than the kinematic model.
- Surface tensile stress was significantly greater for isotropic model than for kinematic model at higher power level.
- The von Mises equivalent stress attained 1600 MPa at 250 W laser power for isotropic model which is higher than the yield strength of H13 tool steel. For kinematic model the maximum value is 800 MPa and this is below the yield strength.

#### **7.4 Application of LSG thermal model in quenching and tempering**

- The thermal model of LSG has been successfully utilised to simulate quenching and tempering for structural steel having 20 mm diameter and length. The model predicted temperature distribution, cooling rates and depth of hardened case.
- The model predicted the 1.5 mm case depth for 1200°C initial temperature, 2 s quenching time which agrees with previous experimental work. The hardened case occupied 19% of the cross-sectional area of the steel bar and 81% was left including core and transition zone.

- The cooling rate for the case was predicted  $300^{\circ}\text{C}\text{s}^{-1}$  which indicated the formation of martensite due to quenching. This martensite is transformed into tempered martensite at  $600^{\circ}\text{C}$  equalisation temperature achieved.

### 7.5 Future recommendations

- The 3D LSG thermal model has been developed for stationary laser beam while in real process laser scans over the surface with certain velocity of the treated sample. Therefore, the 3D thermal model could be further developed with moving heat source.
- The convection and radiation boundary conditions have been ignored in the present single step thermal model of LSG because of their insignificant contribution in the heat transfer process. However, in the moving heat source model convection plays a role in heat transfer at the direction of scanning laser due to advection. Therefore, both convection and radiation will be considered in 3D moving heat source model.
- The laser absorptivity will vary with temperature and absorptivity increases at molten state. Hence, a variable absorptivity with temperature will be considered in future.
- The melt pool thermodynamic will be introduced to understand the effect of Marangoni convection in the depth of melt pool created by LSG.
- Laser power has been optimised for this developed thermal model of LSG for H13 tool steel and Ti6Al4V alloy. More parametric study to optimise other important parameters including residence time, beam width and scanning speed will be conducted with additional materials.
- Quantitative microstructure modelling for phase transformation during the LSG process will be added by following phase kinetics such as, Johnson-Mehl-Avrami equation.

- 3D thermal model of Ti6Al4V alloy has considered latent heat of fusion by adjusting specific heat value from the literature to consider phase change. The latent heat of fusion has significant contribution in temperature distribution. Therefore, to increase accuracy of the model more understanding in enthalpy method to simulate phase change in LSG will be required including mass flow during the transition.
- A 3D thermomechanical model could be developed from the 2D model to increase accuracy in predicting residual stress. The effects of inelastic strain on the residual stress will be explored in more details.
- An experimental study of LSG for H13 tool steel or Ti6Al4V alloy to measure surface temperature using thermocouple and high-speed camera will be carried out and experimental results will be used to validate the thermal model of LSG.
- Material properties are important input in LSG modelling which ensures the prediction accuracy. However, appropriated and consistent temperature dependent material properties database is insufficient in the literature for ferrous and non-ferrous materials. Robust and simple experimental research is important to measure temperature dependent physical and mechanical material properties.
- Finally, appropriate method of surface hardness prediction will be explored and implemented in the LSG modelling.

-----X-----

## References

1. Breinan, E. M.; Kear, B. H.; Banas, C. M. Processing materials with lasers. *Phys. Today* **1976**, *29*, 44–50, doi:10.1063/1.3024504.
2. Kear, B. H.; Breinan, E. M.; Greenwald, L. E. Laser glazing - a new process for production and control of rapidly chilled metallurgical microstructures. *Met. Technol.* **1979**, *April*, 121–129.
3. Aqida, S. N. Laser surface modification of steel, PhD thesis, Dublin City University, Dublin, Ireland, 2011.
4. Aldajah, S. H.; Ajayi, O. O.; Fenske, G. R. Laser glazing process development and optimization for railroad applications. *Proc. STLE/ASME Int. Jt. Tribol. Conf. IJTC 2006* **2006**, *2006*, 1–27.
5. Chikarakara, E.; Naher, S.; Brabazon, D. High speed laser surface modification of Ti-6Al-4V. *Surf. Coatings Technol.* **2012**, *206*, 3223–3229, doi:10.1016/j.surfcoat.2012.01.010.
6. Desforges, C. D. Laser heat treatment. *Tribol. Int.* **1978**, *April*, 139–143.
7. Taylor, D. *New Scientist*. March 1977, 647.
8. Kear, B. H.; Breinan, E. M.; Thompson, E. R. Laser processing of materials. In *Advances in Metal Processing*; Burke, J. J., Ed.; Plenum Press, New York, **1981**; 45–78.
9. Aqida, S. N.; Naher, S.; Maurel, M.; Brabazon, D. An overview of laser surface modification of die steels. In *25<sup>th</sup> International Manufacturing Conference Proceedings, Dublin Institute of Technology*; Dublin, Ireland, **2008**; 120–128.
10. Muhič, M.; Tušek, J.; Kosel, F.; Klobčar, D.; Muhi, M.; Tušek, J.; Kosel, F. and; Klob, D. Analysis of die casting tool material. *Stroj. Vestnik/Journal Mech. Eng.* **2010**, *56*, 351–356.
11. Jiang, W.; Molian, P. Nanocrystalline TiC powder alloying and glazing of H13 steel using a CO<sub>2</sub> laser for improved life of die-casting dies. *Surf. Coatings Technol.* **2001**, *135*, 139–149, doi:10.1016/S0257-8972(00)01075-6.
12. Fribourg, G.; Deschamps, A.; Bréchet, Y.; Mylonas, G.; Labeas, G.; Heckenberger, U.; Perez, M. Microstructure modifications induced by a laser surface treatment in an AA7449 aluminium alloy. *Mater. Sci. Eng. A* **2011**, *528*, 2736–2747, doi:10.1016/j.msea.2010.12.018.
13. Cai, H.; Zhang, Y.; Liu, Z. Motion analysis of cam with laser quenching heat treatment. *Laser Technol.* **2010**, *34*, 812–815.
14. Cole, G. S.; McCune Jr, R. C. Composite disk brake rotor and method of making.
15. Chikarakara, E. Laser surface modifications of biomedical alloys, PhD thesis, Dublin City University, Dublin, Ireland, 2012.
16. Piekarska, W.; Kubiak, M.; Saternus, Z. Numerical simulation of deformations in T-joint welded by the laser beam. *Arch. Metall. Mater.* **2013**, *58*, 1391–1396, doi:10.2478/amm-2013-0181.
17. Kong, F.; Kovacevic, R. 3D finite element modeling of the thermally induced residual stress in the hybrid laser/arc welding of lap joint. *J. Mater. Process.*

- Technol.* **2010**, 210, 941–950, doi:10.1016/j.jmatprotec.2010.02.006.
18. Tölle, F.; Gumenyuk, A.; Backhaus, A.; Olschok, S.; Rethmeier, M.; Reisinger, U. Welding residual stress reduction by scanning of a defocused beam. *J. Mater. Process. Technol.* **2012**, 212, 19–26, doi:10.1016/j.jmatprotec.2011.07.019.
  19. Hao, M.; Sun, Y. A FEM model for simulating temperature field in coaxial laser cladding of Ti6Al4V alloy using an inverse modeling approach. *Int. J. Heat Mass Transf.* **2013**, 64, 352–360, doi:10.1016/j.ijheatmasstransfer.2013.04.050.
  20. Hofman, J. T.; De Lange, D. F.; Pathiraj, B.; Meijer, J. FEM modeling and experimental verification for dilution control in laser cladding. *J. Mater. Process. Technol.* **2011**, 211, 187–196, doi:10.1016/j.jmatprotec.2010.09.007.
  21. Tobar, M. J.; Álvarez, C.; Amado, J. M.; Ramil, A.; Saavedra, E. and; Yáñez, A. Laser transformation hardening of a tool steel: Simulation-based parameter optimization and experimental results. *Surf. Coatings Technol.* **2006**, 200, 6362–6367, doi:10.1016/j.surfcoat.2005.11.067.
  22. Yáñez, A.; Álvarez, J. C.; López, A. J.; Nicolás, G.; Pérez, J. A.; Ramil, A.; Saavedra, E. Modelling of temperature evolution on metals during laser hardening process. *Appl. Surf. Sci.* **2002**, 186, 611–616, doi:10.1016/S0169-4332(01)00696-1.
  23. Akbari, M.; Saedodin, S.; Toghraie, D.; Shoja-Razavi, R.; Kowsari, F. Experimental and numerical investigation of temperature distribution and melt pool geometry during pulsed laser welding of Ti6Al4V alloy. *Opt. Laser Technol.* **2014**, 59, 52–59, doi:10.1016/j.optlastec.2013.12.009.
  24. Chehrghani, A.; Torkamany, M. J.; Hamed, M. J.; Sabbaghzadeh, J. Numerical modeling and experimental investigation of TiC formation on titanium surface pre-coated by graphite under pulsed laser irradiation. *Appl. Surf. Sci.* **2012**, 258, 2068–2076, doi:10.1016/j.apsusc.2011.04.064.
  25. Farahmand, P.; Kovacevic, R. An experimental–numerical investigation of heat distribution and stress field in single- and multi-track laser cladding by a high-power direct diode laser. *Opt. Laser Technol.* **2014**, 63, 154–168, doi:10.1016/j.optlastec.2014.04.016.
  26. Azizpour, M.; Ghoreishi, M.; Khorram, A. Numerical simulation of laser beam welding of Ti6Al4V sheet. *J. Comput. Appl. Res. Mech. Eng.* **2015**, 4, 145–154.
  27. Mahank, T. A. Laser glazing of metals and metallic and ceramic coatings, PhD thesis, Pennsylvania State University, Pennsylvania, United states 2010.
  28. Aqida, S. N.; Naher, S.; Brabazon, D. Thermal simulation of laser surface modification of H13 die steel. *Key Eng. Mater.* **2012**, 504–506, 351–356, doi:10.4028/www.scientific.net/KEM.504-506.351.
  29. Peligrad, A.; Zhou, E.; Morton, D. and; Li, L. A melt depth prediction model for quality control of laser surface glazing of inhomogeneous materials. *Opt. Laser Technol.* **2001**, 33, 7–13, doi:10.1016/S0030-3992(00)00107-9.
  30. Hao, L.; Lawrence, J. Melt depth prediction for laser irradiated magnesia partially stabilised zirconia. *J. Mater. Process. Technol.* **2006**, 180, 110–116, doi:10.1016/j.jmatprotec.2006.05.009.
  31. Li, J. F.; Li, L.; Stott, F. H. Comparison of volumetric and surface heating sources in the modeling of laser melting of ceramic materials. *Int. J. Heat Mass Transf.* **2004**, 47, 1159–1174, doi:10.1016/j.ijheatmasstransfer.2003.10.002.

32. Deng, D.; Kiyoshima, S. Numerical simulation of residual stresses induced by laser beam welding in a SUS316 stainless steel pipe with considering initial residual stress influences. *Nucl. Eng. Des.* **2010**, *240*, 688–696, doi:10.1016/j.nucengdes.2009.11.049.
33. Han, Q.; Kim, D.; Kim, D.; Lee, H.; Kim, N. Laser pulsed welding in thin sheets of Zircaloy-4. *J. Mater. Process. Technol.* **2012**, *212*, 1116–1122, doi:10.1016/j.jmatprotec.2011.12.022.
34. Tirand, G.; Arvieu, C.; Lacoste, E.; Quenisset, J. M. Control of aluminium laser welding conditions with the help of numerical modelling. *J. Mater. Process. Technol.* **2013**, *213*, 337–348, doi:10.1016/j.jmatprotec.2012.10.014.
35. Bendaoud, I.; Mattei, S.; Cicala, E.; Tomashchuk, I.; Andrzejewski, H.; Sallamand, P.; Mathieu, A.; Bouchaud, F. The numerical simulation of heat transfer during a hybrid laser–MIG welding using equivalent heat source approach. *Opt. Laser Technol.* **2014**, *56*, 334–342, doi:10.1016/j.optlastec.2013.09.007.
36. Kumar, C.; Das, M.; Biswas, P. A 3-D finite element analysis of transient temperature profile of laser welded Ti-6Al-4V alloy. In *5th interantional and 26th all India manufacturing technology, design and research conference*; Guwahati, India, 2014; 1–6.
37. Han, Q.; Kim, D.; Kim, D.; Lee, H.; Kim, N. Laser pulsed welding in thin sheets of Zircaloy-4. *J. Mater. Process. Technol.* **2012**, *212*, 1116–1122, doi:10.1016/j.jmatprotec.2011.12.022.
38. Piekarska, W.; Kubiak, M. Modeling of thermal phenomena in single laser beam and laser-arc hybrid welding processes using projection method. *Appl. Math. Model.* **2013**, *37*, 2051–2062, doi:10.1016/j.apm.2012.04.052.
39. Kumar, S.; Awasthi, R.; Viswanadham, C. S.; Bhanumurthy, K.; Dey, G. K. Thermo-metallurgical and thermo-mechanical computations for laser welded joint in 9Cr-1Mo(V, Nb) ferritic/martensitic steel. *Mater. Des.* **2014**, *59*, 211–220, doi:10.1016/j.matdes.2014.02.046.
40. Santhanakrishnan, S.; Kong, F.; Kovacevic, R. An experimentally based thermo-kinetic hardening model for high power direct diode laser cladding. *J. Mater. Process. Technol.* **2011**, *211*, 1247–1259, doi:10.1016/j.jmatprotec.2011.02.006.
41. Farahmand, P.; Balu, P.; Kong, F.; Kovacevic, R. Investigation of thermal cycle and hardness distribution in the Laser Cladding of AISI H13 Tool Steel produced by a High Power Direct Diode Laser. In *ASME 2013 International Mechanical Engineering Congress and Exposition*; San Diego, California, USA, 2015; 1–12.
42. Louvis, E.; Fox, P.; Sutcliffe, C. J. Selective laser melting of aluminium components. *J. Mater. Process. Technol.* **2011**, *211*, 275–284, doi:10.1016/j.jmatprotec.2010.09.019.
43. Song, B.; Dong, S.; Liao, H.; Coddet, C. Process parameter selection for selective laser melting of Ti6Al4V based on temperature distribution simulation and experimental sintering. *Int. J. Adv. Manuf. Technol.* **2012**, *61*, 967–974, doi:10.1007/s00170-011-3776-6.
44. Sallica-Leva, E.; Jardini, A. L.; Fogagnolo, J. B. Microstructure and mechanical behavior of porous Ti-6Al-4V parts obtained by selective laser melting. *J. Mech. Behav. Biomed. Mater.* **2013**, *26*, 98–108, doi:10.1016/j.jmbbm.2013.05.011.
45. Prashanth, K. G.; Scudino, S.; Klauss, H. J.; Surreddi, K. B.; Löber, L.; Wang, Z.; Chaubey, A. K.; Kühn, U.; Eckert, J. Microstructure and mechanical properties of

- Al-12Si produced by selective laser melting: Effect of heat treatment. *Mater. Sci. Eng. A* **2014**, 590, 153–160, doi:10.1016/j.msea.2013.10.023.
46. Dai, D.; Gu, D. Thermal behavior and densification mechanism during selective laser melting of copper matrix composites: Simulation and experiments. *Mater. Des.* **2014**, 55, 482–491, doi:10.1016/j.matdes.2013.10.006.
  47. Bertelli, F.; Meza, E. S.; Goulart, P. R.; Cheung, N.; Riva, R.; Garcia, A. Laser remelting of Al1.5 wt%Fe alloy surfaces: Numerical and experimental analyses. *Opt. Lasers Eng.* **2011**, 49, 490–497, doi:10.1016/j.optlaseng.2011.01.007.
  48. Telasang, G.; Dutta Majumdar, J.; Padmanabham, G.; Tak, M.; Manna, I. Effect of laser parameters on microstructure and hardness of laser clad and tempered AISI H13 tool steel. *Surf. Coatings Technol.* **2014**, 258, 1108–1118, doi:10.1016/j.surfcoat.2014.07.023.
  49. Telasang, G.; Dutta Majumdar, J.; Padmanabham, G.; Manna, I. Structure-property correlation in laser surface treated AISI H13 tool steel for improved mechanical properties. *Mater. Sci. Eng. A* **2014**, 599, 255–267, doi:10.1016/j.msea.2014.01.083.
  50. Suárez, A.; Tobar, M. J.; Yáñez, A.; Perez, I.; Sampedro, J.; Amigo, V.; Candel, J. J. Modeling of phase transformations of Ti6Al4V during laser metal deposition. *Phys. Procedia* **2011**, 12, 666–673, doi:10.1016/j.phpro.2011.03.083.
  51. Roberts, I. A. Investigation of residual stresses in the Laser Melting of metal powders in additive layer, PhD thesis, University of Wolverhampton, UK, 2012.
  52. Yilbas, B. S.; Akhtar, S. S.; Karatas, C.; Ali, H.; Boran, K.; Khaled, M.; Al-Aqeeli, N.; Aleem, A. B. J. Laser treatment of aluminum composite and investigation of thermal stress field. *Int. J. Adv. Manuf. Technol.* **2016**, 86, 3547–3561, doi:10.1007/s00170-015-8202-z.
  53. Suárez, A.; Amado, J. M.; Tobar, M. J.; Yáñez, A.; Fraga, E.; Peel, M. J. Study of residual stresses generated inside laser clad plates using FEM and diffraction of synchrotron radiation. *Surf. Coatings Technol.* **2010**, 204, 1983–1988, doi:10.1016/j.surfcoat.2009.11.037.
  54. Paul, S.; Ashraf, K.; Singh, R. Residual stress modeling of powder injection laser surface cladding for die repair applications. In *ASME 2014 International Manufacturing Science and Engineering Conference, MSEC 2014 Collocated with the JSME 2014 International Conference on Materials and Processing and the 42nd North American Manufacturing Research Conference*; 2014; Vol. 2, 1–8.
  55. Li, C.; Wang, Y.; Zhan, H.; Han, T.; Han, B.; Zhao, W. Three-dimensional finite element analysis of temperatures and stresses in wide-band laser surface melting processing. *Mater. Des.* **2010**, 31, 3366–3373, doi:10.1016/j.matdes.2010.01.054.
  56. Wang, L.; Felicelli, S. D.; Pratt, P. Residual stresses in LENS-deposited AISI 410 stainless steel plates. *Mater. Sci. Eng. A* **2008**, 496, 234–241, doi:10.1016/j.msea.2008.05.044.
  57. Talukdar, T. K.; Wang, L.; Felicelli, S. D. Simulation of residual stress in LENS deposited H13 tool steel on copper substrate. In *ASME 2011 International Mechanical Engineering Congress and Exposition*; Denver, Colorado, USA; 1–9.
  58. Li, C.; Wang, Y.; Zhang, Z.; Han, B.; Han, T. Influence of overlapping ratio on hardness and residual stress distributions in multi-track laser surface melting roller steel. *Opt. Lasers Eng.* **2010**, 48, 1224–1230, doi:10.1016/j.optlaseng.2010.06.010.

59. Réti, T.; Gergely, M.; Tardy, P. Mathematical treatment of non-isothermal transformations. *Mater. Sci. Technol.* **1987**, *3*, 365–371, doi:10.1179/026708387790122611.
60. Yadroitsev, I.; Krakhmalev, P.; Yadroitsava, I. Selective laser melting of Ti6Al4V alloy for biomedical applications: Temperature monitoring and microstructural evolution. *J. Alloys Compd.* **2014**, *583*, 404–409, doi:10.1016/j.jallcom.2013.08.183.
61. Yilbas, B. S.; Sami, M.; AbuAlHamayel, H. I. 3-dimensional modeling of laser repetitive pulse heating: a phase change and a moving heat source considerations. *Appl. Surf. Sci.* **1998**, *134*, 159–178, doi:10.1016/S0169-4332(98)00205-0.
62. El Cheikh, H.; Courant, B.; Hascoët, J. Y.; Guillén, R. Prediction and analytical description of the single laser track geometry in direct laser fabrication from process parameters and energy balance reasoning. *J. Mater. Process. Technol.* **2012**, *212*, 1832–1839, doi:10.1016/j.jmatprotec.2012.03.016.
63. Verhaeghe, F.; Craeghs, T.; Heulens, J.; Pandelaers, L. A pragmatic model for selective laser melting with evaporation. *Acta Mater.* **2009**, *57*, 6006–6012, doi:10.1016/j.actamat.2009.08.027.
64. Laazizi, A.; Courant, B.; Jacquemin, F.; Andrzejewski, H. Applied multi-pulsed laser in surface treatment and numerical-experimental analysis. *Opt. Laser Technol.* **2011**, *43*, 1257–1263, doi:10.1016/j.optlastec.2011.03.019.
65. Goldak, J.; Chakravarti, A.; Bibby, M. A new finite element model for welding heat sources. *Metall. Trans. B* **1984**, *15*, 299–305.
66. Cottam, R.; Brandt, M. Development of a processing window for the transformation hardening of Nickel-Aluminium-Bronze. **2010**, 654-656, 1916–1919, doi:10.4028/www.scientific.net/MSF.654-656.1916.
67. Lei, Y.; Sun, R.; Tang, Y.; Niu, W. Numerical simulation of temperature distribution and TiC growth kinetics for high power laser clad TiC/NiCrBSiC composite coatings. *Opt. Laser Technol.* **2012**, *44*, 1141–1147, doi:10.1016/j.optlastec.2011.09.030.
68. Vollertsen, F.; Partes, K.; Meijer, J. State of the art of Laser Hardening and Cladding. In *the Third International WLT-Conference on Lasers in Manufacturing*; 2005; 1–25.
69. Kaplan, A. F. H. Laser absorptivity on wavy molten metal surfaces: Categorization of different metals and wavelengths. *J. Laser Appl.* **2014**, *26*, 012007(1-9), doi:10.2351/1.4833936.
70. Schneider, M.; Berthe, L.; Fabbro, R.; Muller, M. Measurement of laser absorptivity for operating parameters characteristic of laser drilling regime. *J. Phys. D. Appl. Phys.* **2008**, *41*, 6, doi:10.1088/0022-3727/41/15/155502.
71. Naeem, M. Laser processing of reflective materials. *Laser Tech. J.* **2013**, *10*, 18–20, doi:10.1002/latj.201390001.
72. Yang, J.; Sun, S.; Brandt, M.; Yan, W. Experimental investigation and 3D finite element prediction of the heat affected zone during laser assisted machining of Ti6Al4V alloy. *J. Mater. Process. Technol.* **2010**, *210*, 2215–2222, doi:10.1016/j.jmatprotec.2010.08.007.
73. Boley, C. D.; Mitchell, S. C.; Rubenchik, A. M.; Wu, S. S. Q. Metal powder absorptivity: modeling and experiment. *Appl. Opt.* **2016**, *55*, 6496, doi:10.1364/AO.55.006496.

74. Lawrence, J.; Johnston, E. P.; Li, L. Determination of absorption length of CO<sub>2</sub> and high-power diode laser radiation for ordinary Portland cement. *J. Phys. D. Appl. Phys.* **2000**, *33*, 945–947, doi:10.1088/0022-3727/33/8/310.
75. Wang, S.; Singh, R.; Yan, W. Thermo-mechanical modelling of laser cladding of CPM9V on H13 tool steel. In *5th interantional and 26th all India manufacturing technology, design and research conference*; Guwahati, Assam, India, 2014; 10–16.
76. Grellier, A.; Siaux, M. A new hot work tool steel for high temperature and high stress service conditions. In *6th international tooling conference*; Bergström, J., Ed.; Karlstad University: Sweden, 2002; 39–48.
77. Brabazon, D.; Naher, S.; Biggs, P. Glazing of tool dies for semi-solid steel forming. *Int. J. Mater. Form.* **2008**, *Supplement*, 985–988, doi:10.1007/s12289-008-0223-9.
78. Burakowski, T.; Wierzchon, T. *Surface engineering of metals: Principle, equipment, technologies*; CRC Press, 1998; ISBN 9780849382253.
79. Antony, K.; Arivazhagan, N.; Senthilkumaran, K. Numerical and experimental investigations on laser melting of stainless steel 316L metal powders. *J. Manuf. Process.* **2014**, *16*, 345–355, doi:10.1016/j.jmapro.2014.04.001.
80. Liaqat, A.; Safdar, S.; Sheikh, M. A. Finite-element modelling of thermo-mechanical stress distribution in laser beam ceramic tile grout sealing process. *Proc. Inst. Mech. Eng. Part C J. Mech. Eng. Sci.* **2006**, *220*, 1497–1508, doi:10.1243/0954406JMES143.
81. Mughal, M. P.; Fawad, H.; Mufti, R. Finite element prediction of thermal stresses and deformations in layered manufacturing of metallic parts. *Acta Mech.* **2006**, *183*, 61–79, doi:10.1007/s00707-006-0329-4.
82. Wang, L.; Wang, Y.; Sun, X. G.; He, J. Q.; Pan, Z. Y.; Zhou, Y.; Wu, P. L. Influence of pores on the thermal insulation behavior of thermal barrier coatings prepared by atmospheric plasma spray. *Mater. Des.* **2011**, *32*, 36–47, doi:10.1016/j.matdes.2010.06.040.
83. Tracy, C. D. Fire endurance of multicellular panels in an FRP building system, DSc thesis, École Polytechnique Fédérale de Lausanne, Lausanne, Switzerland, 2005.
84. Issa, A.; Brabazon, D.; Hashmi, M. S. J. 3D transient thermal modelling of laser microchannel fabrication in lime-soda glass. *J. Mater. Process. Technol.* **2008**, *207*, 307–314, doi:10.1016/j.jmatprotec.2008.06.056.
85. Zekovic, S.; Dwivedi, R.; Kovacevic, R. Thermo-structural finite element Analysis of direct laser metal deposited thin-walled structures. In *Solid Freeform Fabrication Symposium*; Austin, Texas, USA, 2005; 338–355.
86. Incropera, F. P.; Dewitt, D. P. *Fundamentals of heat and mass transfer*; 7th ed.; John Wiley and Sons, 2011;
87. Kabir, I. R.; Yin, D.; Naher, S. 3D thermal model of laser surface glazing for H13 tool steel. *AIP Conf. Proc.* **2017**, *1896*, 130003(1-6), doi:10.1063/1.5008152.
88. Kabir, I. R.; Yin, D.; Tamanna, N.; Naher, S. Thermomechanical modelling of laser surface glazing for H13 tool steel. *Appl. Phys. A Mater. Sci. Process.* **2018**, *124*, 1–9.
89. Li, C.; Wang, Y.; Han, B. Microstructure, hardness and stress in melted zone of

- 42CrMo steel by wide-band laser surface melting. *Opt. Lasers Eng.* **2011**, *49*, 530–535, doi:10.1016/j.optlaseng.2010.12.008.
90. Kruth, J. P.; Froyen, L.; Van Vaerenbergh, J.; Mercelis, P.; Rombouts, M.; Lauwers, B. Selective laser melting of iron-based powder. *J. Mater. Process. Technol.* **2004**, *149*, 616–622, doi:10.1016/j.jmatprotec.2003.11.051.
  91. Ansys coupled-field analyses guide Available online: <http://support.ansys.com/documentation> (accessed on Nov 30, 2017).
  92. Chaboche, J. L. A review of some plasticity and viscoplasticity constitutive theories. *Int. J. Plast.* **2008**, *24*, 1642–1693, doi:10.1016/j.ijplas.2008.03.009.
  93. Ansys Inc. ANSYS Theory reference manual, Available online: <http://support.ansys.com/documentation> (accessed on Nov 30, 2018).
  94. Suárez Díaz, A. Thermomechanical and metallurgical modeling of laser hardening and laser cladding processes, PhD thesis, Universidade Da Coruna, Spain, 2011.
  95. Tamanna, N.; Crouch, R.; Gavaises, M.; Naher, S. A One-dimensional analysis of the distribution of temperature, stress and strain in the co-axial Laser Cladding process. In *20th International ESAFORM Conference on Material Forming*; AIP Conference Proceedings: Dublin, Ireland, 2017; 1-6.
  96. Oldani, C.; Dominguez, A. Titanium as a biomaterial for implants. In *Recent Advances in Arthroplasty*; Fokter, D. S., Ed.; 2012; 149–162 ISBN 978-953-307-990-5.
  97. Wang, S. H.; Wei, M. D.; Tsay, L. W. Tensile properties of LBW welds in Ti-6Al-4V alloy at evaluated temperatures below 450 °C. *Mater. Lett.* **2003**, *57*, 1815–1823, doi:10.1016/S0167-577X(02)01074-1.
  98. Van Noort, R. Titanium: the implant material of today. *J. Mater. Sci.* **1987**, *22*, 3801–3811.
  99. Chikarakara, E.; Fitzpatrick, P.; Moore, E.; Levingstone, T.; Grehan, L.; Higginbotham, C.; Vázquez, M.; Bagga, K.; Naher, S.; Brabazon, D. In vitro fibroblast and pre-osteoblastic cellular responses on laser surface modified Ti-6Al-4V. *Biomed. Mater.* **2015**, *10*, 015007(1-12), doi:10.1088/1748-6041/10/1/015007.
  100. Wally, J. Z., Grunsven, W. V., Claeysens, F., Goodall, R., Reilly, G. C. Porous titanium for dental implant applications. *Metals (Basel)*. **2015**, *5*, 1902–1920, doi:10.3390/met5041902.
  101. Parithimarkalaignan, S.; Padmanabhan, T. V. Osseointegration: An update. *J. Indian Prosthodont. Soc.* **2013**, *13*, 2–6, doi:10.1007/s13191-013-0252-z.
  102. Biswas, A.; Li, L.; Maity, T. K.; Chatterjee, U. K.; Mordike, B. L.; Manna, I.; Majumdar, J. Laser surface treatment of Ti-6Al-4V for bio-implant application. *Lasers Eng.* **2007**, *17*, 59–73.
  103. Balla, V. K.; Soderlind, J.; Bose, S.; Bandyopadhyay, A. Microstructure, mechanical and wear properties of laser surface melted Ti6Al4V alloy. *J. Mech. Behav. Biomed. Mater.* **2014**, *32*, 335–344, doi:10.1016/j.jmbbm.2013.12.001.
  104. Baloyi, N. M.; Popoola, A. P. I.; Pityana, S. L. Microstructure, hardness and corrosion properties of laser processed Ti6Al4V-based composites. *Trans. Nonferrous Met. Soc. China (English Ed.)* **2015**, *25*, 2912–2923, doi:10.1016/S1003-6326(15)63917-6.
  105. Bartolomeu, F.; Buciumeanu, M.; Pinto, E.; Alves, N.; Silva, F. S.; Carvalho, O.;

- Miranda, G. Wear behavior of Ti6Al4V biomedical alloys processed by selective laser melting, hot pressing and conventional casting. *Trans. Nonferrous Met. Soc. China (English Ed.)* **2017**, 27, 829–838, doi:10.1016/S1003-6326(17)60060-8.
106. Romano, J.; Ladani, L.; Sadowski, M. Thermal modeling of Laser based Additive Manufacturing processes within common materials. *Procedia Manuf.* **2015**, 1, 238–250, doi:10.1016/j.promfg.2015.09.012.
107. ASM International High-Strength Low-Alloy Steels. *Alloy. Underst. Basics* **2001**, 45, 193–202.
108. Tamura, I.; Sekine, H.; Tanaka, T.; Ouchi, C. *Thermomechanical processing of high strength low alloy steels*; Bitterworths & Co., 1988; ISBN 0408110341.
109. Bae, Y.; Lee, J.; Choi, J.; Choo, W.; Hong, S. Effects of austenite conditioning on austenite/ferrite phase transformation of HSLA steel. *Mater. Trans.* **2004**, 45, 137–142, doi:10.2320/matertrans.45.137.
110. Panigrahi, B. K. Microstructure-related properties of some novel reinforcement bar steel. *J. Mater. Eng. Perform.* **2010**, 19, 287–293, doi:10.1007/s11665-009-9456-0.
111. Panigrahi, B. K.; Jain, S. K. Impact toughness of high strength low alloy TMT reinforcement ribbed bar. *Bull. Mater. Sci.* **2002**, 25, 319–324, doi:10.1007/BF02704125.
112. Kabir, I. R.; Islam, M. A. Hardened case properties and tensile behaviours of TMT steel bars. *Am. J. Mech. Eng.* **2014**, 2, 8–14, doi:10.12691/ajme-2-1-2.
113. Sk, M. B.; Khan, A. K.; Lenka, S.; Syed, B.; Chakraborty, J.; Chakrabarti, D.; Deb, A.; Chandra, S.; Kundu, S. Effect of microstructure and texture on the impact transition behaviour of thermo-mechanically treated reinforcement steel bars. *Mater. Des.* **2016**, 90, 1136–1150, doi:10.1016/j.matdes.2015.11.053.
114. Smoljan, B. Prediction of mechanical properties and microstructure distribution of quenched and tempered steel shaft. *J. Mater. Process. Technol.* **2006**, 175, 393–397, doi:10.1016/j.jmatprotec.2005.04.068.
115. Huiping, L.; Guoqun, Z.; Shanting, N.; Chuanzhen, H. FEM simulation of quenching process and experimental verification of simulation results. *Mater. Sci. Eng. A* **2007**, 452–453, 705–714, doi:10.1016/j.msea.2006.11.023.
116. Şimşir, C.; Gür, C. H. 3D FEM simulation of steel quenching and investigation of the effect of asymmetric geometry on residual stress distribution. *J. Mater. Process. Technol.* **2008**, 207, 211–221, doi:10.1016/j.jmatprotec.2007.12.074.
117. Sánchez Sarmiento, G.; Gastón, A.; Totten, G. Computational modeling of heat treating processes by use of HT-mod and ABAQUS. *Lat. Am. Appl. Res.* **2011**, 41, 217–224.
118. Deng, X.; Ju, D. Modeling and simulation of quenching and tempering process in steels. *Phys. Procedia* **2013**, 50, 368–374, doi:10.1016/j.phpro.2013.11.057.
119. Madej, L.; Wang, J.; Perzynski, K.; Hodgson, P. D. Numerical modeling of dual phase microstructure behavior under deformation conditions on the basis of digital material representation. *Comput. Mater. Sci.* **2014**, 95, 651–662, doi:10.1016/j.commatsci.2014.08.035.
120. Tomellini, R. *Technical Steel Research: Modelling of steel microstructural evolution during thermomechanical treatment*; Brussels, 1997.
121. Şimşir, C.; Gür, C. H. A simulation of the quenching process for predicting

- temperature, microstructure and residual stresses. *Stroj. Vestnik/Journal Mech. Eng.* **2010**, 56, 93–103, doi:10.5545/84\_DOI\_not\_assigned.
122. He, C.; Heng, and X. *Principle of Chemical Engineering*; Science Press: Beijing, 2001;
  123. Outinen, J. Mechanical properties of structural steels at elevated temperatures and after cooling down. In *Fire and materials conference*; Interscience communications limited, UK: San Francisco, USA, 2006, 1-15.
  124. Chen, J.; Young, B.; Uy, B.; Chen, J.; Young, B.; Asce, M.; Uy, B. Behavior of high strength structural steel at elevated temperatures. *J. Struct. Eng.* **2006**, 132, 1948–1954, doi:10.1061/ASCE0733-94452006132:121948.
  125. Schneider, S.; G. Schneider, S.; Marques da Silva, H. Study of the non-linear stress-strain behaviour in Ti-Nb-Zr alloys. *Mater. Res.* **2005**, 8, 435–438, doi:http://dx.doi.org/10.1590/S1516-14392005000400013.
  126. Finite element method Available online: [http://web.mit.edu/16.810/www/16.810\\_L4\\_CAE.pdf](http://web.mit.edu/16.810/www/16.810_L4_CAE.pdf) (accessed on Apr 25, 2018).
  127. Element reference, Ansys Inc., Available online: <http://support.ansys.com/documentation> (accessed on Apr 30, 2018).

-----X-----

# Appendices

## A1. Theory and background

### A1.1 Principle of heat conduction in solid

Heat conduction is a process of heat transfer through the solid mass. The famous Fourier's law of heat conduction explains that the rate of heat flow inside a solid medium is proportional to the gradient of temperature and cross-sectional area of the medium. In LSG, solid-state cooling occurs due to the conduction. Because of very fast nature of the process and localised heating by focused laser beam, the convection and radiation terms of heat transfer are not significant in this case. The heat conduction in LSG is transient in nature which means the rate of temperature change through the solid is not constant over time. Therefore, the governing equation of heat transfer in LSG expressed by the first law of thermodynamics and Fourier's law of conduction, is formulated as follows.

$$\textit{input} - \textit{output} = \textit{change of rate of internal energy} \quad (\text{A1.1})$$

For steady-state conduction, there is no net change in rate of internal energy of the material and it is expressed as follows [86].

$$\textit{input} - \textit{output} = 0 \quad (\text{A1.2})$$

### A1.2 Thermal residual stress

Thermal residual stress is the interior stress developed in absence of any external mechanical force acting on the material that is undergone heat treatments. The temperature gradient usually acts as a force to cause displacement of the atoms and due to the material and support constraints (chemical bonds, clamping respectively) thermal residual stress generates against this atomic movement. In LSG, the steep temperature

gradient causes thermal residual stress on or around the surface. Thermal stress may be tensile or compressive nature depending on the process parameters and nature of constraints applied on the treated part. Sometimes the compressive residual stress is beneficial, however, tensile residual stress causes early crack formation tendency in the material surface or delamination of the modified surface layer from the bulk. Therefore, it is very important to investigate the nature and distribution of residual stress induced in LSG process. Thermal stress can be calculated by the total strain developed in the material depending on process parameters, material properties and behaviours, which has been explained in detail in chapter five [51, 94].

### A1.3 Finite element method

Finite element method is a powerful numerical method handling complex geometrical feature to solve many engineering problems. There are many software packages such as ANSYS, ABAQUS, COMSOL, use FEM to formulate the physical problem and solve it. FEM uses simple piecewise polynomial method to find out the solution and hence, it is very popular to the engineers and researchers over the other numerical methods such as finite difference method. However, FEM gives the approximate solution and it has inherent numerical errors while simplifying the complex geometry. The basic concept of FEM is that, based on the governing equation and boundary conditions of a physical problem FEM produced a set of simultaneous algebraic equation expressed in Equation A1.3 [126].

$$[K]\{u\} = \{F\} \quad (\text{A1.3})$$

In this Equation A1.3,  $[K]$  refers to the property matrix,  $\{u\}$  is the behaviour and  $\{F\}$  is the action. For example, in heat transfer problem  $[K]$  will be the thermal conductivity matrix,  $\{u\}$  will be the temperature for each node and  $\{F\}$  will be the heat source applied as a boundary condition.

#### A1.4 Thermomechanical coupling method

When a system shows different physical phenomena the coupling method helps to analyse the interactions among them. Coupling is established when the results of one analysis is input for another analysis to find out the output. In heat treatments like LSG, due to application of thermal energy by laser heat source, thermal diffusion occurs in the materials, which leads to the microstructural change and residual stress development inside the material. Therefore, there are three different phenomena underlined in LSG process and to analyse the interactions among them thermal-structural coupling analysis is carried out. There are two ways of coupling between two or more analyses. One is the load transfer coupling technique, which is otherwise called uncoupled or indirect or weak coupling. Other is the direct or strong coupling technique. In load transfer coupling, all analyses are run separately one after another and the output of first analysis is applied as input of the second analysis and so on. Through this technique, only one directional effect can be accounted. On the other hand, in direct coupling multiple analyses run simultaneously. There are different element types used in ANSYS for thermal-structural coupled analysis such as Plane 13, Plane 223 (2D), Solid 5, Solid 227 (3D) and more [127]. In ANSYS, it is possible to formulate both weak and strong coupling using direct coupling element type. For mathematical formulation of those coupling technique follow ref. [91]. The temperature induced strain is always considered one-way effect ignoring the reversible effect of strain on temperature. Therefore, the weak coupling is recommended in case of thermal stress analysis [94](p. 39).

## A2. Mesh convergence

### A2.1 Mesh convergence study of LSG model

The mesh convergence study has been carried out to find out the optimum size of element (in the laser irradiated zone) for the FEM thermal model. The study has initiated with the 2D circular cross-section of cylinder. The quarter of the circular cross-section using symmetry boundary condition has been used for saving computational space and time. The area near the surface has been meshed with fine elements and inner area with coarse elements. The beam diameter is very small of about 0.2 mm and the heat flux has been applied on the element surface. Therefore, the largest element length on the surface has been taken equal or less than 0.2 mm. Then the model has been run by varying the length of element size for laser power 200 W and 0.15 ms residence time.

The maximum surface temperature with no. of elements is plotted in Figure A2.1. The figure shows that from 500 no. of elements (around the laser irradiated area), the temperature becomes stable. Therefore, the mesh convergence study tells that from 5-2  $\mu\text{m}$  along the periphery and 10-5  $\mu\text{m}$  along the radius, will be optimal for this study of LSG. It is worth-mentioning that, the author has found that with beam diameter the optimal length of element changes. Therefore, by changing beam diameter one needs to remodel the process every time. This is one of the difficulties in mesh based numerical models.

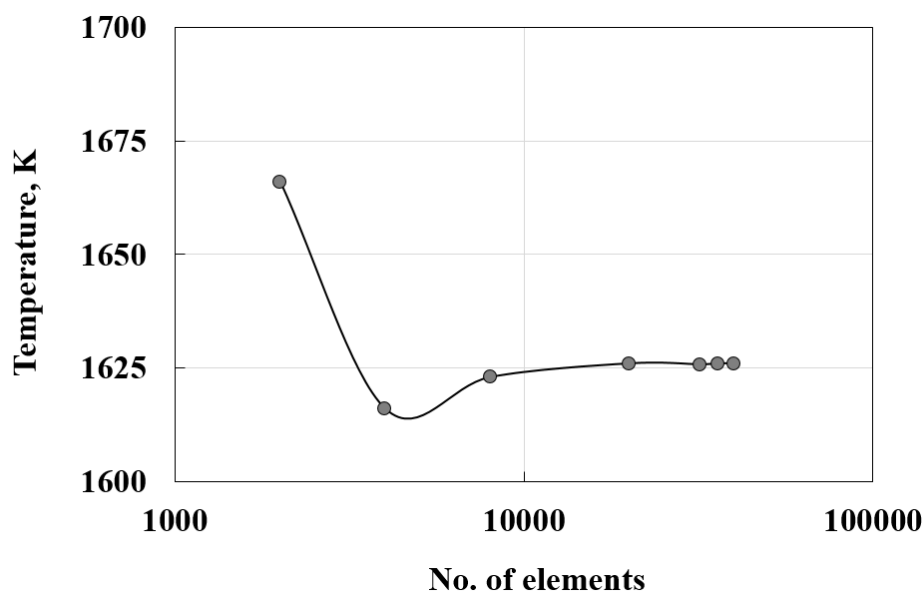


Figure A2.1 Maximum surface temperature varying with no. of elements around the laser irradiated area, for 200 W laser power, 0.2 mm beam diameter, and 0.15 ms residence time

#### A2.2 Mesh convergence study of quenching and tempering model

For every finite element analysis grid or mesh convergence study is important to find out the optimum number of elements number. A grid independence study was conducted to find out the accurate number of elements for TMT modelling with cylindrical model. From this study the solution became almost stable from 15400 number of elements and onward. Eventually the model was conducted with 48000 number of elements. The modelling takes 5 minutes on average to complete by Intel corei7 processor with 32GB random access memory and minimum 8GB storage. This model is focused on the quenching and tempering steps. The last pass temperature for rebar is kept in the austenitic zone so that after quenching the surface structure can transform into martensite. Therefore, the initial temperature is set for whole model as 1000- 1200 °C. Quenching step is modelled by setting boundary condition as forced convection in water medium for 2 s. After that the bar is allowed to cool naturally by changing boundary condition into

normal convection in air. In this stage the self-tempering happens because of the high temperature of the core. The maximum temperature of tempering depends on the temperature gradient between surface and core after quenching. In Chapter 6, Figure 6.2a, the cylindrical rolled sample of diameter 20mm and length 20mm is created for simulation of TMT process in ANSYS mechanical APDL. The meshed model is also illustrated in Figure 6.2b for 3D FEM quenching and tempering model.

### A3. APDL code of LSG modelling

#### A3.1 Geometry and mesh of half-cylindrical workpiece

```

et,1,55                                SAVE
et,2,70 !for 3D analysis                local,11,1,0,0,0
!creating geometry                      lsel,s,loc,x,0.005,0.0049475
PCIRC,0.005,0.0049925,0,180, !A1       ASLL,S
PCIRC,0.0049850,0.0049775,0,180, !A2   WPCSYS,-1,0
APLOT                                   wprota,,,90,
LPLOT                                   *do,i,1,432
a,3,5,                                   ASBW,all
APLOT                                   lsel,s,loc,x,0.005,0.0049475
KPLOT                                   ASLL,S
a,3,6,4,5, !creates area through keypoints wprota,,0.4167,,
APLOT                                   *enddo
FLST,2,4,3                              ALLSEL,ALL
FITEM,2,3                               APLOT
FITEM,2,6                               lsel,s,loc,x,0.00482,
FITEM,2,5                               ASLL,S
FITEM,2,4                               asel,u,,,11
A,P51X                                  WPCSYS,-1,0
PCIRC,0.00497,0.0049625,0,180,         wprota,,,90,
!A4                                     *do,i,1,144
KPLOT                                   ASBW,all
a,7,10,9,8,                             lsel,s,loc,x,0.00482,
PCIRC,0.0049550,0.0049475,0,180,     ASLL,S
!A6                                     asel,u,,,11
APLOT                                   wprota,,1.2501,,
a,11,14,13,12                          *enddo
APLOT                                   ALLSEL,ALL
PCIRC,0.00494,0.00482,0,180,         lsel,s,loc,x,0.00467,
a,15,18,17,16                          ASLL,S
PCIRC,0.00467,0.00452,0,180, !A10   WPCSYS,-1,0
a,19,22,21,20                          wprota,,,90,
PCIRC,0.00422,,0,180,                 *do,i,1,48
a,23,26,25,24

```

```

ASBW,all
lsel,s,loc,x,0.00467,
ASLL,S
wprota,,3.7503,,
*enddo
lsel,s,loc,x,0.00422
ASLL,S
WPCSYS,-1,0
wprota,,,90,
ASBW,all
lsel,s,loc,x,0.00422
ASLL,S
wprota,,90,,
ASBW,all
ALLSEL,ALL
SAVE
!meshing areas
lsel,s,loc,x,0.005,0.00422
lsel,u,loc,x,0.00422
LESIZE,all, , ,1, , , , ,0
lsel,s,loc,x,0.005,0.00494,
lsel,u,loc,x,0.005
lsel,u,loc,x,0.0049925
lsel,u,loc,x,0.0049850
lsel,u,loc,x,0.0049775
lsel,u,loc,x,0.00497
lsel,u,loc,x,0.0049625
lsel,u,loc,x,0.0049550
lsel,u,loc,x,0.0049475
lsel,u,loc,x,0.00494,
LESIZE,all, , ,6, , , , ,0
lsel,s,loc,x,0.005,0.0049475
ASLL,S
amesh,all
lsel,s,loc,x,0.00482,0.00467
ASLL,S

```

```

amesh,all
lsel,s,loc,x,0,0.00422
LESIZE,all, , ,16, , , , ,0 !LESIZE,all, ,
,24, , , , ,0
asll,s
asel,u,,,9
mshape,0,2d
mshkey,2
amesh,all !make free mesh anyway
csys,0
/PREP7
k,,0,0,0
k,,0,0,-0.001
KDELE, 4145
KDELE, 4146
k,,0,0,-0.001
lstr,27,4145
allsel,all
LPLOT
vdrag,all,37
vdrag,all,,,,,37,
APLOT
ALLSEL,ALL
APLOT
save

```

**A3.2 Thermal model with surface and volumetric heat source**

/PREP7	MPTEMP,3,473
MPTEMP,,,,,,,,	MPTEMP,4,673
MPTEMP,1,298	MPTEMP,5,873
MPTEMP,2,373	MPTEMP,6,1073
MPTEMP,3,473	MPTEMP,7,1273
MPTEMP,4,673	MPTEMP,8,1473
MPTEMP,5,873	MPTEMP,9,1673
MPTEMP,6,1073	MPTEMP,10,1873
MPTEMP,7,1273	MPTEMP,11,2073
MPTEMP,8,1473	MPTEMP,12,2273
MPTEMP,9,1673	MPDE,C,1
MPTEMP,10,1873	MPDATA,C,1,,477
MPTEMP,11,2073	MPDATA,C,1,,453
MPTEMP,12,2273	MPDATA,C,1,,467
MPDE,DENS,1	MPDATA,C,1,,502
MPDATA,DENS,1,,7650	MPDATA,C,1,,537
MPDATA,DENS,1,,7650	MPDATA,C,1,,572
MPDATA,DENS,1,,7600	MPDATA,C,1,,607
MPDATA,DENS,1,,7580	MPDATA,C,1,,642
MPDATA,DENS,1,,7550	MPDATA,C,1,,677
MPDATA,DENS,1,,7200	MPDATA,C,1,,708
MPDATA,DENS,1,,7150	MPDATA,C,1,,721
MPDATA,DENS,1,,7100	MPDATA,C,1,,721
MPDATA,DENS,1,,7000	MPTEMP,,,,,,,,
MPDATA,DENS,1,,7000	MPTEMP,1,298
MPDATA,DENS,1,,6900	MPTEMP,2,373
MPDATA,DENS,1,,6900	MPTEMP,3,473
MPTEMP,,,,,,,,	MPTEMP,4,673
MPTEMP,1,298	MPTEMP,5,873
MPTEMP,2,373	MPTEMP,6,1073
MPTEMP,7,1273	FITEM,5,44622
MPTEMP,8,1473	FITEM,5,-44623
MPTEMP,9,1673	NSEL,S, , ,P51X
MPTEMP,10,1873	CM,rectangle,NODE

```

MPTEMP,11,2073
MPTEMP,12,2273
MPDE,KXX,1
MPDATA,KXX,1,,29.5
MPDATA,KXX,1,,30.3
MPDATA,KXX,1,,33.7
MPDATA,KXX,1,,37
MPDATA,KXX,1,,40.5
MPDATA,KXX,1,,43.9
MPDATA,KXX,1,,47.3
MPDATA,KXX,1,,50.7
MPDATA,KXX,1,,21.98
MPDATA,KXX,1,,24.06
MPDATA,KXX,1,,25
MPDATA,KXX,1,,25

!creating a component by selecting nodes
1.8e-4by 2e-4
FLST,5,15,1,ORDE,15
FITEM,5,23
FITEM,5,-24
FITEM,5,43
FITEM,5,1972
FITEM,5,3889
FITEM,5,5912
FITEM,5,-5913
FITEM,5,5922
FITEM,5,-5923
FITEM,5,6172
FITEM,5,-6173
FITEM,5,25462
FITEM,5,-25463

!apply surface flux
SF,rectangle,HFLUX,2.86e9 !2.25e9
P=300W for rectangular surface heat
source
!BF,rectangle,HGEN,2.86e9 !for
volumetric heat source
allsel,all
/sol
ANTYPE,4
!*
TRNOPT,FULL
LUMPM,0
!*
DELTIM,1e-6,0,0
OUTRES,ERASE
OUTRES,ALL,ALL
AUTOTS,0
KBC,0
LNSRCH,1
NEQIT,50
TREF,298,
TIME,0.00015
SOLVE
*SET,user_time,0.00015
time,user_time+0.0004
SFDELE,all,all
allsel,all
SOLVE

```

**A3.3 2D thermomechanical model for Ti6Al4V alloy**

```

/PREP7
MPTEMP,,,,,,,,
MPTEMP,1,298
MPTEMP,2,373
MPTEMP,3,473
MPTEMP,4,673
MPTEMP,5,873
MPTEMP,6,1073
MPTEMP,7,1273
MPTEMP,8,1473
MPTEMP,9,1673
MPTEMP,10,1873
MPTEMP,11,2073
MPTEMP,12,2273
MPDE,DENS,1
MPDATA,DENS,1,,7650
MPDATA,DENS,1,,7650
MPDATA,DENS,1,,7600
MPDATA,DENS,1,,7580
MPDATA,DENS,1,,7550
MPDATA,DENS,1,,7200
MPDATA,DENS,1,,7150
MPDATA,DENS,1,,7100
MPDATA,DENS,1,,7000
MPDATA,DENS,1,,7000
MPDATA,DENS,1,,6900
MPDATA,DENS,1,,6900
MPTEMP,,,,,,,,
MPTEMP,1,298
MPTEMP,2,373
MPTEMP,3,473
MPTEMP,4,673
MPTEMP,5,873
MPTEMP,6,1073
MPTEMP,7,1273
MPTEMP,8,1473
MPTEMP,9,1673
MPTEMP,10,1873
MPTEMP,11,2073
MPTEMP,12,2273
MPDE,KXX,1
MPDATA,KXX,1,,29.5
MPDATA,KXX,1,,30.3
MPTEMP,8,1473
MPTEMP,9,1673
MPTEMP,10,1873
MPTEMP,11,2073
MPTEMP,12,2273
MPDE,C,1
MPDATA,C,1,,477
MPDATA,C,1,,453
MPDATA,C,1,,467
MPDATA,C,1,,502
MPDATA,C,1,,537
MPDATA,C,1,,572
MPDATA,C,1,,607
MPDATA,C,1,,642
MPDATA,C,1,,677
MPDATA,C,1,,708
MPDATA,C,1,,721
MPDATA,C,1,,721
MPTEMP,,,,,,,,
MPTEMP,1,298
MPTEMP,2,373
MPTEMP,3,473
MPTEMP,4,673
MPTEMP,5,873
MPTEMP,6,1073
MPTEMP,7,1273
MPTEMP,8,1473
MPTEMP,9,1673
MPTEMP,10,1873
MPTEMP,11,2073
MPTEMP,12,2273

```

MPTEMP,7,1273  
 MPDATA,KXX,1,,37  
 MPDATA,KXX,1,,40.5  
 MPDATA,KXX,1,,43.9  
 MPDATA,KXX,1,,47.3  
 MPDATA,KXX,1,,50.7  
 MPDATA,KXX,1,,21.98  
 MPDATA,KXX,1,,24.06  
 MPDATA,KXX,1,,25  
 MPDATA,KXX,1,,25  
 !!  
 mptemp,,,,,,,,,  
 mptemp,1,293  
 mptemp,2,373  
 mptemp,3,473  
 mptemp,4,673  
 mptemp,5,1173  
 mptemp,6,1473  
 mptemp,7,1873  
 mptemp,8,2073  
 mptemp,9,2773  
 mpdata,hf,1,,11.13  
 mpdata,hf,1,,13.64  
 mpdata,hf,1,,18.3  
 mpdata,hf,1,,33  
 coefficient  
 mpdata,hf,1,,117  
 mpdata,hf,1,,212.5  
 mpdata,hf,1,,409.5  
 mpdata,hf,1,,743.6  
 mpdata,hf,1,,1000  
 !!!structural properties  
 MPTEMP,,,,,,,,,  
 MPTEMP,1,298  
 MPTEMP,2,623  
 MPTEMP,3,833  
 MPDATA,KXX,1,,33.7  
 MPTEMP,5,1473  
 MPTEMP,6,1973  
 MPTEMP,7,2273  
 MPDE,EX,1  
 MPDE,PRXY,1  
 MPDATA,EX,1,,2.06e11 !Young's  
 MPDATA,EX,1,,1.92e11  
 MPDATA,EX,1,,1.42e11  
 MPDATA,EX,1,,0.880e11  
 MPDATA,EX,1,,0.180e11  
 MPDATA,EX,1,,0.150e11  
 MPDATA,EX,1,,0.130e11  
 MPDATA,PRXY,1,,0.30 !Poisson's  
 MPDATA,PRXY,1,,0.328  
 MPDATA,PRXY,1,,0.372  
 MPDATA,PRXY,1,,0.408  
 MPDATA,PRXY,1,,0.445  
 MPDATA,PRXY,1,,0.468  
 MPDATA,PRXY,1,,0.476  
 !Yield strength and Tangent Modulus  
 !isotropic hardening model  
 TB,BISO,1,6,2,  
 TBTEMP,298  
 !convection TBDATA,,1.20e8,7.95e10,,,  
 TBTEMP,833  
 TBDATA,,0.56e8,5.19e10,,,  
 TBTEMP,1073  
 TBDATA,,0.440e8,4.08e10,,,  
 TBTEMP,1673  
 TBDATA,,0.085e8,0.57e10,,,  
 TBTEMP,1973  
 TBDATA,,0.078e8,0.36e10,,,  
 TBTEMP,2273  
 TBDATA,,0.058e8,0.22e10,,,  
 !kinematic hardening model

```

MPTEMP,4,1073
TBTEMP,298
TBDATA,,1.20e8,7.95e10,,,
TBTEMP,833
TBDATA,,0.5e8,5.19e10,,,
TBTEMP,1073
TBDATA,,0.440e8,4.08e10,,,
TBTEMP,1673
TBDATA,,0.085e8,0.57e10,,,
TBTEMP,1973
TBDATA,,0.078e8,0.36e10,,,
TBTEMP,2273
TBDATA,,0.05878,0.22e10,,,
MPTEMP,,,,,,,,
MPTEMP,1,298
MPTEMP,2,623
MPTEMP,3,833
MPTEMP,4,1273
MPTEMP,5,1673
MPTEMP,6,1973
MPTEMP,7,2273
UIMP,1,REFT,,298
MPDATA,CTEX,1,,10.3E-006
!Thermal expansion coefficient
MPDATA,CTEX,1,,12.1E-006
MPDATA,CTEX,1,,12.7E-006
MPDATA,CTEX,1,,13.6E-006
MPDATA,CTEX,1,,14.2E-006
MPDATA,CTEX,1,,14.2E-006
MPDATA,CTEX,1,,16.4E-006
!Setting the keyoptions for direct coupled
ET
/PREP7
!plane223
!plane stress
KEYOPT,1,1,11
TB,BKIN,1,6,2,0
KEYOPT,1,3,0
KEYOPT,1,4,0
KEYOPT,1,9,1
KEYOPT,1,10,0
!plane strain
KEYOPT,1,1,11
KEYOPT,1,2,1
KEYOPT,1,3,2
KEYOPT,1,4,0
KEYOPT,1,9,1
KEYOPT,1,10,0
FINISH
/SOL
!boundary condition at centre node
D,26720, , , , ,UX,UY, , , ,
allsel,all
!Initial condition
FLST,2,29173,1,ORDE,2
FITEM,2,1
FITEM,2,-29173
IC,P51X,TEMP,298, ,
!apply heatsource
local,11,2,0,0,0,
nsel,s,loc,x,0.005,0.00499929
nsel,r,loc,y,88.855,91.145
CM,heatsource,NODE
csys,0
SF,heatsource,hflux,1.91e9      !4.77e9,
5.73e9
allsel,all
ANTYPE,4
TRNOPT,FULL
LUMPM,0
!NSUBST,150
DELTIM,1e-6,0,0

```

```

KEYOPT,1,2,1
OUTRES,ALL,ALL
AUTOTS,0
KBC,0
LNSRCH,1
NEQIT,50
NLGEOM,1 !large deformation transient
TREF,298
TIME,0.00015
SOLVE
SFDELE,all,all
*SET,user_time,0.00015
time,user_time+0.0004
allsel,all
SOLVE
FINISH
!derivative in post26
!NSOL,7,1,TEMP,,TEMP_7,
!STORE,MERGE
!DERIV,9,TEMP_7,TIME, ,rateT, , ,1,
!NSOL,2,441,U,Y,UY441 ! Defines
variable 2 as UY at node 441, name =
UY441
!DERIV,3,2,1,,VEL441 ! Variable 3 is
derivative of variable 2 w.r.t.
! variable 1 (time), name = VEL441
(velocity)
!DERIV,4,3,1,,ACCL441 ! Variable 4 is
derivative of variable 3 w.r.t.
! variable 1 (time), name = ACCL441
(acceleration)
/post26
NSOL,2,1,Temp,,Temp1
DERIV,3,2,1,,Rate1

```

---

The End

---